

Journal of Materials Chemistry A

Doped and Functionalized Non-Ti-MXene for Flexible and Wearable Electronic Devices

Journal:	Journal of Materials Chemistry A
Manuscript ID	TA-REV-10-2024-007376.R1
Article Type:	Review Article
Date Submitted by the Author:	13-Nov-2024
Complete List of Authors:	De, Shrabani; North Carolina Agricultural and Technical State University, Chemistry Bastakoti, Bishnu; North Carolina A&T State University, Department of Chemistry

SCHOLARONE™ Manuscripts

Doped and Functionalized Non-Ti-MXene for Flexible and Wearable Electronic Devices

Shrabani De, Bishnu Prasad Bastakoti*

Department of Chemistry, North Carolina A&T State University,1601 E. Market St. Greensboro, North Carolina, 27411, USA

*Email: <u>bpbastakoti@ncat.edu</u>

Abstract

Unique physicochemical properties of non-Ti-MXenes have attracted prominent attention in various fields. Doping/substitution and surface modification of non-Ti-MXenes have also started gaining interest because of their enhanced efficiency and targeted application. Recently, the flexibility of non-Ti-MXenes has started becoming popular in wearable electronics. The state-of-the-art research progress on non-Ti-MXenes and their doped/substituted or surfacemodified counterparts is systematically reviewed in this article as well as their flexibility and recent utilization in wearable and portable electronic devices. Theoretical and experimental research on synthesis strategies, unique properties, and electrochemical efficiency of the most studied 10 non-Ti-MXenes have been discussed in this review. Also, doping/substitution and surface functionalization of non-Ti-MXenes have been reviewed in terms of their characteristics, synthesis techniques, and benefits. The introduction of flexibility using different techniques and their recent utilization in various flexible and wearable electronic devices have also been systematically reviewed. Moreover, the challenges and outlook of this area are also enlightened for future opportunities. The novelty of this article is depicted by addressing the less-investigated category of MXenes that is non-Ti-MXenes. This is the first review covering doping and surface modification of non-Ti-MXenes for implementation in flexible and wearable electronics.

Keywords: Non-Ti-MXene, doping, functionalization, flexibility, and wearable electronics.

1. Introduction

In the past few years, significant advancements in miniaturization and downscaling of flexible and wearable intelligent electronics for human use have achieved exponential advancement. Wearable as well as flexible gadgets introduce a creative paradigm in every exposure of human life and can be implemented in various applications such as soft robotics, communication, sports fitness, smart sensors, intelligent household and medical devices, and so on 1-6. However, the current development in wearable and flexible electronics is still in the early stages and the main focus is on reliability, stability, and the robust performance of these electronic devices. Remarkably, further advancement in flexible and wearable electronics can be achieved by encountering their inherent characteristics like being lightweight, cost-effective, and effortlessly mounting on skin. Thus, the development of multifunctional and intelligent electronics plays an important role in various devices like energy storage, health monitors, sensors, and energy harvesters 7-16.

Although, batteries and supercapacitors are the mostly studied energy devices, energy harvesters and electronic sensors are also portraying irreplaceable opportunities to solve real world energy problems¹⁷. They harness energy employing piezoelectric, pyroelectric, and thermoelectric characteristics of nanomaterials to generate electricity and have the potential to be used in self-powered flexible devices¹⁸. The energy harvesting ability and flexibility of these nanogenerators have been practically applied in human health monitoring sensors. In healthcare devices, the interaction between electronic devices with human skin should be natural to monitor the medical condition. Therefore, the materials need to be compatible with human skin, sustainable, resilient, and durable for noninvasive tracking, which is essential for electronic sensing where the human body is involved^{19, 20}. To achieve these requirements, in recent years, significant research has been carried out in this field by utilizing a variety of organic and inorganic nanomaterials^{21, 22}. The main way to overcome these limitations is to fabricate novel materials that are associated with high mechanical strength, biocompatibility, and excellent sensitivity while simultaneously having superior energy storage efficiency. However, these challenges were not considerably encountered until the exposure to twodimensional (2D) materials.

Recently, 2D materials like transition metal oxides, layered double hydroxides, hexagonal boron nitrides, metal-organic frameworks, and perovskites have been extensively investigated to advance flexible and wearable electronics for versatile applications²³. These 2D materials are either mechanically unstable or have low electrochemical activity due to the less

inherent electronic conductivity²⁴. Thus, a substantial amount of electrode fillers like polymeric binders and conducting materials are needed to sustain the conductivity and nobility of the electrode, which incorporates difficulties in the fabrication process and negatively impacts the efficiency of the electronic devices. Therefore, the novel 2D materials associated with available active sites to accelerate the electrochemical reactions, high electrical conductivity, and mechanical stability are crucial for achieving next-generation wearable and flexible electronic devices.

In the development and design of flexible electronics, a new layered 2D material known as MXenes, which are the transition metal carbides, nitrides, or carbonitrides have been gaining notable attention from researchers after its discovery in 2011^{25} . MXenes are generally prepared from layered MAX phase precursors [Fig. 1] consisting of three different components having formula $M_{n+1}AX_n$, where M, A, and X denote an early transition metal, group 12 to 16 elements, and C and/or N, respectively and n=1-4. The prepared MXenes have the common representation as $M_{n+1}X_nT_x$ where T_x represents the surface terminalization with -O, -F, -OH, and -Cl groups²⁶. Additionally, the enormous interest in fabricating 2D structures inspired the development of MBene, which is a 2D structure similar to MXene synthesized from MAB phase where boron (B) has been used in place of C and/or N (X)²⁷. Further, the surface functionalization is also expanded not only from common -F, -OH, -O, and, -Cl groups but also to other non-metal groups²⁸. Moreover, new MXenes have been investigated and reported utilizing unexpected M metals like Lu and Mn, bringing new apprehensions into the future of enlarging ordinary MXenes from IIIB to the VIB family onwards²⁹⁻³¹.

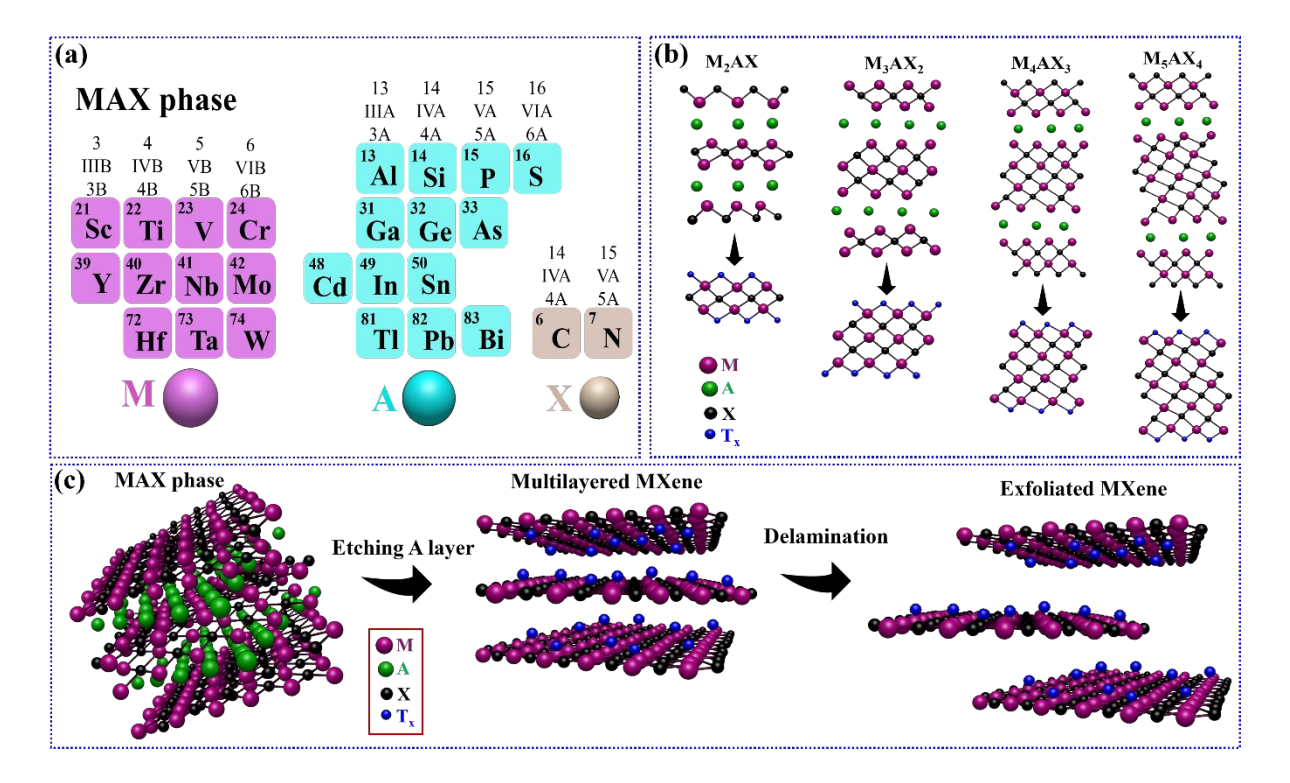


Fig. 1. (a) Different components of M, A, and X of MAX phases, (b) crystal structure of various MAX phases, and (c) schematic of typical synthesis strategy and delamination of MXene from its MAX phase precursor.

However, the uncommon MXenes have only been theoretically developed, and there have been a lot of challenges in their experimental synthesis. Over 50 MXenes have been successfully synthesized, while more than 70 MAX phases have been reported experimentally^{32, 33}. Different methods of single and multilayer MXene synthesis including (i) top-down process in which selective etching of MAX and non-MAX phase occurs, (ii) bottom-up process via salt-templated growth and chemical vapor deposition (CVD), and (iii) chemical transformations have been introduced so far³⁴⁻³⁷. Due to the intrinsic advantageous characteristics of MXene such as excellent electrical conductivity (up to 20000 S cm⁻¹)³⁸, large specific surface area (~347 m² g⁻¹)³⁹, the impressive elastic modulus of 330 GPa⁴⁰, high thermal conductivity (108 W m⁻¹ K⁻¹)⁴¹, good chemical stability, superior hydrophilicity, and environmental compatibility show favorable output in a versatile range of applications. MXenes hold promise in the fields of energy storage like battery and supercapacitor, energy generation such as solar cell and electro/photocatalysis, wearable and flexible electronics, environmental applications like heavy metal/oil adsorption and water treatment, sensors, biomedical applications, seawater desalination, and electromagnetic shielding⁴²⁻⁴⁸.

Thus, owing to their versatile characteristics like superior hydrophilicity, atomic layer thickness, and microscale lateral size, a flexible paper/film electrode of MXene can be easily assembled by coating or vacuum filtration⁴⁹⁻⁵¹. Further, high electronegativity conferred by the fluorine ion during etching and sufficient surface-active sites facilitates the composite formation of MXene with other nanomaterials resulting in the fabrication of flexible as well as efficient composite electrodes⁵². The MXene-based flexible materials have been used in versatile electronic devices, including upgraded flexible electronics⁵³, healthcare sector^{54, 55}, and the division connected to wearable energy^{50, 56}. Fabrication of electronics from bioinspired resources and fusion of them in textile or planar substrates for flexible and wearable electronics is feasible due to the unique structural features of MXene^{57, 58}. This results in the implementation of MXene in real-time functional applications, including smart textile-based devices, printed electronics, and three-dimensional (3D) frameworks like aerogels and hydrogels⁵⁹⁻⁶¹. In the wearable and flexible application region, MXene is becoming one of the most exciting candidates due to its ability to advance hybridization and coupling with other materials at the nano level⁶². It is counted on MXene-based nanoelectronic devices that the coming years will witness tremendous growth and efficient processing of these materials.

Despite infinite promises, the significant limitations associated with MXene research are the self-restacking of MXene layers, the tendency to oxidize, high contact resistance, low flexibility, and cytotoxicity⁶³⁻⁶⁵. Inspired by other 2D materials, doping and surface modification of MXene have been established as a successful strategy to conquer these limitations and enhance their performance by unlocking its efficiency in new horizons. Generally, doping means the incorporation of foreign elements into a 2D system via the incorporation/substitution of heteroatoms in the lattice structure which is an effective method to tune their physicochemical characteristics⁶⁶⁻⁶⁸. Overall, doping in the MXene system results in the following advantages:

- 1. Significantly incorporate Fermi energy⁶⁹;
- 2. Inert species get converted to electrochemically active sites resulting in an increment in conductivity⁷⁰;
- 3. Generate defects by adjusting the electronic structure of the material resulting in an improvement in electrochemical performance⁷¹;
- 4. Calibrate the nature of chemical bonds and the surface functional groups that restrict the rearrangement of MXene and accelerate the polysulphide transition⁷²;

- 5. Tune the bandgap by tailoring the surface chemical characteristics to trigger the catalytic performance^{73, 74};
- 6. Fine-tune the grating range leading to the improvement in photometric range resulting in superior photoelectric efficiency⁷⁵. Therefore, doping tunes the atomic structure and properties of MXene via surface or lattice modification or substitution, which considerably boosts the device's performance and stability⁷⁶⁻⁷⁸.

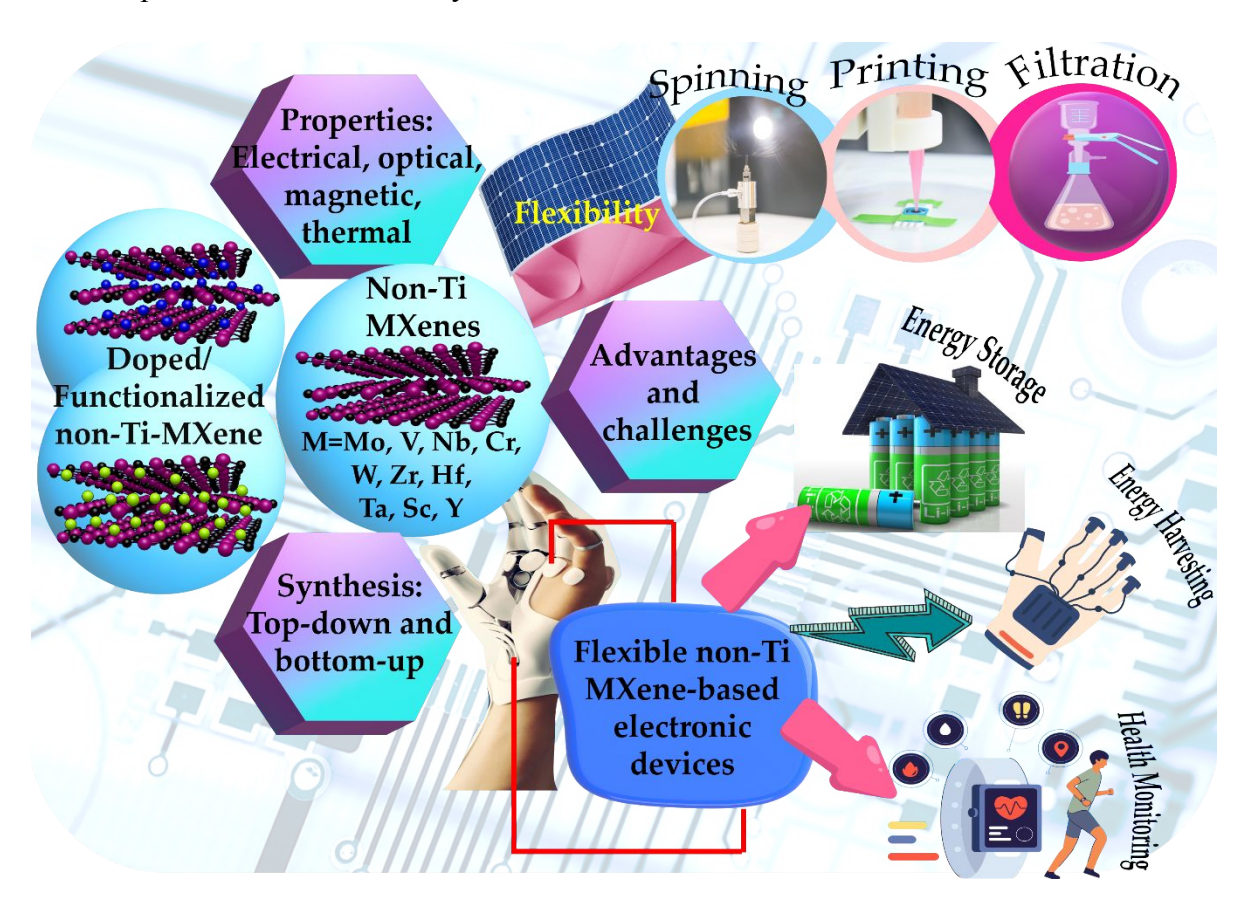


Fig. 2. General overview of the focus areas of this review.

Further, the tuning of surface functional groups (T_x) can modify and improve the characteristics of MXene⁷⁹. Functionalized MXenes can be synthesized by modifying pristine MXene with covalent and non-covalent functional groups. Covalent functionalization of surface can be classified into three categories^{80, 81}: (i) surface-initiated polymerization by macromolecules⁸², (ii) single heteroatoms⁸³, and (iii) small molecules like acid halide, alkali metal hydroxide, acid anhydride, organic amines, and epoxy compounds⁸⁴⁻⁸⁷. On the other hand, non-covalent surface functionalization can be achieved via hydrogen bonding, electrostatic interaction, and van der Waals forces⁸⁸⁻⁹².

Interestingly, the flexibility of non-Ti-MXenes and their doped or functionalized versions has started gaining interest in wearable electronics. A variety of techniques like printing and spinning have been used to develop flexible and freestanding non-Ti-MXenes. Still, non-Ti-MXene is less investigated area of MXene family and very few reviews have been reported on them. For example, Lamiel et al. reviewed structure, properties and various applications of non-Ti-MXenes in 2023⁹³. However, doping and surface modification of non-Ti MXenes are not reviewed before. Additionally, flexibility of non-Ti-MXene and their doped/functionalized counterparts are also not reviewed earlier. Advantageous properties and more targeted applications of non-Ti-MXenes compared to Ti-MXenes urges a proper review which covers their synthesis, physicochemical properties with dopant or functional group, and flexibility for application in wearable and flexible electronics. The novelty of this article comparing other related MXene-based reviews is depicted by addressing the less-investigated category of MXenes that is non-Ti-MXene and this is the first review covering doping and surface modification of non-Ti-MXenes and their flexibility for implementation in wearable and portable electronics.

This review focuses on the potential impact of replacing conventional Ti-based MXenes with other metal-based counterparts and the effect of doping and surface functionalization on non-Ti MXenes. The properties, advantages, and current progress of this category of MXene materials are discussed. Additionally, the flexibility and application of non-Ti-MXene and their doped and functionalized versions in the field of flexible and wearable electronic devices, including energy storage, energy harvesting, and wearable health monitoring, have also been discussed. Further, limitations and future outlooks on this topic have also been included. Fig. 2 schematically demonstrates the overall focus of this review.

2. Common synthesis method of MXene from a MAX phase precursor

Initially, MAX phases paved the way for MXenes towards its future success. MAX phases were classified by Barsoum et al.⁹⁴ as a new group of solids and according to the n value of M_{n+1}AX_n, the configuration can be M₂AX, M₃AX₂, M₄AX₃, and M₅AX₄ for 211, 312, 413, and 514, respectively, among most of the MAX phases reported in the preliminary stage by Nowotny et al.⁹⁵. The crystal structures of MAX phases [Fig. 1(b)] are mostly hexagonal with space group of P63/mmc⁹⁶. In their crystal lattice structure, "A" layers are situated at the core of the trigonal prism with the M6X octahedral layers located at the edges⁹⁷. On the other hand, Hf, Zr, Sc based compounds most likely consist of alternate NaCl-like M-C bonds with Al₄C₃-type Al(A)-C layers familiar as non-MAX phases. The common formula of these non-MAX

phases is (MC)_n[Al(A)]_mC_{m-1}, where A is Ge and/or Si, n is 2-4, and m is 3 or 4⁹⁸. Hybrid MAX phases consisting of metastable phases like M₅A₂X₃ and M₇A₂X₅ have also been reported⁹⁹. Initially, these hybrid MAX phases were evaluated in Ti-Si-C systems with 312 and 211 combinations of Ti₅Si₂C₃, on the other hand, with 312 and 413 combinations were applied for Ti₇Si₂C₅⁹⁹. Recently, quaternary MAX phases that result in the development of new MXenes have also been reported by alloying the original MAX phases and show in-plane (*i*-MAX) and out-of-plane (*o*-MAX) arrangement¹⁰⁰⁻¹⁰². Till now, above 155 MAX phase compounds have been reported theoretically and experimentally¹⁰³.

Commonly, the top-down synthesis method has been used to prepare MXene from its precursor MAX phase. MAX phases consist of stacked layers of comparatively strong M-X bonds because of their metallic and covalent interaction with comparatively weak M-A bonds ¹⁰⁴. This results in selective acid etching of the weak M-A bond and the formation of accordion-like MX layers by splitting the solid MAX phase [Fig. 1(c)] ¹⁰⁵. Further, the delaminated few-layered MXene can be obtained via different techniques like ultrasonication or shaking which further weaken the accordion-like stacked structure. Although Ti-based MXenes dominate the MXene research in various fields, the constantly expanding growth of MXene candidates has been stimulated by the optimized synthesis of new types of MXenes from *i*-MAX, *o*-MAX, hybrid, and non-MAX phases. Additionally, doping and surface functionalization of MXene during MAX phase synthesis or post-exfoliation process broaden the diversity of MXene stoichiometry.

3. Beyond Ti-based MXenes

Since, the successful delamination of Ti₃AlC₂ into Ti₃C₂ multilayered MXene by Gogotsi et al. around 100 stoichiometric MXene compounds have been developed, and among them ~70% of the MXene investigation was focused on titanium while the remaining 30% is split up to other less-studied early transition metal like Mo, V, Nb, Cr, W, Zr, Hf, Ta, Sc, and Y-based MXenes⁹³. However, a small number of publications of non-Ti-based MXenes is attributed to the complicated synthesis route and lower stability of these MXenes. Despite the complicated synthesis method, MXenes, are associated with differently promising intrinsic characteristics and abundance, summarized in Table 1.

Table 1. Characteristics and abundance of the early transition metals of MXene. Values acquired from Royal Society of Chemistry, 2024.

Metal	Atomic	Atomic	Density	Boiling	Melting	Young's	Abundance
(M)	number	mass	(g cm ⁻³)	point	point	modulus	on earth
				(°C)	(°C)	(GPa)	(ppm)
Ti	22	47.867	4.506	3287	1670	115.7	4136
Mo	42	95.95	10.2	4639	2622	-	0.8
V	23	50.942	6.0	3407	1910	127.6	138
Nb	41	92.906	8.57	4741	2477	104.9	8
Cr	24	51.996	7.15	2671	1907	279.1	135
W	74	183.84	19.3	5555	3414	411	1
Zr	40	91.224	6.52	4406	1854	-	132
Hf	72	178.486	13.3	4600	2233	-	3
Ta	73	180.948	16.4	5455	3017	185.7	0.7
Sc	21	44.956	2.99	2836	1541	74.4	0.3
Y	39	88.906	4.47	3345	1522	63.5	33

Their unique properties are sometimes more remarkable than the conventional Ti-based MXenes which make them attractive in versatile applications¹⁰⁶. Table 2 summarises different non-Ti-MXenes with their synthesis methods from corresponding MAX phases and their major outcomes.

3.1 Mo-based MXenes

In spite of its low abundance on earth's crust, molybdenum-based MXenes have been the second most investigated MXene candidate because of their superior performance in energy storage, medical, and catalysis field¹⁰⁷⁻¹⁰⁹. Although the MAX phases are the conventional precursor materials for MXenes, Mo₂GaN, and Mo₂AlC cannot be synthesized due to the thermodynamic instability¹¹⁰. On the other hand, Mo₂Ga₂C can be prepared successfully as a layered bulk MAX phase [Fig. 3(a)], which results in Mo₂C MXene after etching^{107, 110}. The trials of selective etching of Ga from Mo₂GaC to synthesize Mo₂C MXene remained almost unsuccessful^{111, 112}. The first bulk-scale preparation of 2D layered Mo₂CT_x MXene was reported by Halim et al. via selective removal of Ga-layer from Mo₂Ga₂C applying LiF/HCl etchant [Fig. 3(b)]¹¹³. Further, the layer exfoliation was acquired by simple handshaking of the

aqueous MXene dispersion. Notably, 2D transition metal boride (MBene) has also been synthesized from bulk ternary MAB phase¹¹⁴ which became a promising raw material by following a similar idea and route of MXene. A molybdenum-based MBene (MoB) [Fig. 3(c)] was synthesized from MoAlB (MAB phase) via HF-free hydrothermal etching process¹¹⁵. However, it was observed that the Al layer was not fully etched out, as evidenced by the traces of the precursor material MoAl_{1-x}B [Fig. 3(d)]. The epitaxial method was followed to prepare MXene from another non-MXene precursor ³⁵. In this process, 2D Mo₂C was prepared via chemical conversion through thermal annealing of MoS₂ crystals under CH₄ and H₂ atmosphere. According to the DFT calculation, the transformation of MoS₂ was initiated on their edge, where carbide conversion and hydrodesulfurization happened. The bottom-up method was also employed to synthesize Mo-MXene, like chemical vapor deposition (CVD) [102] and solid-state synthesis [103] through which the surface functionalization of such MXenes could be controlled precisely.

Mo₂C with Mo-termination without surface functional groups (T_x) exhibited superior stability and catalytic activity compared to Cu-ZnO-Al₂O₃ and β-Mo₂C¹¹⁶. Mo₂C MXene without surface functional groups showed enhanced performance and selectivity towards CO₂ hydrogenation. Mo-MXene become more advantageous than the conventional Ti-MXenes in the field of electrocatalysis¹¹⁷. Several research has been carried out to tune the properties of Mo-MXene and phase engineering is one of the approaches among them to host polymorphism in 2D Mo₂C crystals¹¹⁸. The diffusion barrier between Mo and C, the elemental precursors can be tuned by adjusting the thickness of the Cu foil catalyst resulting in controlled crystal growth. This kind of engineering can regulate the stacking type of Mo-MXene to Bernal (AB) type which becomes advantageous for the catalytic activity than the traditional AA type stacked crystals [Fig. 3(e)]¹¹⁸. Metal substitution like Co- and Fe- in 2D Mo₂CT_x can also enhance the reactivity of Mo-MXene [Fig. (f)]^{119, 120}.

Thus, the established research on Mo-MXene has grown from the MAX phase precursor to the MAB phases. This facilitates broad opportunities for researchers to study various characteristics and applications of MBene as a class of MXene. Although the limited abundance of molybdenum restricts its application, metal-substituted Mo-MXenes with combative characteristics need to be studied well.

3.2 V-based MXenes

After titanium, vanadium is one of the most abundant (Table 1) among other metals, and thus V-based MXenes are comparable in cost-effectiveness to Ti-MXenes. The research on V-MXenes has been developed experimentally contrasting with other non-Ti-MXenes and found application in various fields like supercapacitor, theranostics, electrocatalyst, nuclear waste adsorption, and so on¹²¹⁻¹²⁴. Also, vanadium has been incorporated in many double transition metal-based MXenes like Mo-V¹²⁵, Cr-V¹²⁶, and Ti-V-based¹²⁷ MXenes.

The selective elimination of Al atom occurs from V_2AIC , the precursor MAX phase of V_2CT_x MXene following the typical HF etching method [Fig. 3(g)]¹²⁸. The delaminated few layered V_2CT_x nanosheets [Fig. 3(h)]¹²⁹ were obtained from the stacked multilayers [Fig. 3(i)] ¹²³ via sonication. The successful formation of V-MXene from MAX phase can be established by XRD [Fig. 3(j)] and BET surface area analysis [Fig. 3(k)]¹³⁰. Also, high-quality vanadium carbide MXene has been successfully prepared via a safer and HF-free etching method using NaF^{131} or LiF/HCl¹³². The widely used organic delaminating agents for MXene like tetramethylammonium hydroxide (TMAOH)¹³³ and tetrabutylammonium hydroxide (TBAOH)¹³⁴ have also been used for effective intercalation in V-MXene structure. The ion intercalation method has also been used to increase the interlayer spacing where Sn was intercalated in V_2C MXene by forming V-O-Sn covalent bonding¹³⁵. The green method for delamination of V_2C with good structural stability and a high yield of 90% was reported using algae extraction¹³⁶.

It was reported that V₂C nanosheets showed photothermal efficiency for magnetic resonance imaging and photoacoustic imaging-guided photothermal therapy for cancer¹³⁶. Additionally, V₂CT_x showed superior theoretical capacity than Nb₂CT_x, Ti₂C, and commercial graphitic carbon¹³⁷. Thus, V-based MXenes are associated with versatile opportunities to be investigated in other energy-related applications. Therefore, different HF-free synthesis methods of V-based MXenes have shown successful outcomes. This is inspiring to the researchers to investigate facile synthesis methods of M-MXene with safer chemicals. Also, doping become an interesting strategy to tune and enhance the overall characteristics of V-based MXenes which can be beneficial for targeted modern applications.

3.3 Nb-based MXenes

The traditional top-down method for the selective etching of Al using HF has also been utilized here to synthesize accordion-like multilayered Nb₂C MXene¹³⁸ from Nb₂AlC MAX phase [Fig.

3(l, m)]^{139, 140}. But, even under a favorable atmosphere, HF-etched Nb-MXene tends to get oxidized¹⁴¹. So, the HF-free methods have also been explored to synthesize Nb-MXene using an electrochemical method¹⁴¹ or HCl etching^{142, 143} which offer safe and quick synthesis with enhanced surface area, high porosity, excellent conductivity, good chemical stability, and less cytotoxicity. Further, TBAOH¹⁴⁴ and tetrapropylammonium hydroxide (TPAOH)^{139, 140, 142, 145} were most commonly used as intercalants for the delamination of Nb-MXene into a few layers. The increasing interest in using MXene to procure nanomaterials has also significantly gained attention among researchers. For example, Nb₂O₅ nanoparticles covered over the surface of carbon layers have been synthesized from Nb₂CT_x MXene via CO₂ calcination or hydrothermal method¹⁴⁶. Some other reported unique morphologies of Nb-MXene were nitrogen-doped-Nb₂C/Nb₂O₅¹⁴⁷, 1D nanowire framework¹⁴⁸, carbon nanotube (CNT) and 2D Nb₂CT_x composite¹⁴⁴, and ferroelectric crystals derived from MXene¹⁴⁹.

Nb-MXenes have versatile characteristics like good photothermal stability, metallic conductivity, photonic and optical properties, biocompatibility, and high capacitive performance¹⁵⁰. Importantly, Nb₂CT_x performed better than the aqueous Ti-based MXene analogs [Fig. 3(n)] and exhibited very high energy density (146.7 Wh kg⁻¹)¹⁵¹. Additionally, the superior pseudocapacitive performance of Nb₂C MXene was reported with better cyclic life and fast kinetics than the Ti₂C and Ti₃C₂¹⁵². The properties and applications of Nb-MXene with various surface terminations like chlorine (Cl), imidogen (NH), bromine (Br), selenium (Se), sulfur (S), tellurium (Te) as well as bare Nb₂C with conventionally functionalized (-F, -OH, -O) Nb-MXene were also evaluated^{28, 153}. The work function of Nb₂CT_x can also be tuned by controlling the number of surface terminal groups of MXene¹⁵⁴. Nb-MXenes have been used in various fields of applications like medical implants, sensing, capacitors, photonics, batteries, sensing, catalysis and with such promising performances Nb-MXenes can be competitive with Ti or other non-Ti-based MXenes.

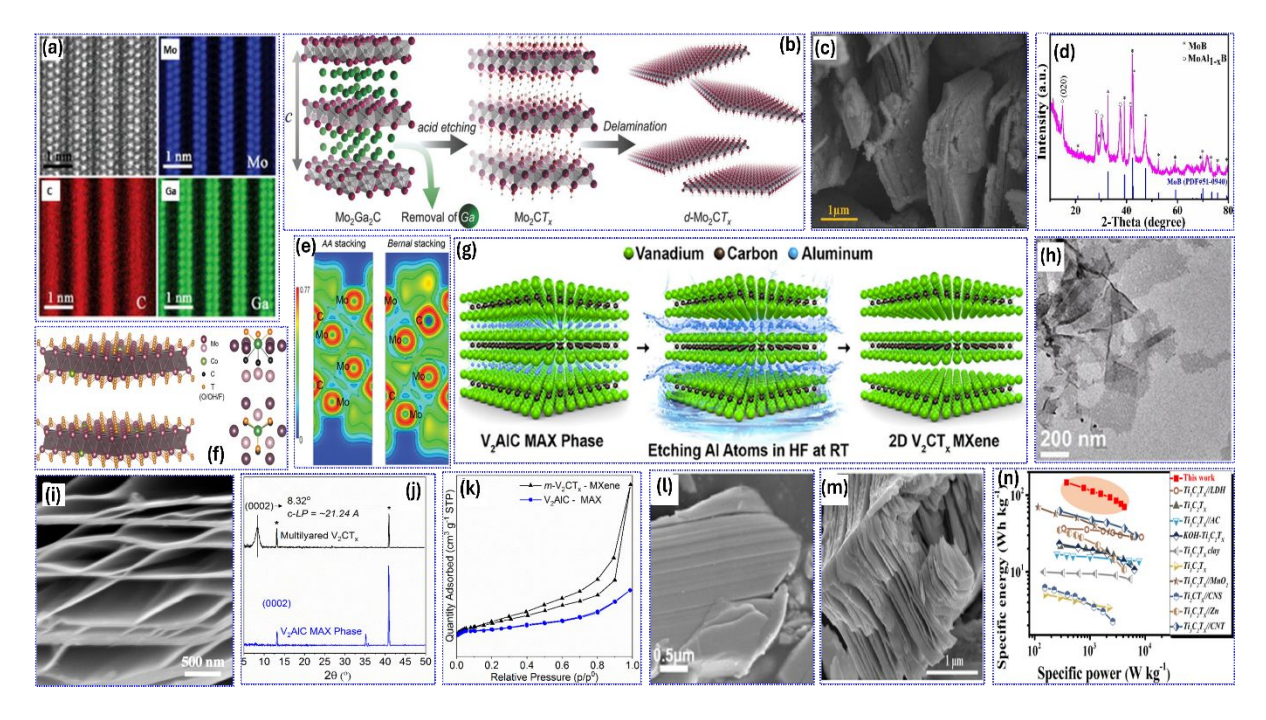


Fig. 3. (a) HRSTEM image of Mo₂Ga₂C with corresponding EDX mapping, (b) schematic representation of synthesis and delamination of Mo₂CT_x, (c) SEM image of 2D MoB layers, (d) XRD spectrum of MBene, (e) side view of the electronic localization function of AA and Bernal stacked Mo₂C with the color bar showing degree of localization of electrons, (f) Mo_2CT_x :Co structure, (g) synthesis method of V_2CT_x from V_2AlC , (h) TEM image of few layered V₂C obtained after sonication, (i) SEM image of stacked V₂CT_x, (j) XRD patterns of V_2AlC and multilayered V_2CT_x (* indicates unreacted MAX phase), (k) adsorption-desorption isotherm of multilayered V₂CT_x and V₂AlC, SEM images of (l) Nb₂AlC and (m) multilayered Nb₂C₁ (n) Ragone plot comparing performance of Nb-MXene with some previously reported Ti-MXenes. (a) Reproduced from ref¹⁰⁷ with permission from Wiley-VCH, copyright 2019, (b) reproduced from ref¹¹³ with permission from Wiley-VCH, copyright 2016, (c, d) reproduced from ref¹¹⁵ with permission from Elsevier, copyright 2022, (e) reproduced from ref¹¹⁸ with permission from Wiley-VCH, copyright 2019, (f) reproduced from ref¹¹⁹ with permission from American Chemical Society, copyright 2019, (g) reproduced from ref¹²⁸ with permission from American Chemical Society, copyright 2017, (h) reproduced from ref¹²⁹ with permission from Nature Portfolio, copyright 2021, (i) reproduced from ref¹²³ with permission from American Chemical Society, copyright 2016, (j, k) reproduced from ref¹³⁰ with permission from American Chemical Society, copyright 2020, (l, m) reproduced from ref¹⁴⁰ with permission from American Chemical Society, copyright 2020, (n) reproduced from ref¹⁵¹ with permission from Cell Press, copyright 2021.

3.4 Cr-based MXenes

Although Cr-MXenes is one of the most difficult to synthesize experimentally¹⁵⁵, recently they have gained interest due to their interesting electronic 156, ferromagnetic 157, and hydrogen storage¹⁵⁸ properties. Commonly, the most widely reported MAX phase for Cr-MXene is Cr₂AlC. Ball milling¹⁵⁹, magnetron sputtering¹⁶⁰, molten salt¹⁶¹, and sintering¹⁶² are the few reported methods to prepare Cr₂AlC MAX phase. Cr₂GaC is another reported MAX phase for Cr-MXene¹⁶³. Still, it remains a difficult task to synthesize a highly pure Cr-MXene, as the conversion of Cr-MAX phase predominantly results in anisotropic and bulk chromium carbide over 2D Cr-MXene¹⁶⁴. As Cr-MXene has low cohesive energy or stability compared to other MXenes, it is still challenging to synthesize Cr-MXenes like Cr₂N, Cr₃N₂, Cr₄N₃, Cr₂C, Cr₃C₂, and Cr₄C₃¹⁶⁵. Another challenging reason is the acid etching with HF results in the formation of fluoride salts or dissolution of metal for the Cr-MAX phases conflicting with the other commonly reported MAX phases¹⁵⁸. To eliminate the adverse results of using fluoridecontaining etchants a different etchant was reported where FeCl₃ and tartaric acid (for metalcomplex formation) was utilized [Fig. 4(a)] which generate soluble iron cations and aluminium complexes that can be easily eliminated by washing¹⁶⁶. Interestingly, an electrochemical method using dilute HCl exhibited successful removal of aluminium resulting in good quality Cr_2CT_x from its MAX phase precursor¹⁶⁷. On the other hand, the common etchants like HF, KF, NaF, NaOH, molten salt method, and acid mixture remained unsuccessful in efficient etching of the Cr-MAX phase¹⁶⁵.

The structural stability and electrocatalytic activity of 2D Cr₂CO₂ modified with transition metal and carbon vacancy were assessed by density functional theory (DFT)¹⁶⁸A theoretical study suggested that carbon vacancy reduces the bond strength of H on the surface of Cr₂CO₂, which facilitates electrocatalytic efficiency. Though experimental preparation of Cr-MXene is still challenging, theoretical reports have exhibited competing performance in various applications. Due to the natural abundance and low cost of Cr-MXene, there can be a great future focusing on synthesis and application in various areas.

3.5 W-based MXenes

The M₂AX phases consisting of W like W₂SC, W₂AlN, W₂SN, W₂SiN, W₂SnN, W₂GaN, W₂InN, W₂PbC and W₂GeN are reported as unstable forms¹⁶⁹. Therefore, the quaternary *i*-MAX phase with the formula $(M_{2/3}^1M_{1/3}^2)_2$ AlC, where M¹ and M² are the prior transition metals, were fabricated replacing the common MAX phases which consist of only one transition metal¹⁷⁰. Among around 18 compositions of $(W_{2/3}M_{1/3}^2)_2$ AC, where A is Al, Si, Ge,

Ga, Sn, In and M^2 is Y and Sc, the most stable *i*-MAX phase for experimental synthesis according to DFT calculation are $(W_{2/3}Y_{1/3})_2AlC$ and $(W_{2/3}Sc_{1/3})_2AlC^{171}$. HF or LiF/HCl had been used to eliminate Al and Sc or Y resulting in 2D $W_{1.33}C$ with ordered divacancies [Fig. 4(b)]. Lanthanides like Lu, Gd, Dy, Tb, Er, Ho, and Tm can also be used to replace Sc or Y in M^2 sites of the quaternary *i*-MAX phase¹⁷². Surface functionalized W_2C with -O and -F has been reported and used in NH_3 gas sensing field¹⁷³. Therefore, theoretical studies have been carried out to understand the potential of W-MXenes in different applications.

3.6 Zr-based MXenes

The layered quaternary or ternary transition metal carbides having a formula of $Zr_n[Al(Si)]_4C_3$ or $Zr_nAl_3C_2$ (where n=1,2,3) are categorized as non-MAX phases because Al-C units are eliminated explicitly in place of only Al atoms in normal MAX phases¹⁷⁴. Zhou et al. reported an in-situ sintering method pulsed with electric current was used to synthesize $Zr_3Al_3C_5^{175}$. The accordion like 2D $Zr_3C_2T_z$ MXene [Fig. 4(c)] was prepared by specific elimination of Al_3C_3 from $Zr_3Al_3C_5$ utilizing HF as etchant. Surface functionalized Zr-MXenes like $Zr_3C_2F_2$, $Zr_3C_2O_2$, and $Zr_3C_2(OH)_2$ had shown metallic conductivity and $Zr_3C_2O_2$ exhibited very high mechanical strength with C_{11} value of 392.9 GPa^{175} . According to the theoretical calculation, $Zr_3C_2O_2$ and Zr_2CO_2 behave as metal and semiconductor with Na-ion capacitance of 326 and 474 mA h g⁻¹, respectively¹⁷⁶, whereas the theoretical Li-ion capacitance Zr_2CO_2 , Zr_2CF_2 , Zr_2C , and Zr_2CS_2 were 266, 58, 310, and 259 mAh g⁻¹, respectively¹⁷⁷. Theoretical study suggested the application of surface-functionalized Zr-MXene in catalysis, water-splitting, and battery¹⁷⁶, 178, 179.

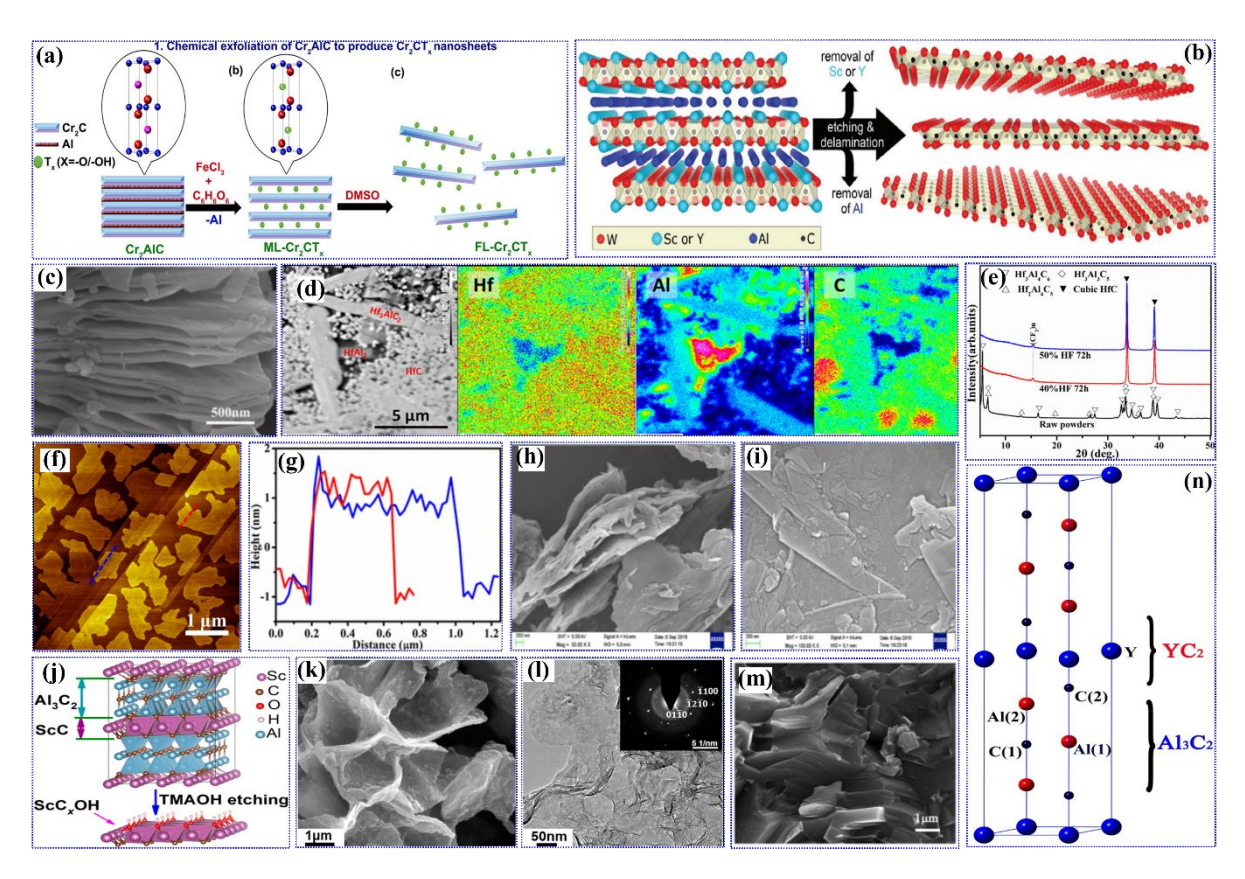


Fig. 4. (a) Cr₂AlC MAX phase and a unit cell of Cr₂AlC (color of balls: pink-Al; blue-C; red-Cr), (b) in-plane chemical ordering in (W_{2/3}Sc_{1/3})₂AlC or (W_{2/3}Y_{1/3})₂AlC *i*-MAX phase resulting in W_{1,33}C with ordered divacancies, (c) SEM of accordion like Zr₃C₂T_z, (d) elemental mapping of Hf, Al, C in a Hf-Al-C MAX phase, (e) XRD spectra of Hf-Al-C before and after etching, (f) AFM and (g) corresponding height profile of Hf₃C₂T_z, FESEM of (h) Ta₄C₃ and (i) Ta₄AlC₃, (j) synthesis method of ScC_xOH from ScAl₃C₃, (k) SEM image of ScC_xOH, (l) TEM image of delaminated ScC_xOH, (m) SEM image of YAl₃C₃, (n) crystal structure of YAl₃C₃. (a) Reproduced from ref¹⁶⁶ with permission from American Chemical Society, copyright 2020, (b) reproduced from ref¹⁷¹ with permission from Wiley-VCH, copyright 2018, (c) reproduced from ref¹⁸² with permission from American Chemical Society, copyright 2016, (e-g) reproduced from ref¹⁸¹ with permission from American Chemical Society, copyright 2017, (h, i) reproduced from ref¹⁸² with permission from Elsevier, copyright 2019, (j-l) reproduced from ref¹⁸³ with permission from American Chemical Society, copyright 2019, (m, n) reproduced from ref¹⁸⁴ with permission from Elsevier, copyright 2017, (m, n) reproduced from ref¹⁸⁵ with permission from Elsevier, copyright 2019, (m, n) reproduced from ref¹⁸⁶ with permission from Elsevier, copyright 2017.

3.7 Hf-based MXenes

Similar to the Zr-containing non-MAX phases, Hf-MXenes are also synthesized from layered quaternary or ternary non-MAX phase transition metal carbides having formula

 $(HfC)_n[Al(Si)]_4C_3$ or $(HfC)_nAl_3C_2$ (where $n=1, 2, 3)^{174}$. It has been observed that the preparation of pure conventional MAX phases specifically for Hf and Zr is not easy to obtain ¹⁷⁴. The hot pressing method was utilized to prepare Hf-containing ternary carbides like Hf₂Al₄C₅, Hf₃Al₃C₅, and Hf₃Al₄C₆¹⁸⁵. The elemental dispersion of Hf, Al, and C is shown in Fig. 4(d) in a Hf-Al-C MAX phase system¹⁸⁰. It was reported that MAX phases like Hf₂AlC and Hf₃AlC₂ contain HfAl₂, HfC, and Hf₂Al₃ phases. Also, the single-phase quaternary carbide of Hf-Al-Si-C system, Hf₂[Al(Si)]₄C₅ has been successfully prepared, which exhibited superior thermal and mechanical properties than HfC¹⁸⁶. A combination of hot pressing and spark plasma sintering methods have been utilized to synthesize single-phase Hf₂Al₄C₅ which consists of four Al-C layers (Al₄C₃) sandwiched between two Hf-C layers¹⁸⁷. For Hf-Al-C ternary carbides, the bonds between Hf-C and Al-C are strong enough, which makes it difficult for selective etching and exfoliation¹⁸¹. To weaken the interfacial bond, alloying of Si with Al was carried out in $Hf_3[Al(Si)]_4C_{6}$, which facilitates the HF etching and exfoliation into multilayered $Hf_3C_2T_z^{181}$. The XRD spectra of Hf₃[Al(Si)]₄C₆ before and after HF etching are shown in Fig. 4(e), which clearly indicates the exfoliation of MXene layer compared to the precursor MAX phase¹⁸¹. The morphology and corresponding height profile of Hf₃C₂T₇ MXene are shown in Fig. 4(f, g), respectively, which revealed the formation of bilayer MXene sheets¹⁸¹.

According to the first principle DFT calculation, Hf₃C₂O₂ showed strong mechanical strength among the surface functionalized Hf₃C₂T₂ (T = F, O, OH) MXenes¹⁸¹. On the other hand, functionalization with O-S on the surface of Hf-MXene resulted in a tuneable band gap associated with tuneable properties, which could be beneficial for a wide range of applications¹⁸⁸. Hf-MXenes have also been studied for sodium and lithium-ion batteries, and they delivered 504 and 1567 mAh cm⁻³ reversible volumetric capacitance, respectively¹⁸¹. Additionally, Li-bounded F-functionalized Hf-MXene exhibited efficient performance for hydrogen storage¹⁸⁹.

3.8 Ta-based MXenes

It is observed that Ta-based nanomaterials are one of the most biocompatible with minute harmful biological impact¹⁹⁰. As a result, Ta-based MXenes with tuneable features are considered efficient candidates for bio-based applications. Synthesis of multilayered Ta-MXene Ta_4C_3 [Fig. 4(h)] can be carried out by the elimination of Al layer from the typical MAX phase Ta_4AlC_3 [Fig. 4(i)]¹⁸². Fine quantum dots of $Ta_4C_3T_x$ with a particle size of <5 nm diameter had been synthesized, exhibiting outstanding biocompatibility, high surface area, thermal stability, and steady suspension with minimal agglomeration¹⁹¹.

Tantalum is mainly explored in biomedical applications because the high atomic number of Ta (73) is associated with high image contrast which is beneficial for computed tomographic and X-ray imaging^{192, 193}. As bio-functionalities are advantageous for bio-based applications, soybean phospholipid-modified exfoliated Ta₄C₃ MXene nanosheets exhibited the potentiality of photoacoustic/computed tomographic imaging¹⁹⁴. Due to having 2D morphology, Ta-MXene can act as a suitable host matrix for the growth of superparamagnetic iron oxide nanoparticles on its 2D surface, and this combination has been used in breast cancer therapy¹⁹⁵. Additionally, the extraordinary conductive properties of Ta₄C₃ MXene offer efficient performance for supercapacitor¹⁹⁶, optoelectronics¹⁹⁷, and electrocatalyst for water splitting¹⁹⁸.

Table 2. Summary of different non-Ti-MXenes with their synthesis methods from corresponding MAX phases and major outcomes.

Non-Ti-	MAX phase	Synthesis	Major outcome and property	Ref.
MXene		parameter		
Mo-MXene				
Mo ₂ C	Mo ₂ Ga ₂ C	H ₃ PO ₄ used as etchant via UV-induced process	HF-free etching, fluorine-free high-quality MXene sheets, high-capacity flexible anode for batteries.	199
Mo_2CT_x	Mo ₂ Ga ₂ C	HF (50 %) for 7 days at 55 °C	Stable in acid, much enhanced catalytic activity compared to Ti_2CT_x	117
Mo ₂ C	_	$\begin{array}{c} \text{Chemical} \\ \text{conversion} & \text{of} \\ \text{MoS}_2 & \text{via} \\ \text{epitaxial} \\ \text{synthesis} \\ \text{method} \end{array}$	Unique electronic properties with sheet resistance of 123.6 Ω sq ⁻¹ and carrier concentration of 5.84 \times 10 ¹³ cm ⁻²	35
Mo_2CT_x	Mo ₂ Ga ₂ C		More stable against oxidation than Ti_2CT_x , $Ti_3C_2T_x$, V_2CT_x , and Nb_2CT_x ,	200

			stable broad photoresponse of thin film flexible Mo_2CT_x	
Mo ₂ N	_	Ammoniation of Mo_2CT_x at $600 ^{\circ}C$	Three times higher electrical conductivity than the Mo_2CT_x , stable MXene structure after ammoniation	201
Mo_2CT_x	Mo ₂ Ga ₂ C	Conc. HF at 140 °C for 4 days	Optimization of Ga elimination method, catalytic performance for water-gas shift reaction	202
V-MXene				
V_2CT_x	V ₂ AlC	HF (24 %) at 30	Contains V ₂ AlC residue,	203
		°C for 56 h	in-situ formation of nanoscale VO_x during the charging activation of Zn-ion batteries, converting surface V of cathode V_2CT_x from V^{2+}/V^{3+} to V^{4+}/V^{5+} keeping inner V-C-V layer intact	
V_2CT_x	V ₂ AlC	HF (50 %) for 8 h	$ \begin{array}{cccc} Contains & V_2AIC & residue, \\ functionalized & stacked & layers \\ restrict & the & capacitive \\ performance & \\ \end{array} $	204
V ₂ N	V ₂ AlN	HF (50 %) for 12 h at RT	Develop abundant reactive oxygen sites that eradicate bacteria (in vitro) and enhance the healing of subcutaneous abscesses (in vivo) with minimal toxicity	205
V_2CT_x	V ₂ AlC	HF (50 %) for 92 h at RT	Concentration of surface -OH and -O groups is higher than the	206

			-F groups which facilitates the
			gas adsorption efficiency
V_2O_x/V_2CT_x	V ₂ AlC	NaF + HCl at 90	Oxidation of vanadium during 131
		°C	high temperature etching and
			repetitive electrochemical
			process,
			formation of by-product of
			Na ₅ Al ₁₃ F ₁₄ as impurity
Amorphous	V_2AlC	HF (24 %) at 45	Controlled anodic oxidation of 207
V_2O_x/V_2C		°C for 96 h	multilayered V_2CT_x ,
			reversible V-O vibration and
			reversible valence state of
			V ⁴⁺ /V ⁵⁺ in disordered
			framework
Nb-MXene			
Nb_2CT_x	Nb ₂ AlC	HF (50 %) for 3	Work functions are regulated 208
		days at RT	by replacing surface -F groups
			with -NH ₂ using hydrazine,
			efficient additive for flexible
			perovskite solar cell
Nb_2C	Nb ₂ AlC	HF (40 %) for	Complete removal of Al layer, 209
		24 h	ultrafast reaction dynamics and
			nonlinear response
Nb_2CT_x	Nb ₂ AlC	HF (49 %) at 50	Contains unreacted Nb ₂ AlC ²¹⁰
		°C for 48 h	and residual Al-containing
			impurities,
			assessment of mechanical,
			electronic and surface
			properties

$Nb_4C_3T_x$	7 7	100 h at RT (20- 25 °C)	Large breakdown current density of $\sim 1.1 \times 10^8$ A cm ⁻² , evaluation of electronic properties	211
Nb ₂ C Cr-MXene	Nb ₂ AlC	HF (50 %) at 55 °C for 40 h	Complete removal of Al layer by acid etching, promising electrode material with high charge-discharge rate	137
Cr ₂ C	Cr ₂ AlC	NaF + 12 M HCl at 9 °C for h	Incomplete elimination of Al and contains residual salt impurities, Assessment of magnetic properties	212
Cr ₂ CT _x	Cr ₂ AlC	FeCl ₃ + tartaric acid for 3 h in dark and Ar environment	Contains Cr ₇ C ₃ as impurity, formation of insoluble alumina is restricted, evaluated the hydrogen sensing ability	166
W-MXene W _{1.33} CT _x	$(W_{2/3}Sc_{1/3})_2AlC,$ $(W_{2/3}Y_{1/3})_2AlC$	30 h at RT, LiF + HCl (12	Ordered divacancies of metal, contains residual MAX phase and other impurity phases like YAl ₃ C ₃ and Y ₂ O ₃ , evaluation of catalytic activity affected by the ordered divacancies	171
W _{1.33} C	$(W_{2/3}Sc_{1/3})_2AlC,$ $(W_{2/3}Y_{1/3})_2AlC$	HF (48 %)	Contains residual MAX phase, evaluation of electronic structure, stability, formation	213

			energy and energy storage capacity
W _{1.33} C	,	LiF + HCl (12 M) for 80 h at	Paramagnetic for $R = Lu$ -based 172 W-MXene
	Dy, Tm, Ho, and Lu	37 °C	complex magnetic moment arrangement for R = Dy, Tb, and Ho-based W-MXenes
			antiferromagnetic,
			assessment of electrochemical efficiency
W _{1.33} C	$(W_{2/3}Y_{1/3})_2AIC$	LiF + HCl (12 M)	Ordered divacancies of metal ²¹⁴ and preferable biodegradability or biocompatibility
Zr-MXene			
ZrC	-	Magnetron sputtering	Controlled direct synthesis of ²¹⁵ ZrC film,
		deposition	Evaluated the efficiency in mode-locked fiber laser and photonics
$Zr_3C_2T_z$	$Zr_3Al_3C_5$	HF (50 %) for 72 h at RT	Contains ZrC impurity residue, 216 superior thermal stability than $Ti_3C_2T_z$,
			assessment of mechanical, structural and electronic characteristics
Hf-MXene			
$\mathrm{Hf_3C_2T}_z$	Hf ₃ [Al(Si)] ₄ C ₆	HF etching	Contains residual 217 $Hf_3[Al(Si)]_4C_6$ MAX phase and little HfC impurities,

			evaluation of anodic performance for Li and Na-ion batteries	
Ta-MXene Ta ₄ C ₃	Ta ₄ AlC ₃	HF (40 %) for 4 days at RT	Nonlinear third-order optical 197 properties, evaluated contribution in mode- locked fiber laser	7
Ta ₄ C ₃	Ta ₄ AlC ₃	HF (40 %) for 3 days at RT	Surface modification with 194 soybean phospholipid which enhanced their biocompatibility and stability without toxicity, Evaluated biomedical application for in-vivo photothermal treatment of tumors and photoacoustic/computed tomographic imaging	4
Ta ₄ C ₃ T _x Sc-MXene	Ta ₄ AlC ₃	6 M HCl and the 6 M KOH	Fluorine-free etching, high concentration of -OH and - O terminal groups, 84 % elimination of aluminium, evaluated as a biocompatible material for supercapacitor	5
Sc-MXelle ScC _x OH	ScAl ₃ C ₃	Tetramethyl ammonium hydroxide (TMAOH, 25 wt%) at 30-40 °C for 72 h	Fluorine-free etching, detection of residual Al(OH) ⁴⁻ groups and intercalated TMA ⁺ ions	3

Sc ₂ CO _x	_	Magnetron sputtering	Direct preparation without any 21 MAX phase precursor or etchant, susceptive to oxygen, evaluated optical properties and photoluminescence	8
Y-MXene			photorummeseenee	
Y ₂ CF ₂	_		Direct preparation, high purity, 21 controlled -F functionalization, sensitive to air, assessment of electronic structure and sensitivity to oxygen	9
Y ₂ CF ₂		Solid state reaction of YF ₃ , YC, and Y ₂ C	Direct preparation, 222 Contains YF ₃ impurity and formation of carbonate and fluorocarbon moiety during photo-induced reaction, evaluation of photocatalytic activity	.0
YC_xT_δ	YAl ₃ C ₃	HF (10 %) for 24 h at RT, LiF + HCl (12 M) for 10 h	Residual Y ₂ O ₃ impurity, 22 feather-like nanoplate morphology, evaluation of electrochemical performance as electrode for energy storage	:1

3.9 Sc-based MXenes

Scandium has gained less interest as nanomaterial due to its low commercial availability and high cost²²². Thus, the utilization of expensive Sc-MXene compared to Ti-MXenes can only be justified by their versatile properties and notable performances. The precursor MAX phase

ScAl₃C₃ was synthesized by electric current pulsed sintering in-situ process. Hydroxyl group functionalized, 2D, carbon-deficient Sc-MXene ScC_xOH has been prepared from ScAl₃C₃ using organic base TMAOH as etchant [Fig. 4(j)]¹⁸³. The exfoliated 2D ScC_x nanosheets with hexagonal symmetry can be observed in SEM [Fig. 4(k)] and TEM [Fig. 4(l)] images¹⁸³.

The properties of Sc-MXenes like Sc₂CT₂ (T = O, OH, F, and Cl) were mostly predicted by first-principles calculation due to their limited experimental establishment²²³⁻²²⁵. For instance, Sc₂C(SH)₂, Sc₂CCl₂, and Sc₂NO₂ exhibited semiconducting properties²²⁶ while Sc₂CF₂ and Sc₂C(OH)₂ showed good optical absorption properties in the visible light range²²⁴. In another study, semiconducting Sc₂CF₂ exhibited high thermal conductivity of 472 W m⁻¹ K⁻¹ while less anisotropic Sc₂C(OH)₂ showed low thermal conductivity of 173 W m⁻¹ K⁻¹ which is still higher than silver²²⁷. Recently, a structural state of Sc₂CO₂ MXene with *C2/m* space group (C₃) has been discovered to be influenced by the antiferroelectric and hexagonal ferroelectric phase of Sc₂CO₂²²⁸. This new 2D C₃-structure of Sc-MXene is predicted to be a good candidate for lithium-ion battery anode. Therefore, Sc-MXene has versatile properties, which can make it a good opportunity to utilize them as potential candidates in different fields. However, a cost-effective method needs to be investigated for their experimental synthesis and practical application.

3.10 Y-based MXenes

There are minimal reports of precursor material for Y-MXene. A non-MAX phase system YAl_3C_3 consists of a matching crystal configuration with layered carbides with the formula of $T_mAl_3C_{2+m}^{184}$. There are two types of layers in this crystal configuration, one is Al_3C_2 layers similarly arranged like Al_4C_3 in layered ternary carbides with YC_2 slabs (T_mC_m) in NaCl-type configuration [Fig. 4(n)]. Experimentally, YAl_3C_3 was synthesized by sintering stoichiometric quantity of YC_2 and Al_4C_3 while Y_2O_3 , amorphous carbon, and $Y_4Al_2O_9$ were formed as byproducts²²⁹. Zhao et al. synthesized bulk YAl_3C_3 ceramic [Fig. 4(m)] using C, YH_2 , and Al_3C_3 as starting material at 1500 °C via an *in-situ* hot pressing method¹⁸⁴. On the other hand, a bottom-up method was followed to synthesize Y_2CF_2 via solid-state reaction at high temperatures to obtain direct crystal growth with only fluorine functionalized layers²¹⁹.

A superior thermoelectric property is obtained for YAl_3C_3 than Zr-Al-C and Zr-Al-Si-C ²²⁹. Meanwhile, the electronic property of Y_2CF_2 exhibited a semiconducting nature with an ionization potential of 3.8 eV, an indirect band gap of 1.6 eV, and a direct band gap of 1.9 eV. But the challenge associated with Y_2CF_2 is its sensitivity towards water and oxygen²¹⁹. Etching of YAl_3C_3 with HF followed by delamination with DMSO exhibited a specific capacitance of

18 F g⁻¹ while etching with LiF/HCl showed a specific capacitance of 6 F g⁻¹²²¹. The structural, optical, electronic, and thermal characteristics of Y-MXene and their practical applications were studied by first-principles study²³⁰⁻²³². It was observed that monolayer of Y_2C is associated with a low diffusion barrier of 0.01 eV with high Na adsorption energy of -0.32 eV and a large theoretical capacity of 564 mAh g⁻¹²³³.

As Y remains the least investigated metal among the M-MXenes, it is necessary to synthesize pure Y-MXene experimentally and evaluate its surface termination, characteristics, and stability. Further, it is important to test its efficiency in a wide range of applications.

4. Doped non-Ti-MXene

Theoretical and experimental approaches have been investigated for the engineering of MXene doping. Correspondingly, M, X, and T counterparts of MXene have been explored for doping either during MAX phase synthesis or after MXene synthesis. This type of doping is categorized as (i) M-site doped MXene, (ii) X-site doped MXene, and (iii) T-substituted MXene²³⁴. Halides have been used as substituents for T, heteroatoms like O, S, N, or P were incorporated in all three places (M, X, and T) while, semiconductors like Si, Ge, transition metals like Ru, Mo, Cr, and rare earth metal like Gd, La can be introduced in place of either or both X and M places in MXene lattice^{32, 102, 235, 236}. Doped MXenes with a wide range of diversity in stoichiometry and elemental composition within their lattice structure provide application in many areas due to their outstanding physical and chemical properties. Doping engineering of non-Ti-based MXenes including theoretical and experimental study with different strategies like in-situ and ex-situ, mechanisms, characterizations, properties, and corresponding challenges with further guidelines are discussed in the following section.

4.1 Theoretical study

One of the most promising methods to precisely control the properties and performance of MXene is by element doping via tuning their intrinsic structure at the atomic level²³⁵. To get an idea about the method and the element that is beneficial for doping to obtain better results, the blind experimental trial can be associated with enormous research prices. Thus, the theoretical calculation can predict the doping element, method, and structure, which can further enhance the performance of MXene as well as eliminate inconvenient methods. Accordingly, the experimental authentication following the theoretical predictions can hugely reduce unwanted costs for experimental attempts^{165, 237}. Generally, DFT has been used as a genuine theoretical method to predict the atomic level phenomena, but it is associated with few

restrictions including accuracy in predicting van der Waals force and band gaps. Therefore, to overcome such imperfections and get precise predictions, hybrid functional methods have been used combining advanced algorithms with correction functions. The simulation study of doping of MXene at different sites can predict band gap, bond energy, and bond length which helps deduce the properties of doped MXene.

4.1.1 Doping in M site

It is already an accepted fact that the unique properties of MXene are related to the vacant d-orbital of M atom and with increasing the size of M ($Hf_2CO_2 > Zr_2CO_2 > Ti_2CO_2$) the band gap of MXene increases, which directly affects their intrinsic properties²³⁸. The formation energy of double transition metal MXenes having sandwiched structure of two different transition metals having formula $M'_2M''C_2$ and $M'_2M''_2C_3$ (M' and M'' = V, Nb, Ta, Ti) have been predicted by theoretical calculation [Fig. 5(a, b)]¹⁰². Si et al. predicted quantum spin hall insulator $Mo_2MC_2O_2$ (M = Hf, Zr, Ti) in which oxygen terminations resulted in mutual electrostatic repulsion and resistance to oxidation²³⁹. In another study, Yang et al. studied the magnetic properties of $Cr_2MC_2T_2$ (M = V, Ti)²⁴⁰.

Recently, Jin et al. reviewed the catalytic performance of 18 double transition metal MXenes $M'_2M''_2C_3T_x$, $M'_2M''C_2T_x$ (M' and M" = Nb, V, Ta, Cr, Ti) for HER [Fig. 5(c)] and among them Mo₂NbC₂O₂ predicted to be the best electrocatalyst due to its smallest overpotential and near-zero Gibbs free energy (~0.003 eV)²⁴¹. In another study, an increment in Co-doping content in nonmagnetic Mo₂C from 3% to 8% increased the total magnetic moment from 1.2 to 2.03 µB²⁴². Ling et al. observed that doping with Co/Fe/Ni enhances the electrocatalytic performance of V₂CO₂²⁴³. In another study, incorporating transition metals like Au, Fe, Ag, Ni, Mn, Pd, Mo, and Ru induced the electrochemical activity of Cr₂CO₂^{168, 244}. Yang et al. predicted promising gas sensing activity of Mn-doped Sc₂CO₂ based on their change in resistance²⁴⁵. Another study suggested that inserting a single Pd atom with oxygen vacancy in defective Mo₂CO₂ can result in efficient material for CO oxidation²⁴⁶. The doped Pd atom can facilitate the electron transfer by acting as a reactive site from CO to O₂, leading to the dissociation of O-O bond and generation of CO₂. The bifunctional electrocatalytic activity obtained for Nb₂CT₂ after doping Pd/Pt as noble metals generally acts as excellent electrocatalysts, as well as the synergistic effect of both metals, enhances the electron donor ability²⁴⁷. Theoretical study also suggested that MXene annealing strategy at moderate temperature can enhance the degree of distribution of M atom and structural stability of MXene

²⁴⁸Therefore, doping or insertion of specific metal atoms into MXenes is anticipated to be a useful method for tuning their performance.

4.1.2 Doping in X site

The elemental doping of MXene in the X site has been less investigated compared to the doping in the M site, though it influences the properties of MXene significantly. The theoretical study predicted Sc₂C(OH)₂ substitutionally doped with Ge/Si as a topological insulator, and this study revealed a new band inversion mechanism involving s and p-d orbitals²⁴⁹. Balci et al. investigated the electronic property of X (Ge, Si, Sn, B, B+N, S, F, and N)-doped Sc₂CF₂ where C atoms get substituted²⁵⁰. The study revealed that S, F, N-substituted monolayer of Sc₂CF₂ with C monovacancy transited to metal from semiconductor while Ge, Si, Sn, B, B+N-substitute one consists of band gap within 0.24 to 0.55 eV. The total energy calculation indicated that the substitution of the C atom by Ge, Si, and Sn is less permittable, while S, F, N, and B+N doping are favorable. It was interesting to note that, the B-doped Sc₂CF₂ showed spin polarization due to a half-filled defect band. It was also concluded that the different heteroatom substitutions in the precursor Sc₂AlC MAX phase is an exothermic process.

Like the M site, in transition metal carbonitrides (M_3CN) X site can also consist of two elements. Huang et al. studied the HER mechanism of various transition metal-based carbonitrides M_3CN (M=Zr, Ta, Nb, Ti, Hf, V, Mo)²⁵¹. Among all non-Ti-based carbonitrides only Nb₃CNO₂ was predicted to be an efficient electrocatalyst due to its free energy of hydrogen adsorption [Fig. 5(d)]. In another study, Ding et al. also reviewed the electrochemical activity of heteroatom-doped Mo_2CO_2 -X (X=B, N, S, and P)²⁵².

Table 3. Summary of the theoretical studies on doping/substitution of non-Ti-based MXenes in M, X, and T positions with their corresponding application/characteristics.

Doping site	Non-Ti-MXene	Doping element	Properties/Application	Ref.
	MWCO ₂	Mo, Cr	Electrocatalyst	253
	V_2CO_2	Co, Fe, Ni	Electrocatalyst	243
	M_2CO_2 (M=V etc.)	3d, 4d, or 5d	Electrocatalyst	254
		transition metal		
	$MVCO_2$	Zr, Hf, Ti, Nb, Ta	Electrocatalyst	253
	Sc_2CT_2	V, Ti, Mn, Cr	Electronic and magnetic	255
	$(M'_{1-x}M''_{x})_{3}C_{2}$	M'=V, Ta, Ti, Nb	Stability	248

		M"=Nb, V, Mo,		
		Та		
	$Cr_2MC_2T_2$	V, Ti	Magnetic and electronic	240
	Mo ₂ C	Co	Magnetic and electronic	242
M site	$Mo_2MC_2O_2$	Zr, Ti, Hf	Electronic	239
	$M'_2M''C_2$	M'=W, Mo	Electronic	256
		M"=Zr, Ti, Hf		
	Mo ₂ CO ₂	Pd	Oxidation of CO	246
	Cr_2CO_2	Co, Ag, Fe, Au,	Electrocatalyst	244
		Mn, Ir, Mo		
	Nb ₂ CT ₂	Pd, Pt	Electrocatalyst	247
	Mo_2CO_2	Cu	Oxidation of CO	257
	M_2CO_2 (M=Sc	Mn	CO adsorption	245
	etc)			
	Cr_2CO_2	Co, Ni	Electrocatalyst	168
	Mo ₂ C	B, S, P, N	Electrocatalyst	252
X site	Sc_2CF_2	Ge, F, Si, N, B, S,	Electronic	250
		B+N		
	$Sc_2C(OH)_2$	Ge, Si	Electronic	249
	V_2NT_2	S	Na/Li-ion batteries	258
	M_2XT_2 (M=Cr, Sc,	S	Electronic and stability	259
	V, Zr; X=C, N)			
T site	W ₂ CO ₂ , Mo ₂ CO ₂	В	Electrocatalyst	260
	$Nb_{n+1}C_{n}T_{2} \\$	OH, F, O, OCH_3	Work function	261
	Zr_2CT_2	O, F, S	Electronic	177
	Cr ₂ CTT'	Cl, H, F, OH, Br	Electronic and Magnetic	262

4.1.3 Doping in T site

Surface functional group T also significantly influences the properties of MXene. Other than the common surface terminal groups (-O, -F, -OH) like halogen (Br and Cl), chalcogen (Se, S, and Te), and metal have been investigated as elemental substitution on MXene surface. Electronic properties and stability of 20 types of sulfur terminalized MXene M₂XS₂ (M=Sc, V, Ti, Hf, Nb, Zr, Mo, W, Cr, and Ta; X=C and N) were systematically studied by Yang et al.²⁵⁹. Among them, phonon frequency study and molecular dynamic analysis predicted that the most dynamically stable S-substituted MXenes are Cr₂NS₂, Hf₂CS₂, V₂CS₂, Nb₂CS₂, and Ta₂CS₂ [Fig. 5(e)]. According to the formation enthalpy, stable 2D Ta₂CS₂, V₂CS₂, Hf₂CS₂, and Nb₂CS₂ structures are easy to synthesize, and Cr₂NS₂ is comparably challenging to prepare. On the other hand, Nb₂CS₂, V₂CS₂, and Cr₂NS₂ bilayer structures can be easily converted to monolayers due to their smaller binding energy (<0.18 eV atom⁻¹), while Hf₂CS₂ and Ta₂CS₂ are not easy to convert into monolayers due to their higher binding energy. Hybrid functional DFT calculation indicated the semiconducting property of Ta₂CS₂ with a direct band gap of 0.36 eV and the ferromagnetic property of Cr₂NS₂ with a magnetic moment of 1.60 μB. Therefore, S termination influences the property of MXene and can broaden their application areas.

In another study, Zhu et al. demonstrated that substituted MXenes can be helpful for battery applications ¹⁷⁷. Theoretical simulation of Zr₂CT₂ where T=S, F, OH, Se, O, and Te indicated that Zr₂CS₂ has potential for Li-ion batteries due to the high conductivity and rate capability. Recently, Shukla et al. studied S-substituted V₂NS₂ as an anode material for Li/Na ion batteries due to their low diffusion barrier and high adsorption energy for Li/Na ions²⁵⁸. The theoretically predicted capacity of V₂NS₂ for Li storage was 299.5 mAh g⁻¹. Asymmetrically functionalized MXene Cr₂CTT' was also investigated theoretically by He et al. where T and T'= Cl, H, Br, F, and OH ²⁶². Those 2D asymmetrically functionalized Janus Cr₂C MXene with zero magnetization and high Néel temperature exhibited fully spin-polarized semiconductivity. The band gap of these MXenes can efficiently be tuned by types as well as proportions of the surface functionalities and a very high Néel temperature of 400 K was calculated for Cr₂CHF, Cr₂CFCl, Cr₂CHCl, Cr₂CClBr, and Cr₂CFOH.

It was also predicted by Xin et al. that surface functionalization significantly affects the work functions of MXene²⁶¹. It was observed that the introduction of the -OCH₃ functional group on the surface of $Nb_{n+1}C_n$ (n=1, 2, 3, and 4) drastically reduces its work function to 1.0 eV. Thus, $Nb_{n+1}C_n(OCH_3)_2$ can be utilized in electron emission devices and organic electronics with this extremely low work function. In another report, Zheng et al. investigated

the electrochemical performance of B-doped MXenes where B atoms were preferably inserted into the O vacancy sites and bonded strongly on the MXene surface because of their large binding energy (>2 eV)²⁶⁰. The B-doped W₂CO₂ and Mo₂CO₂ exhibited potential for catalytic activity with limiting voltages of -0.24 and -0.20 V.

Table 3 summarises the theoretical studies on doping/substituting non-Ti-based MXenes in M, X, and T positions with their corresponding applications/characteristics. The above discussion indicates that there are plenty of theoretical investigations on doping/substitution of non-Ti-MXenes, and doping significantly affects the property and lattice structure of MXene based on stoichiometry. However, the computation simulation on doping in X and T sites is comparatively rarer than the doping in the M site and needs further effort to design their practical implementation.

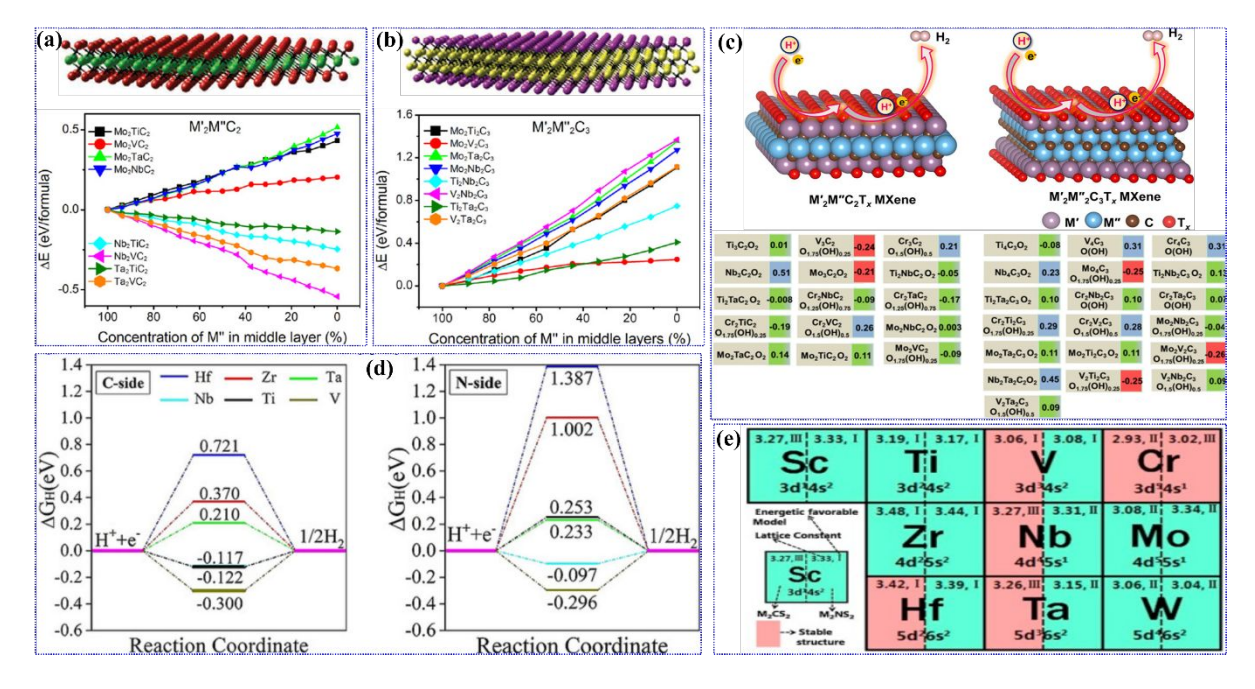


Fig. 5. Predicted stabilities of (a) M'₂M"C₂ and (b) M'₂M"₂C₃, (c) calculated Gibbs free energy of double transition metal MXenes, (d) free energy diagram for C-side and N-side of MXenes, (e) energetically favorable configurations and lattice parameter of M₂XS₂ with various models. (a, b) Reproduced from ref¹⁰² with permission from American Chemical Society, copyright 2015, (c) reproduced from ref²⁴¹ with permission from American Chemical Society, copyright 2020, (d) reproduced from ref²⁵¹ with permission from Wiley-VCH, copyright 2018, (e) reproduced from ref²⁵⁹ with permission from Elsevier, copyright 2018.

4.2 Experimental study

Doping can be achieved experimentally following two methods such as ex-situ (top-down) and in-situ (bottom-up) pathways via compositional engineering of 2D MXene layers. Ex-situ (for

example solvothermal/plasma/heat treatment) method generally involves post-synthesis transformation which permits doping/substitution at X or/and T according to the applied circumstances and the heteroatom. The in-situ (for example via sintering) strategy involves the incorporation of a dopant during the synthesis of 3D MAX phase which is the precursor of MXene, and then selective etching and delamination can result in doped MXenes. Generally, this method includes substitution at M or/and X place according to the dopant and transition metal used³². According to the dopants used, the experimental doping methods are divided into two sections such as non-metal doping and metal doping which are elaborately discussed in the following section including the determination of doping via different characterization methods. Different doping strategies are represented in Fig. 6(a), and Fig. 6(b) shows different characterization techniques used to detect doping in MXene.

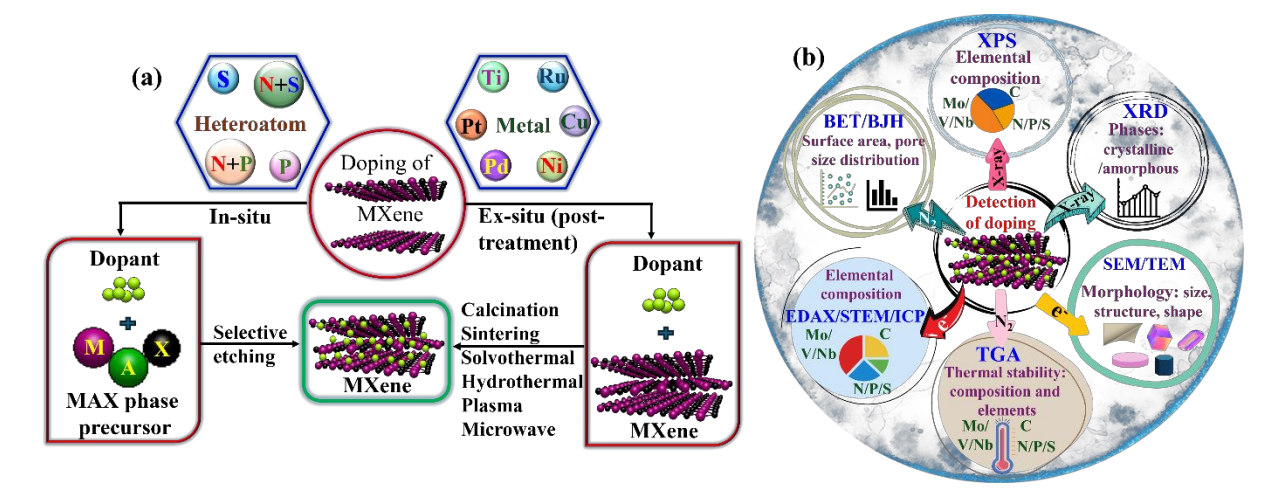


Fig. 6. (a) Schematic representation of methods of heteroatom doping of MXene, and (b) various characterization techniques generally used to detect doping in MXene.

4.2.1 Non-metal doping

Non-metal doping of non-Ti-based MXenes includes doping with N, S, P, or dual atoms (N and S, N and P). Table 4 summarizes the non-metal doping of non-Ti-MXenes with different heteroatoms and their sources, strategies, and benefits of doping.

4.2.1.1 Doping with N

Nitrogen is one of the components of the MXene category like in carbonitrides (M_3CN) and nitrides ($M_{n+1}N_n$, n=1-3). However, it is hard to synthesize stable nitride MXene via conventional acid etching methods because of the large formation energy and unsteady M-N bond. On the other hand, modification with nitrogen via doping or substitution is feasible experimentally by both ex-situ and in-situ methods which can further incorporate versatile properties in MXene.

Several methods have been developed to synthesize heteroatom doped-MXene following in-situ or ex-situ strategies. Among various sources, ammonia is the most widely used reagent for N-doping in MXene and has been directly employed to prepare nitride MXenes like V₂N and Mo₂N. It was observed that the electrical conductivity of V₂N and Mo₂N was remarkably higher than their carbide precursors²⁰¹. Thermal annealing method was used to prepare N-doped $V_4C_3T_x$ under NH₃ environment²⁶³. With increasing the annealing temperature, the nitrogen concentration in $V_4C_3T_x$ increases, which is confirmed by the V-N bond intensity in X-ray photoemission spectroscopy (XPS) analysis [Fig. 7(a, b)]. Besides ammonia, nitrogenous organic materials or nitric monomers like urea, 2-methylimidazole, melamine, and other organic amines have also been widely used for N-doping in MXene. Among them, urea is a low-cost, biocompatible, and environment-friendly material that has been used as a source of N-doping as well as intercalant in MXene materials. Liu et al. employed urea to synthesize N-doped Nb₂CT_x via facile hydrothermal approach ²⁶⁴. Nitrogen doping resulted in enhancement in interlayer spacing of 1.25 nm (calculated from XRD analysis) for ~4.5% nitrogen content (obtained by XPS) in N- Nb₂CT_x shown in Fig. 7(c, d). Also, the SEM elemental mapping clearly showed the distribution of N over the Nb₂CT_x sheets which further confirms the doping [Fig. 7(e)]. In a recent study, exfoliated N-doped Nb₄C₃T_x coated with N-doped graphitic carbon was synthesized [Fig. 7(f)] via pyrolysis under argon environment as an efficient electrocatalyst for overall water splitting²⁶⁵. By controlling the mass ratio between Nb-MXene and hexamethylenetetramine which was used as an N source, the nitrogen concentration and properties of the composite were tuned.

In another study, phenylamine was used as nitrogen resources to prepare N-doped Mo₂C via hydrothermal followed by thermal annealing method²⁶⁶. The electrocatalytic efficiency was enhanced after N-doping in Mo₂C. Recently, dicyandiamide was used as an N-source to prepare N-Mo₂C via calcination under Ar/H₂ environment²⁶⁷. Nitrogen doping increased the surface area of MXene and the obtained porous nanosheets with ~1 nm thickness [Fig. 7(g)] exhibited outstanding electrocatalytic performance. Chi et al. reported a core-shell porous structure of N-doped Mo₂C/carbon spheres via carbonization using aniline and pyrrole as N resources [Fig. 7(h)]²⁶⁸ and the N insertion in Mo₂C/carbon resulted in superior HER performance. Therefore, N-doping enhances electronic conductivity and electrochemical performance because of its increased density of states at the Fermi level. Nitrogen doping in Mo-based MXenes has been studied mostly via experimental strategy compared to the other non-Ti-MXenes.

4.2.1.2 Doping with S

Sulfur doping of MXene can also be achieved via both in-situ and ex-situ strategies like nitrogen doping. Chen et al. reported the incorporation of sulfur into Mo₂TiC₂T_x structure by annealing the mixture of S and Mo₂TiC₂T_x in an inert environment²⁶⁹. The Mo-O bond was converted to form MoS₂ via this in-situ sulfidation strategy [Fig. 7(i)] and the S-doped MXene exhibited stable Li-ion storage efficiency. Ang et al. reported S-doped Mo₂C via carburization and chemical conversion using sodium thiosulfate as the source of sulfur²⁶⁶. The S-doped Mo₂C delivered good electrocatalytic performance compared to pristine Mo₂C and N-doped Mo₂C due to the more electron donation capability of S than more electronegative N which acted as an electron acceptor from Mo.

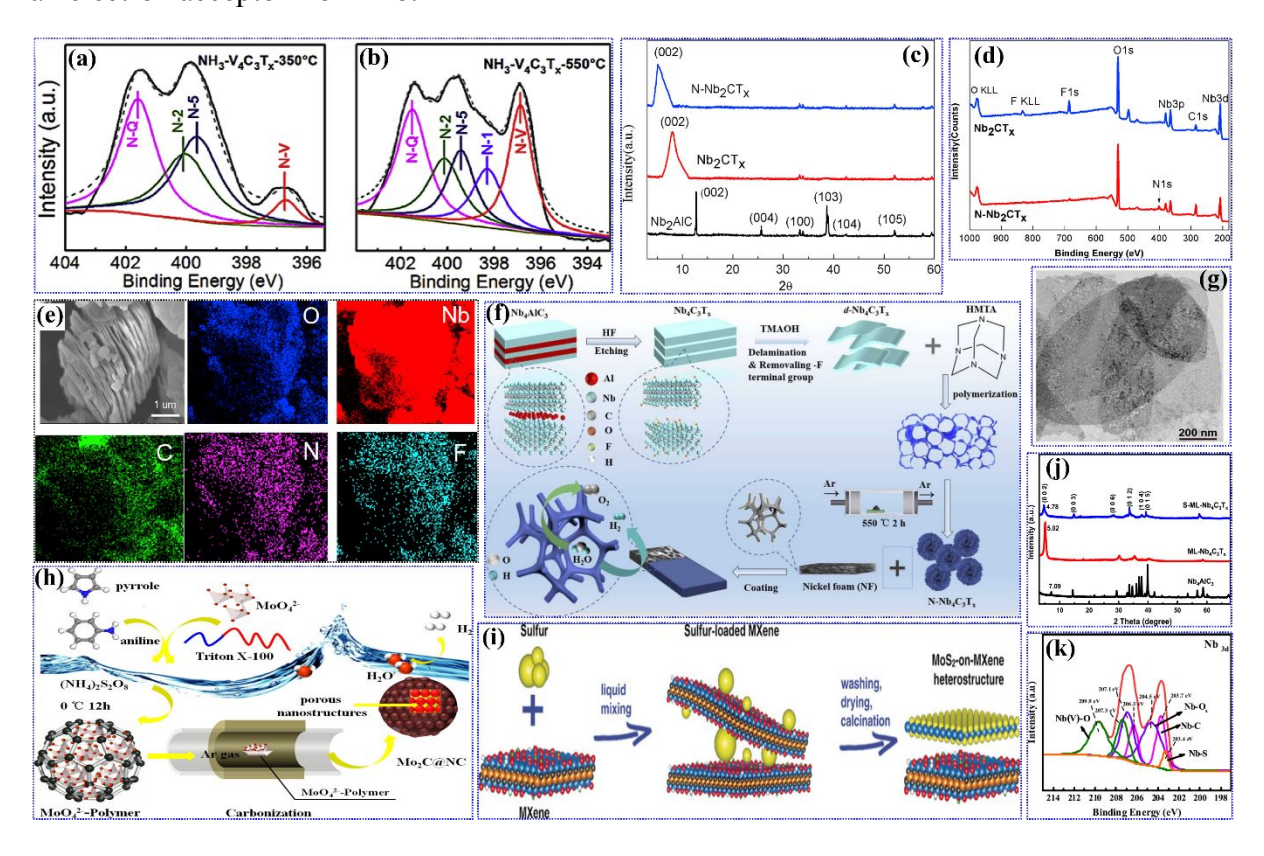


Fig. 7. High-resolution XPS spectra of N 1s for (a) N-V₄C₃T_x at 350 °C, (b) N-V₄C₃T_x at 550 °C, (c) XRD spectra of Nb₂AlC, Nb₂CT_x, and N-Nb₂CT_x, (d) XPS patterns of Nb₂CT_x, and N-Nb₂CT_x, (e) SEM and EDS mapping of O, Nb, C, N, and F of N-doped Nb₂CT_x, (f) formation of N-Nb₄C₃T_x coated with N-doped graphitic carbon, (g) TEM of porous N-Mo₂C, (h) formation of N-doped Mo₂C/carbon spheres, (i) S doping strategy in Mo₂TiC₂T_x, (j) XRD spectra of Nb₄AlC₃, multilayered Nb₄C₃T_x, and S-doped Nb₄C₃T_x, (k) high-resolution XPS spectrum of Nb 3d for S-doped Nb₄C₃T_x. (a, b) Reproduced from ref²⁶⁴ with permission from Elsevier, copyright

2019, (f) reproduced from ref²⁶⁵ with permission from Elsevier, copyright 2024, (g) reproduced from ref²⁶⁷ with permission from American Chemical Society, copyright 2017, (h) reproduced from ref²⁶⁸ with permission from Elsevier, copyright 2018, (i) reproduced from ref²⁶⁹ with permission from Wiley-VCH, copyright 2018, (j, k) reproduced from ref²⁷⁰ with permission from Elsevier, copyright 2022.

Recently, Wu et al. synthesized multilayered S-doped Nb₄C₃T_x via hydrothermal method using Na₂S as a sulfur source²⁷⁰. The heterostructure obtained after S-doping which prevented the restacking of 2D layers is confirmed by the XRD analysis [Fig. 7(j)] exhibiting the highest left shifting of (002) plane for S-doped Nb₄C₃T_x. An extra peak of Nb-S (203.4 eV) was observed in the deconvoluted XPS spectra [Fig. 7(k)] of Nb 3d for S-doped Nb₄C₃T_x compared to undoped Nb₄C₃T_x which confirms the doping. Doping tuned the electronic structure of Nb₄C₃T_x and facilitated the electron mobility resulting in enhanced electrochemical performance of S-doped Nb₄C₃T_x. In another study, sulfidation of Mo₂C via in-situ hydrothermal method in a microwave oven was carried out using thioacetamide as a sulfur source²⁷¹.

4.2.1.3 Doping with P

The lower electronegativity (2.19) and bulkier size of phosphorous than N (3.04) and S (2.58) significantly impact the electronic structure of P-doped MXenes resulting in enhanced intrinsic properties²⁷². Shi et al. synthesized nanowires of P-doped Mo₂C combined with conducting carbon via simple pyrolysis of MoO_x-phytic acid-polyaniline hybrid in inert environment ²⁷². The electronic, structural, and compositional tuning of Mo-based MXene due to the controlled P-doping (P=2.9%) of the resulting P-Mo₂C@C nanowires exhibited efficiency in electrochemical performances.

A facile phosphorization strategy [Fig. 8(a)] was followed by Qu et al. to incorporate P into Mo₂CT_x by annealing Mo₂CT_x with red phosphorus under Ar environment at 550 °C for 30 min with 10° min⁻¹ flow rate²⁷³. The incorporation of P into Mo₂CT_x resulted in an increment in interlayer spacing indicated by the left shifting of (002) shown in Fig. 8(b). EDS mapping analysis revealed [Fig. 8(c-e)] the uniform distribution of P over the P-doped Mo₂CT_x. XPS study also confirms the P doping in P-Mo₂CT_x with the increment in P concentration compared to the undoped Mo₂CT_x. Additionally, the deconvoluted Mo 3d peak and P 2p_{3/2} peak exhibited the formation of Mo-P bond (228.1 and 231.6 eV) and P-Mo bond (129.4 eV), respectively confirming the P doping in Mo-MXene. In another study, P-doped V₂CT_x was synthesized via heat treatment where triphenylphosphine was used as the precursor of P [Fig. 8(f)]¹²⁴. It was

observed that P-doping (3.83-4.84 at%) at the basal plane resulted in an increment in the electrocatalytic performance of V_2CT_x . Guo et al. developed a new method to dope phosphorus in multilayered 3D V_2C composited with NiCo-layered double hydroxide²⁷⁴. NaH₂PO₂ was used as a phosphorus precursor and calcinated with $V_2C/NiCo$ -layered double hydroxide to synthesize the P-doped vanadium MXene nanocomposite which was used as anode material for Li-ion batteries. It is observed that N-doping in MXene is more widely studied than the S and P doping. Thus, there is huge scope for S and P doping in MXene materials to tune their structure, properties, and performance in various fields.

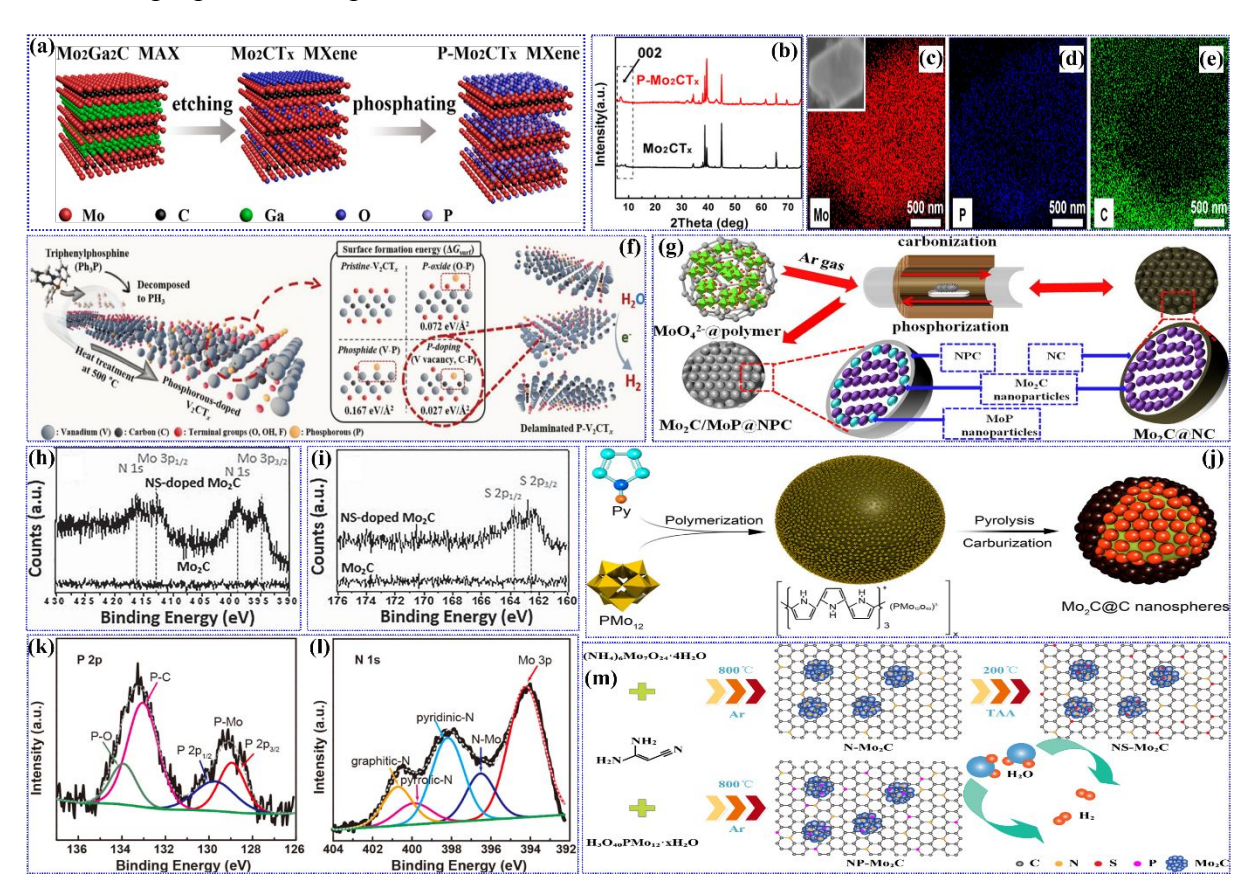


Fig. 8. (a) Formation of Mo₂CT_x and P-Mo₂CT_x, (b) XRD patterns of Mo₂CT_x and P-Mo₂CT_x, EDS elemental mapping of (c) Mo, (d) P, (e) C of P-Mo₂CT_x, (f) preparation of P- V₂CT_x, (g) synthesis of Mo₂C/MoP@N and P doped carbon, high-resolution XPS patterns of N, S codoped Mo₂C for (h) N 1s and Mo 3p, (i) S 2p, (j) synthesis of N, P doped Mo₂C@C nanosphere, high-resolution XPS spectra of N, P doped Mo₂C@C nanosphere for (k) P 2p, (l) N 1s, (m) formation of NP-Mo₂C and NS-Mo₂C. (a-e) Reproduced from ref²⁷³ with permission from American Chemical Society, copyright 2018, (f) reproduced from ref¹²⁴ with permission from Wiley-VCH, copyright 2019, (g) reproduced from ref²⁷⁵ with permission from Elsevier, copyright 2018, (h, i) reproduced from ref²⁶⁶ with permission from Wiley-VCH, copyright

2015, (j-l) reproduced from ref²⁷⁶ with permission from American Chemical Society, copyright 2016, (m) reproduced from ref²⁷⁷ with permission from Elsevier, copyright 2018.

4.2.1.4 Dual doping

The incorporation of two different heteroatoms (N and P/N and S) into MXene results in the generation of higher defects, which provides enhanced active sites and tuned interlayer spacing. Doping with two heteroatoms can trigger coordination of one metal atom into the material which may amplify their property and diversify their area of application. These doping processes are generally influenced by the position of heteroatom dopant (e.g. surface adsorption, carbon lattice substitution, and functional substitution), extent of heteroatom doping, and variety of bond generation of heteroatom with resident C, Ti, O/H/F²⁷⁸. Chi et al. reported N and P doped core-shell Mo₂C MXene combined with MoP and N and P doped carbon and it was observed that doping enhanced the electrocatalytic performance of MXene²⁷⁵. First, Mo₂C/nitrogen-doped carbon spheres were prepared using aniline and pyrrole as nitrogen sources via pyrolysis under Ar atmosphere. Then, NaH₂PO₂ was used as a phosphorous precursor and calcined at 750 °C with Mo₂C/nitrogen-doped carbon spheres under Ar atmosphere for 2 h to obtain the N and P co-doped Mo-MXene [Fig. 8(g)].

In another study, Ang et al. prepared N and S co-doped Mo₂C using thioacetamide as a heteroatom source via carburization at 700 °C under H₂/Ar atmosphere²⁶⁶. The deconvoluted XPS spectra of S 2p revealed the formation of Mo-S bond (162.4 and 163.6 eV) while N 1s (397.7 and 416.3 eV) and Mo 3p (394.7 and 412.8 eV) peaks indicated the formation of Mo-N shown in Fig. 8(h, i). Chen et al. produced N and P dual-doped Mo₂C/carbon nanospheres with pomegranate-like morphology which delivered extraordinary electrocatalytic performance²⁷⁶. Phosphomolybdic acid and aniline were used as P and N precursors, respectively and the doped MXene nanospheres were obtained by a carbothermal reduction method [Fig. 8(j)] at 800 °C at 10 min⁻¹ Ar flow for 3 h. The doping of N and P was confirmed by the XPS analysis from the deconvoluted N1s (396.4 eV) and P 2p (129.5 and 130.4 eV) peaks designated to N-Mo and P-Mo bonds, respectively [Fig. 8(k, 1)]. In another report, N, P and N, S co-doped Mo₂C was synthesized, and it was studied that incorporation of P and S into the N-doped Mo₂C enhanced its electrochemical efficiency²⁷⁷. Dicyandiamide, phosphomolybdic acid, and thioacetamide were used as N, P, and S precursors, and the synthesis process is shown in Fig. 8(m). XPS analysis confirmed the heteroatom doping ascribed by N-Mo, S-Mo, and P-Mo bond peaks.

Table 4. Non-metal doping of non-Ti-MXenes with different heteroatoms and their sources, strategies, and benefits of doping.

Dopant	Non-Ti-	Source	Benefit of doping	Strategy	Ref.
_	MXene			_	
	$N-V_4C_3T_x$	NH ₃	Capacitance enhancement	Annealing	263
Nitrogen	N-Nb ₂ CT _x	Urea	Enhance capacity for Li-ion battery	Hydrothermal	264
	$N-Nb_4C_3T_x$	Hexamethylenetet ramine	Boost electrocatalytic efficiency	Pyrolysis	265
	N-Mo ₂ C	Phenylamine	Boost electrocatalytic efficiency	Hydrothermal followed by annealing	266
	N-Mo ₂ C	Dicyandiamide	Enhance electrocatalytic activity	Calcination	267
	Core shell N- $Mo_2C/carb$ on sphere	Aniline and pyrrole	Enhance charge transfer rate as electrocatalyst	Carbonizatio n	268
	N-Nb ₂ CT _x	NH ₃	Tune the electronic structure to enhance electrocatalytic activity	Annealing	279
	S-Mo ₂ C	Sodium thiosulfate	Enhance electrocatalytic activity	Carburization	266
	MoS_2 - $Mo_2TiC_2T_x$	Sulfur	Stable Li-ion storage	Calcination	269

Sulfur	S-multilayere d $Nb_4C_3T_x$	Na ₂ S	Enhance electrocatalytic activity	Hydrothermal	270
	MoS_2 - Mo_2CT_x	Thioacetamide	Enhance electrocatalytic activity	Microwave assisted hydrothermal	271
	S- Mo ₂ C/carb on cloth	Thiourea	Enhance electrocatalytic activity for wide pH range	Annealing	280
	P- Mo ₂ C@C	Phytic acid	Enhance electrocatalytic activity	Pyrolysis	272
Phospho	P-Mo ₂ CT _x	Red phosphorus	Improve electrocatalytic performance	Annealing	273
rus	V ₂ C/NiCo- layered double hydroxide	NaH ₂ PO ₂	Stable anode for Li- ion battery	Calcination	274
	P-V ₂ CT _x	Triphenyl phosphine	Enhance electrocatalytic performance	Heat treatment	124
	N , S - V_2CT_x	Thiourea	Enhance the efficiency as anode for Li-ion battery	Heat treatment	281
N 1 C	N, S-Mo ₂ C	Thioacetamide	Boost electrocatalytic efficiency	Carburization	266
N and S	N, S-Nb ₂ C	Thiourea	Improve electrochemical sensing	Heat treatment	282

	N,	S-	Thiourea	Improve the hydrogen	Heat	283
	Nb_2CT_x			storage property of	treatment	
				MgH_2		
	N,	P-	Aniline, pyrrole,	Boost electrocatalytic	Pyrolysis	275
	Mo_2C/M	loP	and NaH ₂ PO ₂	efficiency		
	/carbon					
	nanosph	ere				
	N,	P-	Phosphomolybdic	Boost electrocatalytic	Carbothermal	276
	Mo ₂ C/carb acid and		acid and aniline	efficiency	reduction	
N and P	on					
	nanosph	ere				
	N, P ((S)-	Dicyandiamide,	Boost electrocatalytic	Carbonizatio	277
	Mo ₂ C/ca	arb	phosphomolybdic	efficiency	n	
	on		acid, and			
	nanosph	ere	thioacetamide			

4.2.2 Metal doping

Although metal doping or substitution in MXene has been widely studied via theoretical simulation, experimental synthesis remains challenging due to the lack of facile synthesis methods. Incorporating metal ions in MXene crystal regulates its intrinsic properties and induces irreversible structural changes, offering diversified applications in different fields. Table 5 summarizes metal doping of non-Ti-MXenes with the strategies and benefits. Differently ordered double-M stoichiometric MXenes like Cr₂TiC₂, Mo₂TiC₂, Cr₂VC₂, Mo₂ScC₂, Mo₂M₂C₃ (M=V, Ti, or Nb) have been synthesized from their corresponding MAX phases via in-situ method^{102, 236}. Zhou et al. reported that alloying with Ti can effectively increase the exfoliation of (V_{1-x}Ti_x)₂C from its precursor MAX phase (V_{1-x}Ti_x)₂AlC (x=0.1, 0.2, and 0.3) which was prepared by facile elemental mixing followed by sintering²⁸⁴. This result was also confirmed by another study after two years where Ti concentration was tuned by 50% and both studies revealed that Ti-doped V-based MXene exhibited efficient activity for Li-ion batteries²⁸⁵. Peng et al. reported enhancement in the electrocatalytic activity of Mo₂CT_x after doping with atomic Ru²⁸⁶. Ru-doped Mo₂CT_x synthesized via simple agitated stirring which offered higher active sites for the adsorption of electroactive intermediate which

can promote the catalytic activity by reducing the thermodynamic energy barrier. TEM elemental mapping [Fig. 9(a)] of Ru-doped Mo_2CT_x clearly showed the incorporation of Ru inside Mo_2CT_x .

A metal/Mo₂C catalyst was prepared by wetness infusion followed by high-temperature reduction under an H₂ environment²⁸⁷. Various transition metals like Pt, Cu, Pd, Ag, and Ni had been infused into Mo₂C and it was assumed that carburization at 600 °C resulted in Pt/Mo alloy formation. In another study, Li et al. showed a reactive metal support reaction between Pt and Nb₂CT_x²⁸⁸. The heat treatment at 350 °C resulted in a reduction of surface terminal groups of Nb-MXene and the formation of a Pt/Nb surface alloy. In a recent study, Kuznetsov et al. demonstrated a two-step synthesis method to prepare Co substituted Mo₂CT_x where Co(NO₃)₂.6H₂O was mixed with molybdenum precursor via sintering and then Ga was incorporated to form Mo₂Ga₂C:Co via annealing¹¹⁹. Selective acid etching with HF prepared Co-substituted Mo₂CT_x with Co content of ~0.4 wt%. EDS mapping shows the presence of Co over the hexagonal Mo-MXene, which confirms the Co doping [Fig. 9(b)]. Tao et al. reported rare earth (RE) metal incorporated solid *i*-MAX phases (Mo_{2/3}RE_{1/3})₂AlC (RE=Pr, Gd, Ce, Nd, Dy, Sm, Tb, Tm, Er, Ho, and Lu) and studied their magnetic properties²⁸⁹.

Table 5. Summary of metal-doped non-Ti-MXenes with the strategies and benefits.

Non-Ti-MXene	Dopant	Strategy	Benefit of doping	Ref.
	metal/source			
Mo ₂ CT _x :Co	Co(NO ₃) ₂ .6H ₂ O	Carburization	Enhance catalytic activity	119
$(V_{1-x}Ti_x)_2C$	Ti	Sintering	Better exfoliation and Li-	284
			ion battery performance	
$(V_xTi_{1-x})_2C$	Ti	Sintering	Enhance Li-ion storage	285
			performance	
$Ru-Mo_2CT_x$	Ru	Agitated stirring	Enhance electrocatalytic	286
			activity	
Metal/Mo ₂ C	Au, Pt, Pd, Ni,	Carburization	Enhance catalytic	287
	Ag, and Cu		performance	
$Pt-Nb_2CT_x$	$Pt(NO_3)_2(NH_3)_4$	Heat treatment	Enhance catalytic	288
			performance	

$Mo_2Ti_2C_3T_x$	Ti	Sintering	Enhance	thermoelectric	236
			power		
$(Ti_{0.5}V_{0.5})_3C_2$	Ti	Sintering	Boost cata	lytic activity	290
$Mo_2TiC_2T_x$	Ti	Sintering	Enhance	electrochemical	102
			performan	ce	
$Pt-Mo_2TiC_2T_x$	Pt	Electrochemical	Enhance	catalytic	291
		exfoliation	performan	ce	

5. Functionalization of non-Ti-MXene

Controlling the surface functional groups of MXene other than the conventional -F, -OH, -O, or -Cl can diversify the application of MXene by regulating their surface properties. The hydrophilic surface of MXene provides the active centers for covalent binding with polymers, surface active initiators, and small molecules. Various studies have been carried out on the chemical surface functionalization of Ti-based MXenes with suitable groups to enhance their efficiency according to the required application. Table 6 summarizes different types of surface functionalization of non-Ti-MXene with their synthesis methods, reaction parameters, and benefits.

5.1 Functionalization by small molecules

Surface functionalization by different small molecules following simple, inexpensive strategies can regulate characteristics like electrical conductivity, mechanical stability, and solution stability of MXene. DFT simulation established that the –OCH₃ terminated Nb₂C MXene are applicable for field emitters due to their low work function $(1.0 \text{ eV})^{261}$. Jin et al. demonstrated a solvothermal strategy to modify the surface of Nb₂CT_x MXene nanosheets obtained by HF etching with various solvents²⁹². Ethanol (Et) and deionized water (DI) were used as solvents for an environment-friendly solvothermal method at 100 °C for 10 h [Fig. 9(c)] and it was observed that solvent functionalized MXenes have exfoliated layers while there is stacked morphology for the HF etched Nb₂CT_x [Fig. 9(d-i)]. Also, layer spacing for Et- Nb₂CT_x is much larger than the DI- Nb₂CT_x which resulted in enhanced dielectric loss and high electromagnetic wave absorption. The functional groups at the edges and surfaces of Nb₂CT_x can function as polarization sites to absorb the electromagnetic energy.

In a recent study, amino (-NH₂) functionalized Nb₂CT_x was synthesized and tested its performance in photoelectric devices²⁰⁸. The surface –F groups were replaced by –NH₂ groups via simple hydrazine treatment [Fig. 9(j)] and the resulting NH₂-Nb₂CT_x was used in a flexible perovskite solar device with high power conversion efficiency. Sabaghi et al. reported a grafting strategy on V₂C MXene surface using multifunctional azobenzene sulfonic acid and the resulting functionalized V₂C MXene behaved as an anode material for energy storage devices ²⁹³. The starting material for the covalent grafting was 4-aminoazobenzene-4′-sulphonic acid [Fig. 9(k)] and the method included amine diazotization followed by corresponding diazonium removal process [Fig. 9(l)]. This grafting method with organic molecules offered facile K⁺ hopping centers and K⁺ storage sites while acting as a safeguard between the V₂C layers, which eliminates the structural disintegration during intercalation/deintercalation of K⁺ ion [Fig. 9(m, n)]. Fig. 9(o) shows the delamination of V₂C nanosheets due to the functionalization and HRTEM [Fig. 9(p, q)] reveals the increment in interlayer spacing of 0.39 nm due to the incorporation of functionalities between V₂C layers.

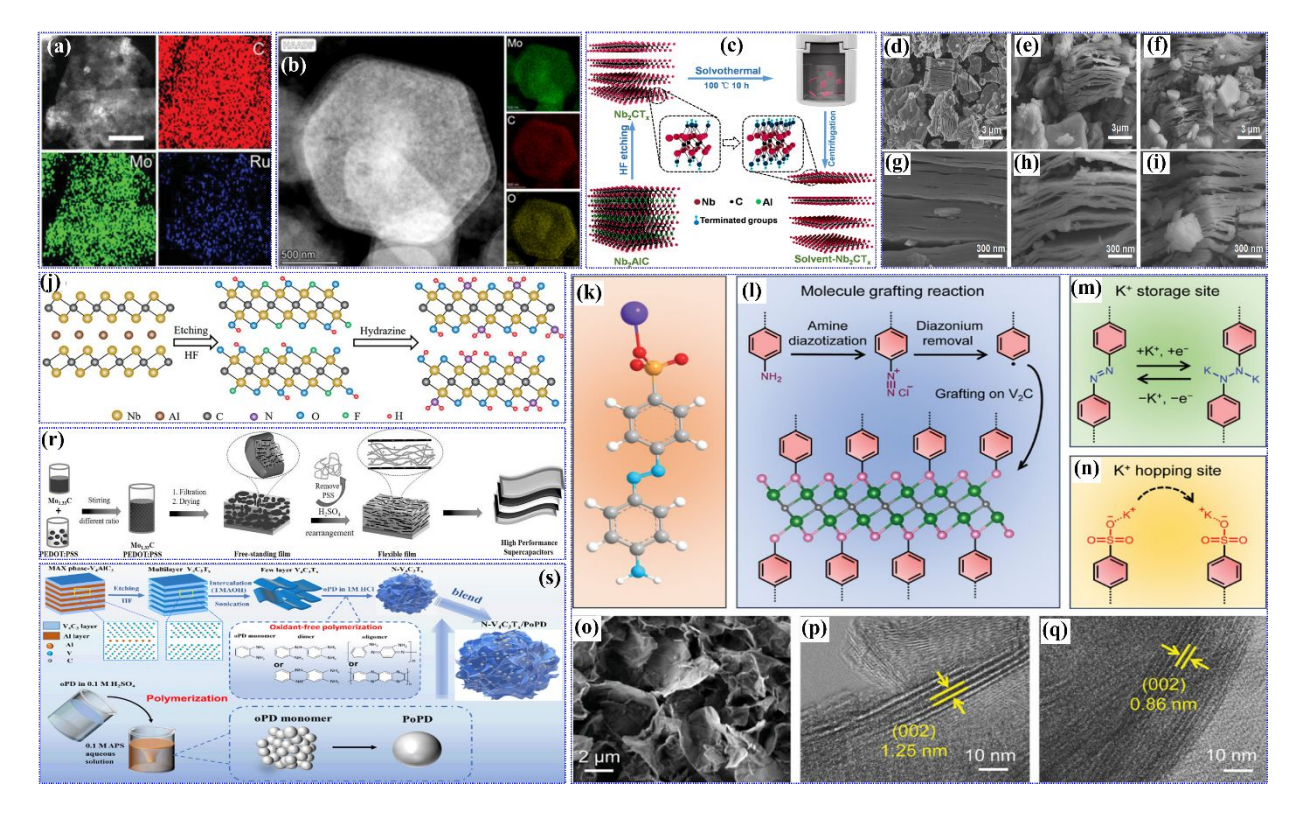


Fig. 9. (a) STEM-EDS mapping of Ru-doped Mo_2CT_x , (b) HAADF-STEM and elemental mapping of Mo_2CT_x :Co, (c) synthesis of Nb_2CT_x and functionalization via solvothermal method, FESEM of (d, g) Nb_2CT_x , (e, h) Et- Nb_2CT_x , (f, i) DI- Nb_2CT_x , (j) preparation method of NH_2 functionalized Nb_2CT_x , (k) schematic of 4-aminoazobenzene-4'-sulfonic acid sodium salt (sphere color: white-H, grey-C, blue-N, orange-S, red-O, purple-Na), (l) molecule grafting

reaction (black-C, green-V, pink-terminals of V₂C), (m) azobenzene unit as the extra K⁺-storage site, (n) sulfonate anion as the K⁺-hopping site, (o) SEM of functionalized V₂C, HR-TEM images of (p) functionalized V₂C and (q) pristine V₂C, (r) synthesis scheme of PEDOT:PSS functionalized Mo_{1.33}C, (s) synthesis of N-V₄C₃T_x/PoPD blend. (a) Reproduced from ref²⁸⁶ with permission from Wiley-VCH, copyright 2020, (b) reproduced from ref¹¹⁹ with permission from American Chemical Society, copyright 2019, (c-i) reproduced from ref²⁹² with permission from Elsevier, copyright 2019, (j) reproduced from ref²⁰⁸ with permission from Wiley-VCH, copyright 2022, (k-q) reproduced from ref²⁹³ with permission from Wiley-VCH, copyright 2018, (s) reproduced from ref²⁹⁵ with permission from American Chemical Society, copyright 2023.

5.2 Functionalization with heteroatoms

Significant improvement in electrochemical properties has been achieved by functionalizing the MXene surface with heteroatom, which leads to an increment in layer spacing by reducing the self-restacking. Wang et al. designed a S functionalized V₂C which exhibited good thermal and dynamic stability as well as metallic conductivity²⁹⁶. It was observed that V₂C with S functionalization is associated with a low shuttle effect and restricts the dissolution of lithium polysulfides compared to the bare V₂C and V₂CO₂. V₂CS₂ acted as an efficient anchoring material for high-performance Li-S batteries.

A theoretical investigation by Mehta et al. reported S functionalized Mo₂C using DFT which suggested its efficiency as an anode material for Li-ion batteries²⁹⁷. Functionalization with S atom on Mo-MXene remarkably enhanced the Li adsorption energy on the functionalized monolayers which is associated with less diffusion barrier and high charge storage capacity of Li-ion batteries. Another theoretical study demonstrated the superconducting property of S functionalized Nb-MXene (Nb₃C₂S₂) as both bulk and monolayer forms with a transition temperature of around 28 K²⁹⁸.

Table 6. Different types of surface functionalization of non-Ti-MXene with their synthesis methods, parameters, and properties or applications.

Type of	Functionalized	Preparation	Benefit of	Ref.
functionalization	non-Ti-MXene	method and	functionalization	
		parameters		
	CH ₃ O-Nb ₂ C	DFT simulation	Enhance ²	261
			capacitance and	

			field-emission
			ability
	$Et-Nb_2CT_x$	Solvothermal at	Superior 292
		100 °C for 10 h,	electromagnetic
		solvent-Ethanol	wave absorption
By small	NH_2 - Nb_2CT_x	Hydrazine (N ₂ H ₄)	Enhance 208
molecules		treatment	photoelectric
morecures			performance
	Azobenzene	4-	Potential anode ²⁹³
	sulfonic acid -V ₂ C	Aminoazobenzene-	for K ⁺ ion storage
		4'-sulphonic acid	
		covalently grafted	
		via amine	
		diazotization	
		followed by	
		corresponding	
		diazonium removal	
	V_2CS_2	DFT simulation	Promoted 296
			electrochemical
			activity as
			anchoring
By heteroatom			material for Li-S batteries
2	M. GG		
	Mo_2CS_2	DFT simulation	Elmanee charge
			storage capacity of Li-ion batteries
	$Nb_3C_2S_2$	DFT simulation	mauce
			superconductivity
	PEDOT:PSS-	Treated with	Enhance stability, ²⁹⁴
	Mo _{1.33} C	PEDOT:PSS and	conductivity and
		then vacuum	capacitance

		filtered and treated with H_2SO_4		
	PoPD/V ₄ C ₃ T _x /PoP D	In-situ polymerization and mechanical mixing	Boost storage capacity	295
By macromolecules	Poly(2- (dimethylamino) ethyl methacrylate)- V ₂ C	Self-triggered photografting and photopolymerizatio n	-	299
	Soybean phospholipid-Ta ₄ C ₃	Thin film approach	Enhanced their biocompatibility and stability without toxicity for biomedical research	194

5.3 Functionalization with macromolecules

The hydrophilic functional groups on the MXene surface arise due to the conventional etching method allowing in-situ polymerization or ex-situ blending of polymers. Electrostatic interaction and hydrogen bonding effectively enhance the interconnection between MXene and al. synthesized of poly(3,4polymers. Qin et flexible film ethylenedioxythiophene):poly(styrenesulfonic acid) (PEDOT:PSS) functionalized Mo_{1.33}C MXene [Fig. 9(r)]²⁹⁴. Concentrated H₂SO₄ was used for post-treatment of the free-standing film to etch out PSS, and the obtained functionalized MXene film delivered excellent performance for flexible supercapacitor devices. The enhanced stability and capacitance were observed after functionalization which was attributed to the increment in interlayer spacing of Mo_{1.33}C due to the incorporation of conducting PEDOT and the surface redox contribution due to the interaction between PEDOT and MXene.

In a recent investigation, Cheng et al. reported poly(o-phenylenediamine) (PoPD) functionalized $V_4C_3T_x$ as an efficient electrode material for high-capacity Li-ion batteries and supercapacitor²⁹⁵. First, $V_4C_3T_x$ was combined with oPD via oxidant-free in-situ

polymerization and then mechanically mixed with PoPD to obtain the V-MXene/polymer composite blend [Fig. 9(s)]. The PoPD nanoparticles play the role of interlayer pillar to prevent the layer stacking of $V_4C_3T_x$ sheets which facilitate the ion transport and boost the charge storage performance. A brush-like polymer grafting of poly(2-(dimethylamino)ethyl methacrylate) over the V_2C MXene nanosheets was explored following a self-triggered photografting and photopolymerization by Chen et al.²⁹⁹. The polymer grafting calibrated the conductivity and transmittance of V_2C and converted the resulting hybrid into a smart MXene system.

Surface functionalization of MXene can resist oxidation, restrict layer restacking, resist abrasion, provide mechanical strength, flexibility, electrochemical and thermal stability, increase conductivity by tuning energy bands, and induce optical and magnetic properties. The versatility incorporated by the surface functional groups according to the requirement for the application amplifies the interest in research on MXene. Although there are plenty of investigations that have been carried out on the functionalization of Ti-based MXenes experimentally, surface tuning beyond Ti-MXenes is still not properly explored experimentally due to a lack of facile strategies. Therefore, there is considerable scope to examine and regulate the surface properties of non-Ti-MXenes for their diversified range of applications.

6. Flexibility of MXene

MXene materials show enhanced flexibility and durability when combined with other compounds. Flexible MXene papers used as freestanding electrodes are limited mainly by their mechanical instability during continuous cyclic study. To utilize their fullest potential as flexible material MXenes are generally combined with graphene-based materials, CNTs, carbon fibers, cellulose, conducting polymers, and porous hydrogels. The limitation of layer restacking resulting in low conductivity, small surface area, and poor capacitance can be eliminated by incorporating an interlayer spacer. These types of heterostructures bring flexibility, stability, resilience, lightweight, mechanical strength, abundant surface-active sites, and available electrolyte movement pathways. Additionally, incorporating/substituting heteroatoms like N, S, and P and tuning surface functional groups enhance their property and stability. The following section briefly discusses various methods reported to prepare MXene-based flexible architectures.

6.1 Vacuum filtration

Vacuum-supported filtration method using polypropylene membrane is commonly used to fabricate freestanding flexible MXene paper electrodes. The hydrogen bonding between MXene layers and the additives used as the spacer and binder leads to the stable and compact MXene film with efficient mixing of different components. These freestanding films are associated with good mechanical stability and flexibility toward bending and folding without any deformation. Further, the stable MXene papers obtained via vacuum filtration can be converted into 3D morphology of MXene materials. The self-assembly of MXene sheets can be eliminated by layer-by-layer filtration using a nanofiller which can provide extra spacing between the MXene sheets and assure flexibility by preventing self-restacking³⁰⁰.

6.2 Coating

Flexible electrodes can be prepared by coating the MXene dispersion over flexible templates, which may contain various functional characteristics. The shape of the coated electrode is completely adaptable to the shape of the template and the extent of electrostatic interaction between the template and MXene surface ensures the feasible coating. An ultrathin uniform coating of MXene material can be obtained via spin-coating method at around 100 to 1000 rpm. Alternatively, blade-casting has also been used to prepare MXene film of controlled thickness by adjusting the height of the blade and concentration of dispersion. This method is useful for large-scale production of flexible electrodes. Some other commonly used coating methods are dip coating, spray coating, and drop casting to get thin MXene film over the template³⁰⁰.

6.3 Spinning

Electrospinning and wet spinning are the two advanced techniques to obtain flexible fibers with large MXene concentrations. Electrospinning is a one-step method to get nonwoven fabric via the application of a high potential between the substrate and the top of the injector. The kind of solvent can regulate the morphology and diameter of the obtained flexible fibers, the concentration of MXene dispersion, electric field intensity, and the distance between substrate and injector. A net-like woven fabric with good flexibility and mechanical strength can be obtained through electrospinning by using a volatile solvent. On the other hand, long fibers can be obtained following a wet spinning strategy by extruding the dispersion from the injector and immersing the extrudate in a coagulation bath. Another polymer additive or conducting component is needed to be introduced with MXene to ensure continuous fiber formation as the large bending stiffness and low aspect ratio of MXene nanosheets³⁰⁰.

6.4 Printing

Printing has become a universal and precise strategy to obtain flexible devices for energy applications. Printing includes various categories including, 3D printing, stamping, inkjet printing, roll-to-roll printing, patterned coating, screen printing, pen-based writing, and direct ink writing. The feature of the printed device mainly depends on the substrate's characteristics and the ink's viscosity. Ink with much lower viscosity can become uncontrollable and over fluidly while high viscosity results in a thick layer of printing and increases the chance of nozzle blockage. This versatile printing method using multicomponent MXene ink has been utilized for fabricating MXene-based flexible Li-ion micro-batteries, micro-supercapacitors, and solar cells. Screen printing and 3D printed cylindrical stamping have also been used for fashioning planner flexible supercapacitors with variable patterns and high-performance³⁰¹.

7. Recent applications in flexible and wearable electronics

The following section discusses the recent applications of flexible non-Ti-based MXenes and their functionalized and doped versions in energy storage, energy harvesting, and wearable health monitoring. Table 7 summarises the implementation of flexible non-Ti-MXenes in various wearable electronic devices.

7.1 Energy storage

The current development in propelling flexible and wearable electronic devices has been transformed by the evolution of lightweight, portable, and flexible energy storage devices like supercapacitors and batteries.

7.1.1 Supercapacitors

Hybrid supercapacitors are associated with high power density, good cyclic stability, moderately high energy density, and good rate performance, but a few factors like toxicity, reliability, cost-effectiveness, safety, and durability also need to be considered. MXene is already a well-established electrode material for supercapacitors due to its high surface area, stability, and electrical conductivity. MXene-based flexible supercapacitors are generally designed by combining MXene with graphene, carbon fiber, CNT, and porous materials. Non-Ti-MXene-based supercapacitors reveal excellent flexibility over various bending angles making it suitable for flexible and wearable electronics [Fig. 10(a, b)]³⁰².

Qin et al. reported a hybrid paste of $Mo_{1.33}C$ i MXene combined with PEDOT:PSS to fabricate a fiber-like asymmetric supercapacitor which delivered a high specific capacitance of 105 F g⁻¹ and exhibited quick response time as well as large transconductance³⁰³. The porous fiber [Fig. 10(d)] electrode was prepared via the spinning method [Fig. 10(c)] and PVA/H₂SO₄

was used as a gel electrolyte for assembling the flexible fiber-shaped device [Fig. 10(e)]. A flexible film electrode of delaminated $V_4C_3T_x$ prepared by vacuum filtration on mixed cellulose ester membrane 304 . The delaminated $V_4C_3T_x$ film was used as flexible and stable negative electrode for an asymmetric supercapacitor with a good energy density of 22.2 Wh L⁻¹. In a recent study, Shen et al. demonstrated $NiCo_2O_4/Nb_2CT_x$ heterostructure-based flexible supercapacitor electrodes which showed large capacity, high stability, and excellent flexibility 305 . That unique heterojunction was obtained by combining hydrothermal and calcination methods which regulate the electronic structure as well as electrical conductivity of the flexible composite.

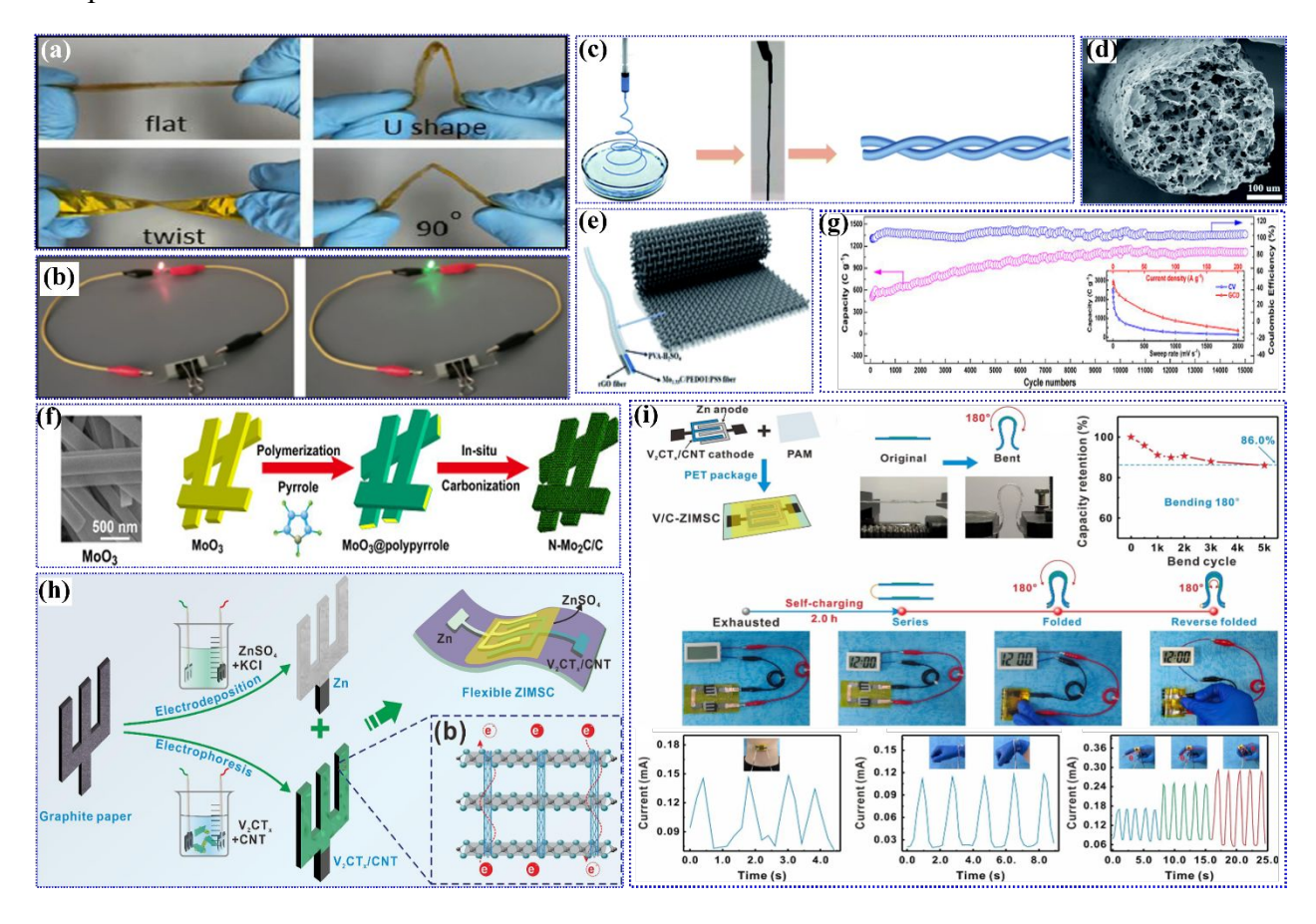


Fig. 10. (a) Flexibility of the supercapacitor device at different status, (b) practical application of the flexible supercapacitor device by operating red and green LED, (c) fabrication of hybrid MXene fiber, (d) SEM of cross-section of hybrid MXene fiber, (e) asymmetric fiber-like supercapacitor, (f) SEM image of MoO₃ and preparation of N-Mo₂C/C nanobelt, (g) cyclic study of N-Mo₂C/C nanobelt with gravimetric capacity plots after cyclic study in inset, (h) fabrication of V₂CT_x/CNT-based flexible Zn-ion micro-supercapacitor, (i) practical application of flexible Zn-ion micro-supercapacitor (a, b) Reproduced from ref³⁰² with permission from Elsevier, copyright 2022, (c-e) reproduced from ref³⁰³ with permission from Royal Society of

Chemistry, copyright 2022, (f, g) reproduced from ref³⁰⁶ with permission from Royal Society of Chemistry, copyright 2020, (h, i) reproduced from ref³⁰⁷ with permission from Elsevier, copyright 2024.

Zhu et al. explored the efficiency of 1D tunnel-like zig-zag N-doped Mo₂C nanobelt, and this type of flexible structure provides a framework for pseudocapacitance and facilitates promising ion diffusion³⁰⁶. Polypyrrole was used as the source of N for the preparation of flexible N-doped Mo₂C via carbonization [Fig. 10(f)]. The incorporation of nitrogen into the MXene system leads to an increment in specific surface area than the initial reagent MoO₃, which helps to accommodate the volume change during fast charging-discharging, resulting in a stable cyclic performance after 15,000 cycles [Fig. 10(g)]. Another electrode material for flexible supercapacitors has been demonstrated by incorporating CNT into Mo₂C and W₂C³⁰⁸. In a recent study, Wu et al reported a zinc-ion-based micro-supercapacitor using free-standing V₂CT_x/CNT prepared via electrophoretic deposition [Fig. 10(h)]³⁰⁷. The introduction of 1D CNT into the 2D V-MXene system enhanced the conductivity as well as reduced the ion/electron transport pathway, resulting in an excellent specific capacitance of 246.88 mF cm² at a current density of 0.5 mA cm⁻². The assembled micro-supercapacitor showed efficient self-charging abilities and utilized as self-powered and stable wearable body movement sensor [Fig. 10(i)].

7.1.2 Batteries

Non-Ti-based MXenes have been emerging as potential candidates for flexible battery electrodes mainly in sodium-ion (SIBs), lithium-ion (LIBs), and lithium-sulfur (LSBs) batteries. Like the flexible MXene electrodes for supercapacitors, different graphene, CNT, carbon nanofibers, nanorod, or porous materials have been integrated into non-Ti-MXenes to incorporate flexibility and robustness, resulting in hierarchical nanohybrid with minimum volume change and abundant ion transport channels.

7.1.2.1 Lithium-ion batteries (LIBs)

A novel Se-functional Nb-MXene Nb₂CSe₂ prepared via a direct vapor-active process was employed as a flexible electrode for fast-charging LIBs while combined with CNTs³⁰⁹. The surface termination with Se enhanced the conductivity of Nb₂CSe₂ around 2000 times and provided extra redox active sites facilitating Li-ion storage. The Nb₂CSe₂/CNT free-standing paper electrode showed good flexibility as shown in Fig. 11(a, b), and the robustness of flexible charge-discharging LIBs is shown in Fig. 11(c, d). Li et al. reported a phase evolution study by annealing MoO₂/polyacrylonitrile nanofibers fabricated via electrospinning [Fig. 11(e)] and

obtaining Mo₂N and Mo₂C while increasing the temperature from 580 °C to 900 °C resulting in carbon nanofibers containing both Mo₂N and Mo₂C³¹⁰. The Mo₂N and Mo₂C containing carbon nanofibers exhibit excellent flexibility, shown in Fig. 11(f, g), and exhibit excellent stability towards LIBs due to the buffering effect of carbon nanofibers while continuous charging-discharging Fig. 11(h).

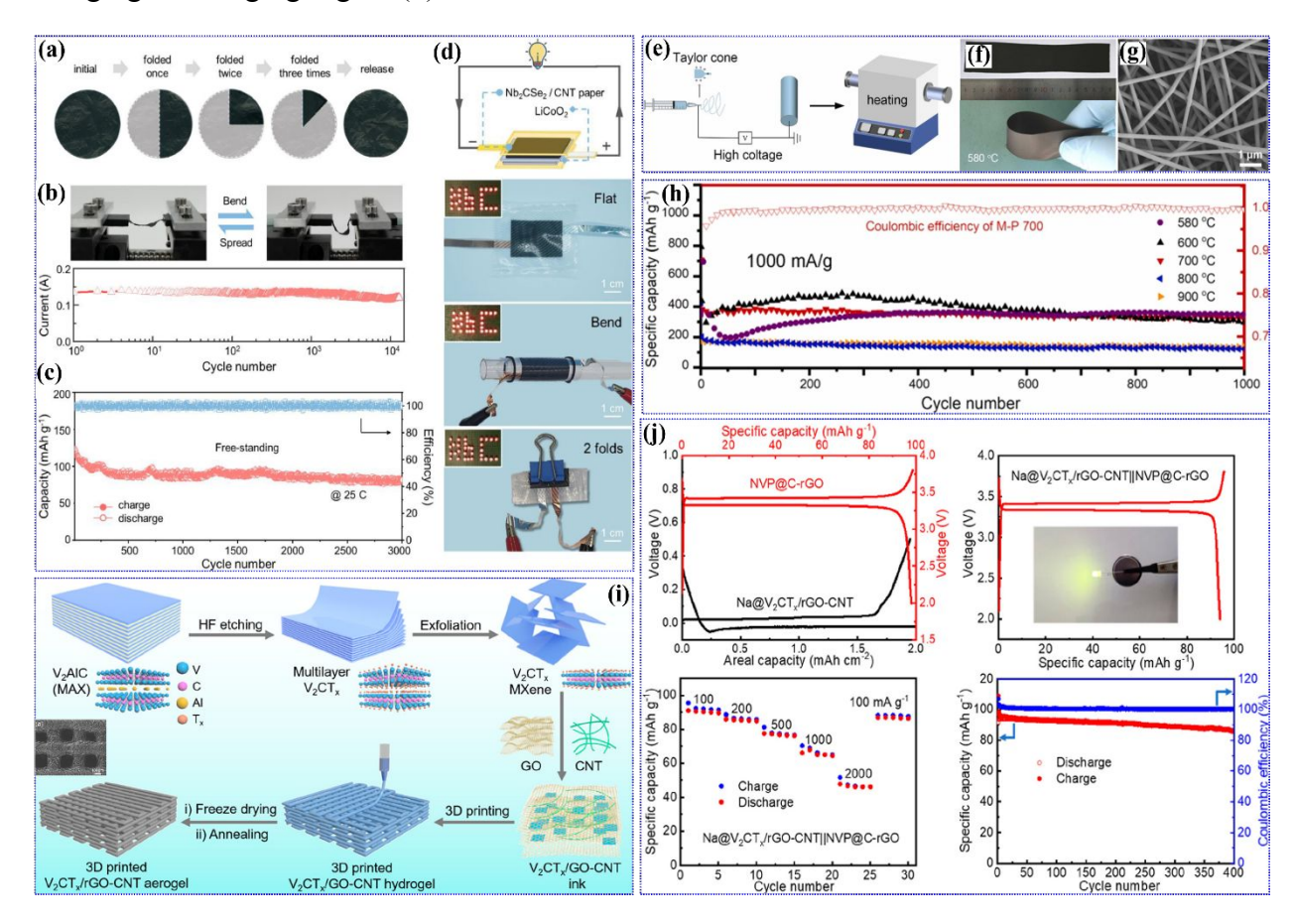


Fig. 11. (a) Nb₂CSe₂/CNT paper at different folding states without fracture, (b) stable electrical property during bend-spread cycles, (c) cyclic stability study of Nb₂CSe₂/CNT paper, (d) flexible full LIB, (e) electrospinning synthesis method, (f) flexibility, (g) SEM image, and (h) stable LIB performance of carbon nanofibers containing both Mo₂N and Mo₂C, (i) synthesis of 3D printed V₂CT_x/rGO-CNT aerogel and its SEM image, (j) full cell SIB performance using Na-V₂CT_x/rGO-CNT as anode. (a-d) Reproduced from ref³⁰⁹ with permission from Elsevier, copyright 2023, (e-h) reproduced from ref³¹⁰ with permission from Elsevier, copyright 2023, (i, j) reproduced from ref³¹¹ with permission from American Chemical Society, copyright 2022.

7.1.2.2 Sodium-ion batteries (SIBs)

A hierarchical 3D porous V_2CT_x/rGO -CNT aerogel microgrid was prepared via the direct ink writing printing method [Fig. 11(i)]³¹¹. The flexible electrode delivered a very stable cyclic life for 3000 h with 99.54 % coulombic efficiency. Theoretical DFT study established that

abundant sodiophilic terminal groups of V_2CT_x facilitate the sodium metal nucleation and homogeneous deposition leading to a dendrite-free surface. Additionally, the combined sodiated Na- V_2CT_x/rGO -CNT as anode in full cell SIB delivered an excellent reversible capacity of 86.27 mAh g⁻¹ at 100 mA g⁻¹ after 400 cycles [Fig. 11(j)]. Yang et al. reported a 3D architecture of rGO-wrapped N-doped carbon spheres combined with Mo₂C nanoparticles [Fig. 12(a)]³¹². The conducting coating of nitrogen-doped carbon stabilizes the structure, enhances the electrolyte penetration, and reduces volume expansion and diffusion barrier, improving the battery capacity and stability [Fig. 12(b)].

7.1.2.3 Lithium-sulfur batteries (LSBs)

An interwind nanosheet nanoribbon heterostructure of V₂C/VO₂ was fabricated and utilized as a flexible cathode for LSBs³¹³. This flexible self-supported film electrode facilitates ion/electron transport and reduces the shuttling effect of lithium polysulphide, leading to high areal capacity and excellent stability under arbitrary bending situations. Mao et al. reported a flexible self-supported sulfur host Mo₂C/carbon cloth (Mo₂C/CC) via simple solvothermal method [Fig. 12(c)]³¹⁴. The 3D architecture of Mo₂C/CC with more active size and large empty space helps to accommodate volume expansion of sulfur to Li₂S₂/Li₂S, and good adsorption efficiency of highly conducting Mo₂C MXene helps to restrict the shuttle effect of lithium polysulphides by forming Mo-S bonds. The catalytic performance of Mo₂C helps to facilitate electron transfer and boost the direct change of polysulphides to Li₂S₂/Li₂S on the surface leading to an amazing specific capacity of 1213 mAh g⁻¹ at 0.1 C with stable cyclic life [Fig. 12(d)]. The practical application of the flexible pouch cell in different bending states is shown in Fig. 12(e).

Table 7. Flexible non-Ti-MXene electrodes for wearable electronics.

MXene		Application	Performance	Ref.
material	flexible			
	electrode			
Nb ₂ CT _x @CC	Drop-casting of	Al-ion	Specific	315
	ink over CC	supercapacitor	capacitance=122 F g ⁻¹ ,	
			energy density=33.2	
			Wh kg-1, stability=90%	
			after 400 cycles	

V ₈ C ₇ /rGO	Laser scribing	Microsupercapacitor	Areal capacitance=49.5 mF cm ⁻² , volumetric energy density=3.4 mWh cm ⁻³	316
$Nb_4C_3T_x$	Membrane filtration	Supercapacitor	Volumetric capacitance=1075 F cm ⁻³ at 5 mV s ⁻¹	317
Mo _{1.33} CT _z - cellulose	Vacuum filtration	Supercapacitor	Specific capacitance=97 F g ⁻¹ , stability=95 % after 30,000 cycles.	318
Mo ₂ Ti ₂ C ₃	Vacuum filtration using polypropylene membrane	Supercapacitor	Specific capacitance=152 F g ⁻¹ , specific energy=188 Wh kg ⁻¹	319
Nb ₂ Se ₂ C/CNT	Filtration	LIBs	Storage capacity=221 mAh g ⁻¹ at 1 A g ⁻¹	320
$V_2O_x@V_2CT_x$	Pasting the ink over graphite foil	Zinc-ion batteries	Reversible capacity=304 mAh g-1 at 0.05 A g-1, stability=81.6 % after 200 cycles	321
$V_4C_3T_x$	Pressing onto stainless-steel mesh	SIBs	Initial irreversibility=128 mAh g ⁻¹	322
CeO ₂ /V ₂ C	In-situ polymerization	TENG (NH ₃ sensor)	Recovery value=36.8%@50 ppb NH ₃ , detection limit=25 ppb NH ₃ , stability=>60 days.	323
PVDF/V ₂ C	Electrospinning	PENG	Open circuit=124 V, short circuit=2.2	324

μAmps with manual single tapping, mechanical stability=>3000 cycles

*CC-carbon cloth, rGO-reduced graphene oxide, CNT-carbon nanotube, SIBs-sodium-ion batteries, LIBs-lithium-ion batteries, TENG-triboelectric nanogenerator, PVDF-polyvinylidene fluoride, PENG-piezoelectric nanogenerator.

7.2 Energy harvesting

Triboelectric nanogenerators have been considered cost-effective, lightweight, portable, human-friendly, and self-powered mechanical harvesters. Influenced by different dynamic human body motions, triboelectric nanogenerators transform kinetic energy into electricity. The working principle of triboelectric nanogenerators is based on the fusion of electrostatic induction and triboelectrification between different materials. Harvesting mechanical energy in a triboelectric nanogenerator occurs by taking two electrodes in contact under various configurations like single-electrode mode, in-plane sliding mode, free-standing triboelectric layer mode, vertical contact separation mode³²⁵. MXene is beneficial for triboelectric nanogenerators because it increases the electronegativity, dielectric constant, and electrical conductivity of the electrode. Wang et al. demonstrated a polyaniline/V₂C composite film via in-situ polymerization used in a self-powered NH₃ detection device based on electromagnetic and triboelectric nanogenerator³²⁶. This hybrid nanogenerator, enabled by walking and running, is used to charge the supercapacitor for operating an NH₃ sensor. The real-time application of the device using polyaniline/V₂C as anode was assessed by powering the alarm circuit via monitoring the NH₃ concentration while used in the shoes of coal mine workers and chicken farms [Fig. 12(f)].

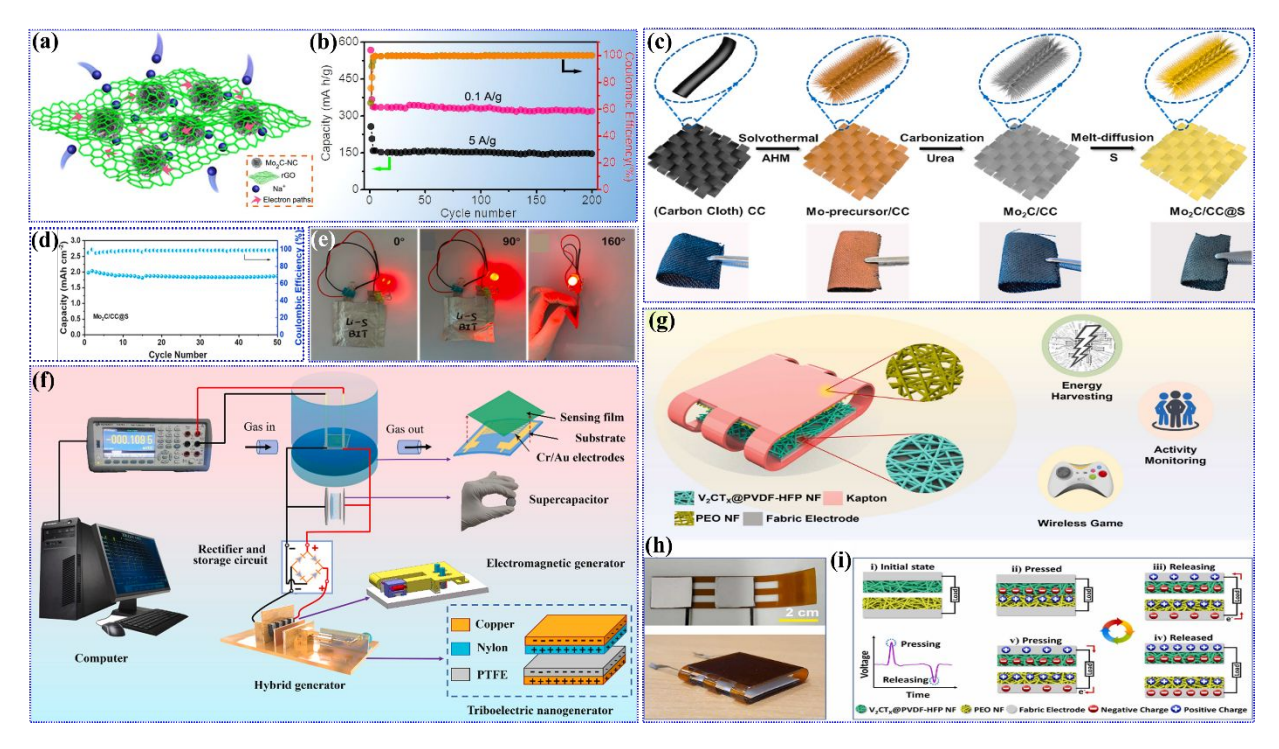


Fig. 12. (a) 3D rGO wrapped N-doped carbon spheres/Mo₂C nanoparticles, (b) cyclic stability study of 3D Mo₂C based SIB, (c) synthesis of flexible self-supported Mo₂C/CC@S as cathode for LSB, (d) cyclic study of Mo₂C/CC@S pouch cell, (e) practical application of the flexible LSB pouch cell, (f) polyaniline/V₂C based gas sensor for self-powered NH₃ sensing, (g) V₂CT_x/PVDF-HFP nanofibers triboelectric nanogenerator device and smart applications, (h) V₂CT_x/PVDF-HFP based triboelectric device, and (i) working mechanism of this triboelectric device. (a, b) Reproduced from ref³¹² with permission from Elsevier, copyright 2021, (c-e) reproduced from ref³¹⁴ with permission from Elsevier, copyright 2021, (g-i) reproduced from ref³²⁷ with permission from Elsevier, copyright 2024.

In another investigation, a triboelectric self-powered sensor was fabricated using Mo₂CT_x/polydimethylsiloxane film³²⁸. This Mo-MXene-based pressure sensor enhanced the system's sensitivity, stability, and quick recovery to achieve non-contact sensing. In a recent study by Faruk et al., a composite nanofiber of V₂CT_x/poly(vinylidene-fluoride-co-hexafluoropropylene) (PVDF-HFP) was synthesized via a simple electrospinning method as a self-powered pressure sensor³²⁷. The introduction of V₂CT_x into the polymer matrix enhanced the dielectric constant as well as the capturing ability of the system, resulting in a high sensitivity of 25.17 V kPa⁻¹ with large power density and stability. The fabricated smart belt using a V-MXene-based triboelectric nanogenerator was used as a self-powered motion sensor for sensing real-time human posture and activity like running, walking, jumping, and cycling

[Fig. 12(g-i)]. Yang et al. demonstrated a flexible triboelectric nanogenerator using a hybrid film of Nb₂CT_x/CNT/PEDOT with high output³²⁹. This self-powered wearable sensor achieved a short-circuit current of 4.42 μA and an open circuit voltage of 184.1 V with excellent sensitivity and stability. Fig. 13(a) shows the real-time application of this sensor for monitoring human motions like making a fist, bending the wrist, swallowing, sliding the mouse, or typing on the keyboard. Further, the large-scale production of energy harvesting flexible electronic devices can be achieved by the incorporation of various organic and inorganic fillers in non-Ti MXene materials which may lead to numerous possibilities in transducers, actuators, energy storage devices, and wearable sensors.

7.3 Wearable health monitoring

Different physiological signals created in the human body, like electrocardiogram, blood pressure, muscle movements, body temperature, heart rate, pulse rate, and so on, can be monitored by wearable electronic devices (e-skins) by fixing the sensor over the human skin. Wearable e-skins prepared by MXene materials have also been utilized for healthcare applications³²⁵. Richard et al. reported a wearable sensing band-aid [Fig. 13(b, c)] for real-time regulation of sleep hormones utilizing Nb₂CT_x combined with a metal-organic framework (MOF)³³⁰. The incorporation of Nb-MXene with Zn-based bio-MOF led to an increment in conductivity, catalytic activity, and abundant active centers which make them efficient for electrochemical detection of melatonin sleep hormone within a wide detection range from 1 to $100 \,\mu$ M at a detection limit of 215 nM [Fig. 13(d, e)]. The real-time application of this sensing transducer patch in a medical context was also established by detecting melatonin hormone in different biological fluids like blood serum, sweat, and cerebrospinal fluid.

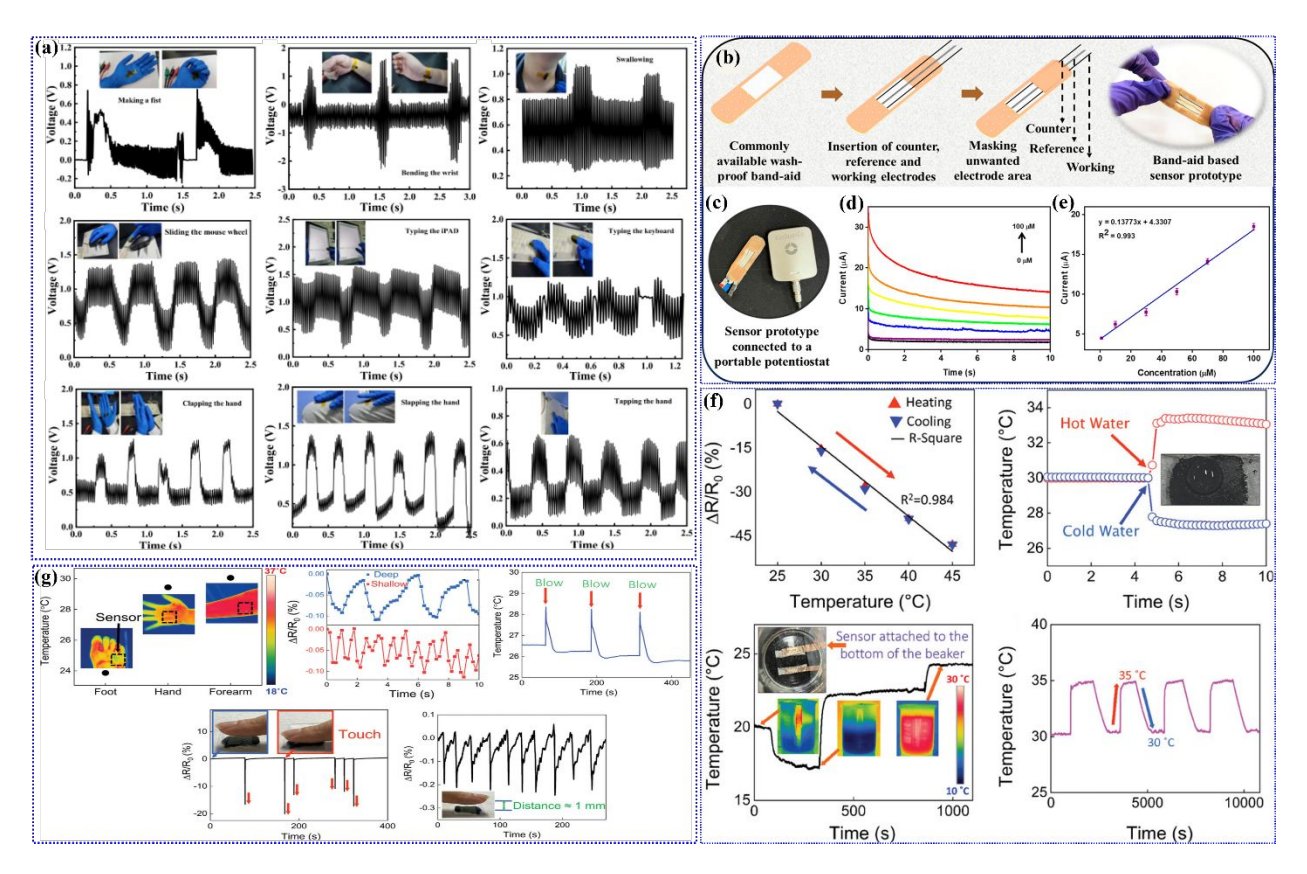


Fig. 13. (a) Human motion monitoring by the flexible Nb₂CT_x/CNT/PEDOT-based triboelectric sensor, (b) assembling band-aid-like prototype, (c) fabricated prototype sensor connected to a potentiostat, (d) current response within detection range from 1 to 100 μM, (e) calibration plot, (f) practical sensing application of the Ir-V₂CT_x heterostructure-based sensor, (g) real-time skin temperature, breathing, blowing, touching, and proximity detection by Ru-V₂CT_x-based sensor. (a) Reproduced from ref³²⁹ with permission from Elsevier, copyright 2022, (b-e) reproduced from ref³³⁰ with permission from American Chemical Society, copyright 2024, (f) reproduced from ref³³¹ with permission from Wiley-VCH, copyright 2024, (g) reproduced from ref³³² with permission from Wiley-VCH, copyright 2023.

The first report on thermography of human-machine interaction for real-time practical sensing in healthcare applications was done by Mahapatra et al. utilizing iridium-incorporated V_2CT_x synthesized via atomic layer deposition³³¹. This unique heterostructure of Irincorporated V-MXene exhibited enhanced temperature sensing performance during repeated cooling and heating water-dropping tests with excellent durability [Fig. 13(f)]. Another work by the same group reported that ruthenium-incorporated delaminated V-MXene was used for temperature sensing³³². This sensor has efficient sensing performance compared to pristine V-MXene and can be useful for safe, personal healthcare monitoring, including touch, breathing, skin temperature, proximity, and blowing [Fig. 13(g)].

8. Conclusion and outlook

After the discovery of MXene as a flourishing 2D material, immense research has been concentrated on Ti-based MXenes. Interestingly, the advantage of the utilization of underexplored non-Ti-MXenes demonstrated admiring characteristics compared to the typical Ti-MXenes. This review article summarizes the state-of-art research progress on non-Ti-MXenes and their doped/substituted or surface functionalized versions, followed by their flexibility and recent utilization in wearable and portable electronic devices. For example, Mo, V, Nb, and Y-MXenes exhibited excellent electronic conductivity which was admirable for energy applications. On the other hand, V, Ta, and Nb-MXenes were associated with low toxicity and biocompatibility leading to their application in the biomedical field. Also, V₂C and Nb₂C demonstrated higher theoretical capacity than Ti₂C. Among various non-Ti-MXenes, V, Mo, and Nb-based MXenes have been most successfully explored experimentally along with Cr, Ta, Hf, Sc, Y, W, and Zr-based MXenes investigated mainly through theoretical simulations. For further tuning of physicochemical properties of non-Ti-based MXenes, structural engineering via doping or functionalization portrayed a great opportunity for energy applications. Effective methods like spinning, coating, vacuum filtration, and printing have been used to obtain flexible and lightweight non-Ti MXene devices for wearable and portable electronics. Although non-Ti-MXenes in wearable and portable electronics have been getting much interest recently, several factors need to be resolved for further research advancement on this topic. The specific limitations and future aspects of this research field [Fig. 14] are listed below.

Experimental synthesis: Most of the non-Ti-MXenes are not experimentally prepared; they have been theoretically predicted. Facile experimental strategies need to be explored to synthesize non-Ti-MXenes and reveal their properties and applications. Also, bulk synthesis of air-stable non-Ti-MXenes without an oxidation tendency is required for their practical application.

Green synthesis method: The conventional HF-etching method is mainly used to synthesize non-Ti-MXenes, and sometimes incomplete etching and bi-product impurities resulted. Thus, alternative synthesis strategies like hydrothermal, microwave, CVD, and electrochemical need to be explored for successful etching.

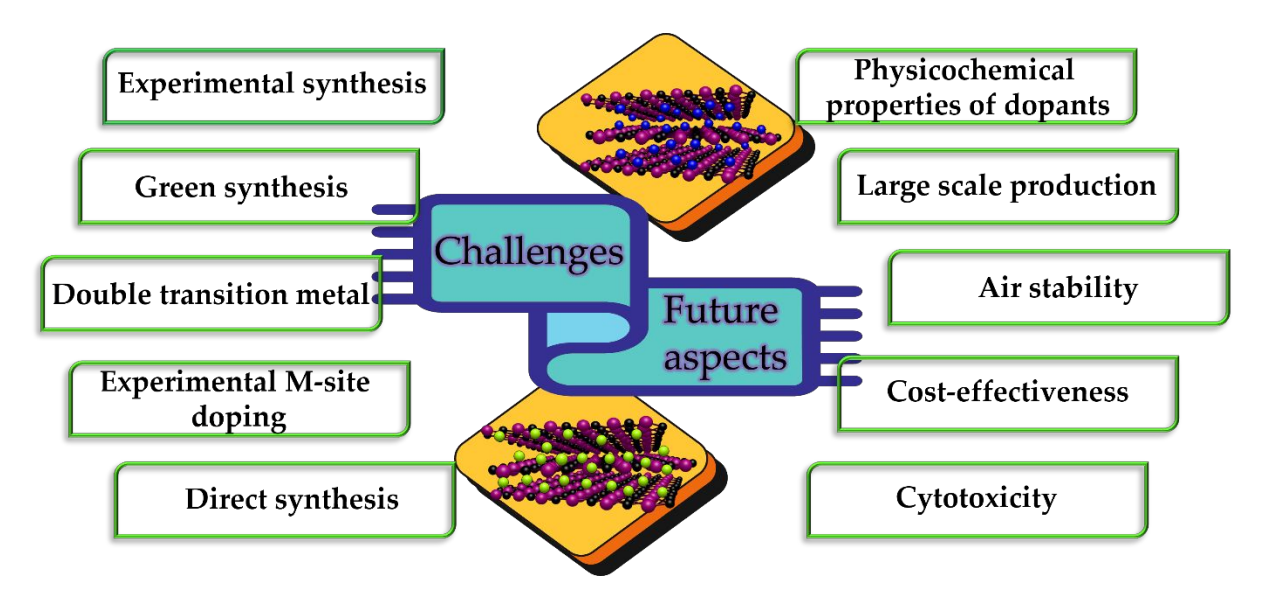


Fig. 14. Overview of challenges and future aspects of this research field.

Direct synthesis: Non-Ti MXene synthesis deeply involves the synthesis of MAX phases (top-down approach). However, bottom-up synthesis methods like chemical vapor deposition, solid-state reaction, magnetron sputtering, and epitaxial synthesis are also needed to explore more for synthesizing non-Ti MXenes with controlled surface functionalities for advanced applications.

Double transition metal or multiple metal-based non-Ti MXene: There are very few experimental works performed on double transition metal or multi-metal (trimetallic) incorporated non-Ti MXenes. Particular attention should be centered on developing facile synthesis methods for their successful formation and their high purity.

Distinction of doped and substituted non-Ti MXenes: Still, there is confusion about the notion of doped and substituted MXenes. MXenes should be considered doped when the dopant concentration is very low, like in the ppm level, and when the heteroatom concentration is high, they should be considered substituted MXenes. A more specific distinction is required to understand their properties, mechanisms, and suitable applications.

Experimental methods for M-site doping: Mostly, theoretical simulations have been carried out for doping or substitution in the M-site using transition metals. Suitable experimental procedures are needed with high yield and quality to verify their actual properties and applications.

Physicochemical properties: The relation between structure and properties like bonding nature among dopants, surface functionalities, and MXene precursors, as well as the content of doping of non-Ti-MXenes, still needed to be addressed.

Fabrication techniques for flexible freestanding non-Ti MXene: Considering layer restacking, and viscosity more suitable technologies need to be carefully studied for the fabrication of flexible freestanding MXene electrodes.

Other potential applications except common energy storage devices: The use of flexible non-Ti-MXenes in wearable electronics is still in the initial stage and is mainly studied for supercapacitors and batteries. It is still necessary to investigate other potential applications, such as energy harvesting and electronic sensors, according to the advancements made in theoretical and technical techniques utilizing cutting-edge non-Ti MXene-based composite materials for wearable electronics. Their biocompatibility and toxicity need to be systematically studied for long-term integration in wearable human skin for sensing.

Non-Ti-MXene derived materials: An interesting study can be performed by creating heterojunctions and interfaces between non-Ti-MXenes and other suitable materials like carbonaceous materials, metal chalcogenides, hollow spheres, and 2D or 3D architectures. Overall, continuous investigation of non-Ti-MXene and their modified versions can pave the way for future advancements in flexible and wearable electronics.

Declaration of Competing Interest

The authors have no known conflicts of interest to declare.

Acknowledgment

This work was supported by DOE BES-RENEW award number DE-SC0024611.

References

- 1. M. A. Butt, N. L. Kazanskiy and S. N. Khonina, *Electronics*, 2022, **11**, 716.
- 2. B. Dai, C. Gao and Y. Xie, *View*, 2022, **3**, 20220027.
- 3. N. Lu and D.-H. Kim, Soft Robotics, 2014, 1, 53-62.
- 4. Y. Yin, C. Guo, H. Li, H. Yang, F. Xiong and D. Chen, Sensors, 2022, 22, 5089.
- 5. R. Yin, D. Wang, S. Zhao, Z. Lou and G. Shen, *Advanced Functional Materials*, 2021, **31**, 2008936.
- 6. Y. Luo, W. Que, Y. Tang, Y. Kang, X. Bin, Z. Wu, B. Yuliarto, B. Gao, J. Henzie and Y. Yamauchi, *ACS nano*, 2024, **18**, 11675-11687.
- 7. S. M. Youssry, M. N. El-Nahass, R. Kumar, I. El-Hallag, W. K. Tan and A. Matsuda, *Journal of Energy Storage*, 2020, **30**, 101485.
- 8. S. M. Youssry, I. El-Hallag, R. Kumar, G. Kawamura, A. Matsuda and M. N. El-Nahass, *Journal of Electroanalytical Chemistry*, 2020, **857**, 113728.
- 9. R. Kumar, S. Sahoo, E. Joanni, R. K. Singh, W. K. Tan, K. K. Kar and A. Matsuda, *Progress in Energy Combustion Science*, 2019, **75**, 100786.
- 10. R. Kumar, S. Sahoo, E. Joanni, R. K. Singh, K. Maegawa, W. K. Tan, G. Kawamura, K. K. Kar and A. Matsuda, *Materials Today*, 2020, **39**, 47-65.
- 11. S. Kalia, R. Kumar, R. Dhiman and R. K. Singh, *Journal of Energy Storage*, 2024, **83**, 110650.

- 12. R. Kumar, R. K. Singh, P. K. Dubey, D. P. Singh, R. M. Yadav and R. S. Tiwari, *RSC Advances*, 2015, **5**, 7112-7120.
- 13. R. Kumar, S. Sahoo, E. Joanni, R. K. Singh and K. K. Kar, *ACS Applied Materials Interfaces*, 2021, **14**, 20306-20325.
- 14. S. M. Youssry, I. El-Hallag, R. Kumar, G. Kawamura, W. K. Tan, A. Matsuda and M. N. El-Nahass, *Journal of Energy Storage*, 2022, **50**, 104638.
- 15. R. Kumar, R. K. Singh, A. R. Vaz and S. A. Moshkalev, *RSC Advances*, 2015, **5**, 67988-67995.
- 16. R. Kumar, S. M. Youssry, E. Joanni, S. Sahoo, G. Kawamura and A. Matsuda, *Journal of Energy Storage*, 2022, **56**, 105896.
- 17. S. Sharma, R. Kumar and R. M. Yadav, *Materials Today Communications*, 2023, **36**, 106860.
- 18. S. Sharma, S. S. Mishra, R. Kumar and R. M. Yadav, *New Journal of Chemistry*, 2022, **46**, 18613-18646.
- 19. S. Li, Y. Zhang, Y. Wang, K. Xia, Z. Yin, H. Wang, M. Zhang, X. Liang, H. Lu and M. Zhu, *InfoMat*, 2020, **2**, 184-211.
- 20. A. Ahmed, M. A. Jalil, M. M. Hossain, M. Moniruzzaman, B. Adak, M. T. Islam, M. S. Parvez and S. Mukhopadhyay, *Journal of Materials Chemistry C*, 2020, **8**, 16204-16215.
- 21. J. Li, M. Xin, Z. Ma, Y. Shi and L. Pan, *Nanotechnology*, 2021, **32**, 472002.
- 22. W. Hu, H. Zhang, K. Salaita and H. Sirringhaus, SmartMat, 2020, 1.
- 23. X. Peng, L. Peng, C. Wu and Y. Xie, *Chemical Society Reviews*, 2014, **43**, 3303-3323.
- 24. C. Zhang, Y. Ma, X. Zhang, S. Abdolhosseinzadeh, H. Sheng, W. Lan, A. Pakdel, J. Heier and F. Nüesch, *Energy Environmental Materials*, 2020, **3**, 29-55.
- 25. M. Naguib, M. Kurtoglu, V. Presser, J. Lu, J. Niu, M. Heon, L. Hultman, Y. Gogotsi and M. W. Barsoum, in *MXenes*, Jenny Stanford Publishing, 2011, pp. 15-29.
- 26. S. De, S. Roy and G. C. Nayak, *Materials Today Nano*, 2023, **22**, 100337.
- 27. X.-H. Zha, P. Xu, Q. Huang, S. Du and R.-Q. Zhang, *Nanoscale Advances*, 2020, **2**, 347-355.
- 28. V. Kamysbayev, A. S. Filatov, H. Hu, X. Rui, F. Lagunas, D. Wang, R. F. Klie and D. V. Talapin, *Science*, 2020, **369**, 979-983.
- 29. Z. K. Baghini, A. Mostafaei and M. Abbasnejad, *Journal of Alloys Compounds*, 2022, **922**, 166198.
- 30. J. He, P. Lyu and P. Nachtigall, Journal of Materials Chemistry C, 2016, 4, 11143-11149.
- 31. J. Abbott, V. Morris, M. Adhikari, S. Balabhadra, A. Bretana, B. Rai, D. Autrey and B. Gautam, *Microscopy Microanalysis*, 2024, **30**.
- 32. Y. Gogotsi and B. Anasori, *ACS Nano*, 2019, **13**, 8491-8494.
- 33. M. Downes, C. E. Shuck, R. J. Wang, P. P. Michałowski, J. Shochat, D. Zhang, M. Shekhirev, Y. Yang, N. J. Zaluzec and R. Arenal, *Journal of the American Chemical Society*, 2024.
- 34. M. Alhabeb, K. Maleski, B. Anasori, P. Lelyukh, L. Clark, S. Sin and Y. Gogotsi, *Chemistry of Materials*, 2017, **29**, 7633-7644.
- 35. J. Jeon, Y. Park, S. Choi, J. Lee, S. S. Lim, B. H. Lee, Y. J. Song, J. H. Cho, Y. H. Jang and S. Lee, *ACS nano*, 2018, **12**, 338-346.
- 36. M. Mozafari and M. Soroush, *Materials Advances*, 2021, **2**, 7277-7307.
- 37. S. M. M. Alonzo, R. Dahal, M. D. Ashie and B. P. Bastakoti, *Journal*, 2024.
- 38. M. Naguib, M. W. Barsoum and Y. Gogotsi, *Advanced Materials*, 2021, **33**, 2103393.
- 39. I. Ihsanullah, *Nano-Micro Letters*, 2020, **12**, 1-20.
- 40. A. Lipatov, H. Lu, M. Alhabeb, B. Anasori, A. Gruverman, Y. Gogotsi and A. Sinitskii, *Science advances*, 2018, **4**, eaat0491.
- 41. Y. Liu, W. Zou, N. Zhao and J. Xu, Nature Communications, 2023, 14, 5342.
- 42. T. P. Nguyen, D. M. T. Nguyen, H. K. Le, D.-V. N. Vo, S. S. Lam, R. S. Varma, M. Shokouhimehr, C. C. Nguyen and Q. Van Le, *Molecular Catalysis*, 2020, **486**, 110850.
- 43. M. Jeon, B.-M. Jun, S. Kim, M. Jang, C. M. Park, S. A. Snyder and Y. Yoon, *Chemosphere*, 2020, **261**, 127781.

- 44. L. Damptey, B. N. Jaato, C. S. Ribeiro, S. Varagnolo, N. P. Power, V. Selvaraj, D. Dodoo-Arhin, R. V. Kumar, S. P. Sreenilayam and D. Brabazon, *Global Challenges*, 2022, **6**, 2100120.
- 45. S. De, S. Acharya, S. Sahoo and G. C. Nayak, *Materials Chemistry Frontiers*, 2021, **5**, 7134-7169.
- 46. S. De, S. Acharya, S. Sahoo, J.-J. Shim and G. C. Nayak, *Materials Chemistry Frontiers*, 2022, **6**, 818-842.
- 47. S. De, C. K. Maity, S. Sahoo and G. C. Nayak, ACS Applied Energy Materials, 2021, 4, 3712-3723.
- 48. J. Wu, Z. Wang, S. Zhang, Q. Yang, Z. Li, X. Zang, X. Zhao, N. Shang, N. Khaorapapong, X. Xu and Y. Yamauchi, *Small*, 2024, **20**, 2305730.
- 49. X. Xia, J. Yang, Y. Liu, J. Zhang, J. Shang, B. Liu, S. Li and W. Li, *Advanced Science*, 2023, **10**, 2204875.
- 50. D. Xiong, Y. Shi and H. Y. Yang, *Materials Today*, 2021, **46**, 183-211.
- 51. T. Xu, H. Du, H. Liu, W. Liu, X. Zhang, C. Si, P. Liu and K. Zhang, *Advanced materials*, 2021, **33**, 2101368.
- 52. S. De, S. Acharya, C. K. Maity and G. C. Nayak, *ACS Applied Nano Materials*, 2023, **6**, 11175-11186.
- 53. S. Fatima, M. W. Hakim, D. Akinwande and S. Rizwan, *Materials Today Physics*, 2022, **26**, 100730.
- 54. S. P. Sreenilayam, I. U. Ahad, V. Nicolosi and D. Brabazon, *Materials Today*, 2021, **43**, 99-131.
- 55. X. Zhao, L.-Y. Wang, C.-Y. Tang, X.-J. Zha, Y. Liu, B.-H. Su, K. Ke, R.-Y. Bao, M.-B. Yang and W. Yang, *ACS nano*, 2020, **14**, 8793-8805.
- 56. M. O. Faruk, A. Ahmed, B. Adak, M. Marzana, M. M. Hossain and S. Mukhopadhyay, *Journal of Materials Chemistry C*, 2021, **9**, 10193-10215.
- 57. S. Seyedin, S. Uzun, A. Levitt, B. Anasori, G. Dion, Y. Gogotsi and J. M. Razal, *Advanced Functional Materials*, 2020, **30**, 1910504.
- 58. X. Liu, X. Jin, L. Li, J. Wang, Y. Yang, Y. Cao and W. Wang, *Journal of Materials Chemistry A*, 2020, **8**, 12526-12537.
- 59. F. Song, G. Li, Y. Zhu, Z. Wu, X. Xie and N. Zhang, *Journal of Materials Chemistry A*, 2020, **8**, 18538-18559.
- 60. D. Wen, X. Wang, L. Liu, C. Hu, C. Sun, Y. Wu, Y. Zhao, J. Zhang, X. Liu and G. Ying, *ACS Applied Materials Interfaces*, 2021, **13**, 17766-17780.
- 61. M. M. Hasan, M. M. Hossain and H. K. Chowdhury, *Journal of Materials Chemistry A*, 2021, **9**, 3231-3269.
- 62. L. Gao, C. Li, W. Huang, S. Mei, H. Lin, Q. Ou, Y. Zhang, J. Guo, F. Zhang and S. Xu, *Chemistry of Materials*, 2020, **32**, 1703-1747.
- 63. C. J. Zhang, S. Pinilla, N. McEvoy, C. P. Cullen, B. Anasori, E. Long, S.-H. Park, A. Seral-Ascaso, A. Shmeliov and D. Krishnan, *Chemistry of Materials*, 2017, **29**, 4848-4856.
- 64. Z. Wu, T. Shang, Y. Deng, Y. Tao and Q. H. Yang, *Advanced science*, 2020, **7**, 1903077.
- 65. A. Szuplewska, D. Kulpińska, M. Jakubczak, A. Dybko, M. Chudy, A. Olszyna, Z. Brzózka and A. M. Jastrzębska, *Advanced Drug Delivery Reviews*, 2022, **182**, 114099.
- 66. S. Zhang, H. Ying, P. Huang, J. Wang, Z. Zhang, Z. Zhang and W.-Q. Han, *ACS Applied Energy Materials*, 2021, **4**, 9806-9815.
- 67. W. Bao, L. Liu, C. Wang, S. Choi, D. Wang and G. Wang, *Advanced Energy Materials*, 2018, **8**, 1702485.
- 68. Y. Wen, T. E. Rufford, X. Chen, N. Li, M. Lyu, L. Dai and L. Wang, *Nano energy*, 2017, **38**, 368-376.
- 69. C. Lu, L. Yang, B. Yan, L. Sun, P. Zhang, W. Zhang and Z. Sun, *Advanced Functional Materials*, 2020, **30**, 2000852.
- 70. H. Larijani and M. Khorshidian, *Applied Surface Science*, 2019, **492**, 826-842.
- 71. P. Chakraborty, T. Das, D. Nafday, L. Boeri and T. Saha-Dasgupta, *Physical Review B*, 2017, **95**, 184106.

- 72. W. Bao, R. Wang, C. Qian, Z. Zhang, R. Wu, Y. Zhang, F. Liu, J. Li and G. Wang, *ACS nano*, 2021, **15**, 16207-16217.
- 73. J. Ran, G. Gao, F.-T. Li, T.-Y. Ma, A. Du and S.-Z. Qiao, *Nature communications*, 2017, **8**, 13907.
- 74. H. Wang, Y. Wu, T. Xiao, X. Yuan, G. Zeng, W. Tu, S. Wu, H. Y. Lee, Y. Z. Tan and J. W. Chew, *Applied Catalysis B: Environmental*, 2018, **233**, 213-225.
- 75. A. D. Dillon, M. J. Ghidiu, A. L. Krick, J. Griggs, S. J. May, Y. Gogotsi, M. W. Barsoum and A. T. Fafarman, *Advanced Functional Materials*, 2016, **26**, 4162-4168.
- 76. Y. An, Y. Tian, C. Liu, S. Xiong, J. Feng and Y. Qian, *ACS nano*, 2021, **15**, 15259-15273.
- 77. X. Han, L. An, Y. Hu, Y. Li, C. Hou, H. Wang and Q. Zhang, *Applied Catalysis B: Environmental*, 2020, **265**, 118539.
- 78. W. Huang, L. Hu, Y. Tang, Z. Xie and H. Zhang, *Advanced Functional Materials*, 2020, **30**, 2005223.
- 79. A. C. Rajan, A. Mishra, S. Satsangi, R. Vaish, H. Mizuseki, K.-R. Lee and A. K. Singh, *Chemistry of Materials*, 2018, **30**, 4031-4038.
- 80. J. Chen, M. Liu, H. Huang, F. Deng, L. Mao, Y. Wen, L. Huang, J. Tian, X. Zhang and Y. Wei, *Journal of Molecular Liquids*, 2018, **259**, 179-185.
- 81. M. Liu, G. Zeng, K. Wang, Q. Wan, L. Tao, X. Zhang and Y. Wei, *Nanoscale*, 2016, **8**, 16819-16840.
- 82. L. Qin, Q. Tao, X. Liu, M. Fahlman, J. Halim, P. O. Å. Persson, J. Rosen and F. Zhang, *Nano Energy*, 2019, **60**, 734-742.
- 83. J. Chen, Q. Huang, H. Huang, L. Mao, M. Liu, X. Zhang and Y. Wei, *Nanoscale*, 2020, **12**, 3574-3592.
- 84. H. Wang, J. Zhang, Y. Wu, H. Huang, G. Li, X. Zhang and Z. Wang, *Applied Surface Science*, 2016, **384**, 287-293.
- 85. X. Zhu, B. Liu, H. Hou, Z. Huang, K. M. Zeinu, L. Huang, X. Yuan, D. Guo, J. Hu and J. Yang, *Electrochimica Acta*, 2017, **248**, 46-57.
- 86. Y. Tian, W. Que, Y. Luo, C. Yang, X. Yin and L. B. Kong, *Journal of Materials Chemistry A*, 2019, **7**, 5416-5425.
- 87. P. Liu, W. Ding, J. Liu, L. Shen, F. Jiang, P. Liu, Z. Zhu, G. Zhang, C. Liu and J. Xu, *Journal of Alloys and Compounds*, 2020, **829**, 154634.
- 88. H. Lin, X. Wang, L. Yu, Y. Chen and J. Shi, *Nano Letters*, 2017, **17**, 384-391.
- 89. Z. Li, Z. Zhuang, F. Lv, H. Zhu, L. Zhou, M. Luo, J. Zhu, Z. Lang, S. Feng, W. Chen, L. Mai and S. Guo, *Advanced Materials*, 2018, **30**, 1803220.
- 90. Y. Xia, T. S. Mathis, M.-Q. Zhao, B. Anasori, A. Dang, Z. Zhou, H. Cho, Y. Gogotsi and S. Yang, *Nature*, 2018, **557**, 409-412.
- 91. Z. Huang, S. Wang, S. Kota, Q. Pan, M. W. Barsoum and C. Y. Li, *Polymer*, 2016, **102**, 119-126.
- 92. W. Shao, M. Tebyetekerwa, I. Marriam, W. Li, Y. Wu, S. Peng, S. Ramakrishna, S. Yang and M. Zhu, *Journal of Power Sources*, 2018, **396**, 683-690.
- 93. C. Lamiel, I. Hussain, J. H. Warner and K. Zhang, *Materials Today*, 2023, **63**, 313-338.
- 94. M. W. Barsoum, *MAX phases: properties of machinable ternary carbides and nitrides*, John Wiley & Sons, 2013.
- 95. V. H. Nowotny, *Progress in Solid State Chemistry*, 1971, **5**, 27-70.
- 96. Y. Wang, T. Guo, Z. Tian, K. Bibi, Y. Z. Zhang and H. N. Alshareef, *Advanced Materials*, 2022, **34**, 2108560.
- 97. M. Hadi, *Journal of Physics Chemistry of Solids*, 2020, **138**, 109275.
- 98. X.-H. Zha, J. Zhou, P. Eklund, X. Bai, S. Du and Q. Huang, *2D Metal Carbides Nitrides Structure, Properties Applications*, 2019, 53-68.
- 99. J.-P. Palmquist, S. Li, P. Å. Persson, J. Emmerlich, O. Wilhelmsson, H. Högberg, M. Katsnelson, B. Johansson, R. Ahuja and O. Eriksson, *Physical Review B—Condensed Matter Materials Physics*, 2004, **70**, 165401.

- 100. J. Rosen, M. Dahlqvist, Q. Tao, L. J. D. M. C. Hultman, P. Nitrides Structure and Applications, 2D Metal Carbides Nitrides Structure, Properties Applications, 2019, 37-52.
- 101. M. Dahlqvist, J. Lu, R. Meshkian, Q. Tao, L. Hultman and J. Rosen, *Science advances*, 2017, **3**, e1700642.
- 102. B. Anasori, Y. Xie, M. Beidaghi, J. Lu, B. C. Hosler, L. Hultman, P. R. Kent, Y. Gogotsi and M. W. Barsoum, *ACS nano*, 2015, **9**, 9507-9516.
- 103. M. Sokol, V. Natu, S. Kota and M. W. Barsoum, Trends in Chemistry, 2019, 1, 210-223.
- 104. R. Sakthivel, M. Keerthi, R.-J. Chung and J.-H. J. P. i. M. S. He, *Progress in Materials Science*, 2023, **132**, 101024.
- 105. A. Iqbal, J. Hong, T. Y. Ko and C. M. Koo, *Nano Convergence*, 2021, **8**, 9.
- 106. P. Das and Z.-S. Wu, *Journal of Physics: Energy*, 2020, **2**, 032004.
- 107. W. Feng, R. Wang, Y. Zhou, L. Ding, X. Gao, B. Zhou, P. Hu and Y. Chen, *Advanced Functional Materials*, 2019, **29**, 1901942.
- 108. X. Guo, C. Wang, W. Wang, Q. Zhou, W. Xu, P. Zhang, S. Wei, Y. Cao, K. Zhu and Z. Liu, *Nano Res. Energy*, 2022, **1**, e9120026.
- 109. Y. Tang, C. Yang, Y. Xie, Y. Kang, W. Que, J. Henzie and Y. Yamauchi, *ACS Sustainable Chemistry Engineering*, 2022, **11**, 168-176.
- 110. D. Vryhof, *Drexel Univ*, 2013, 36.
- 111. C. Hu, C. Li, J. Halim, S. Kota, D. J. Tallman and M. W. Barsoum, *Journal of the American Ceramic Society*, 2015, **98**, 2713-2715.
- 112. R. Meshkian, L.-Å. Näslund, J. Halim, J. Lu, M. W. Barsoum and J. Rosen, *Scripta Materialia*, 2015, **108**, 147-150.
- 113. J. Halim, S. Kota, M. R. Lukatskaya, M. Naguib, M. Q. Zhao, E. J. Moon, J. Pitock, J. Nanda, S. J. May and Y. Gogotsi, *Advanced Functional Materials*, 2016, **26**, 3118-3127.
- 114. M. Ade and H. Hillebrecht, *Inorganic chemistry*, 2015, **54**, 6122-6135.
- 115. W. Xiong, X. Feng, Y. Xiao, T. Huang, X. Li, Z. Huang, S. Ye, Y. Li, X. Ren and X. Wang, *Chemical Engineering Journal*, 2022, **446**, 137466.
- 116. H. Zhou, Z. Chen, E. Kountoupi, A. Tsoukalou, P. M. Abdala, P. Florian, A. Fedorov and C. R. Müller, *Nature Communications*, 2021, **12**, 5510.
- 117. Z. W. Seh, K. D. Fredrickson, B. Anasori, J. Kibsgaard, A. L. Strickler, M. R. Lukatskaya, Y. Gogotsi, T. F. Jaramillo and A. Vojvodic, *ACS Energy Letters*, 2016, **1**, 589-594.
- 118. X. Zhao, W. Sun, D. Geng, W. Fu, J. Dan, Y. Xie, P. R. Kent, W. Zhou, S. J. Pennycook and K. P. Loh, *Advanced Materials*, 2019, **31**, 1808343.
- 119. D. A. Kuznetsov, Z. Chen, P. V. Kumar, A. Tsoukalou, A. Kierzkowska, P. M. Abdala, O. V. Safonova, A. Fedorov and C. R. Müller, *Journal of the American Chemical Society*, 2019, **141**, 17809-17816.
- 120. D. A. Kuznetsov, Z. Chen, P. M. Abdala, O. V. Safonova, A. Fedorov and C. R. Muller, *Journal of the American Chemical Society*, 2021, **143**, 5771-5778.
- 121. A. VahidMohammadi, W. Liang, M. Mojtabavi, M. Wanunu and M. Beidaghi, *Energy Storage Materials*, 2021, **41**, 554-562.
- 122. H. Hu, H. Huang, L. Xia, X. Qian, W. Feng, Y. Chen and Y. Li, *Chemical Engineering Journal*, 2022, **440**, 135810.
- 123. L. Wang, L. Yuan, K. Chen, Y. Zhang, Q. Deng, S. Du, Q. Huang, L. Zheng, J. Zhang and Z. Chai, *ACS applied materials interfaces*, 2016, **8**, 16396-16403.
- 124. Y. Yoon, A. P. Tiwari, M. Choi, T. G. Novak, W. Song, H. Chang, T. Zyung, S. S. Lee, S. Jeon and K. S. An, *Advanced Functional Materials*, 2019, **29**, 1903443.
- 125. G. Deysher, C. E. Shuck, K. Hantanasirisakul, N. C. Frey, A. C. Foucher, K. Maleski, A. Sarycheva, V. B. Shenoy, E. A. Stach and B. Anasori, *ACS Nano*, 2019, **14**, 204-217.
- 126. J. Geng, R. Wu, H. Bai, I.-N. Chan, K. W. Ng, W. F. Ip and H. Pan, *International Journal of Hydrogen Energy*, 2022, **47**, 18725-18737.
- 127. W. Sun, Y. Xie and P. R. Kent, *Nanoscale*, 2018, **10**, 11962-11968.

- 128. A. VahidMohammadi, A. Hadjikhani, S. Shahbazmohamadi and M. Beidaghi, *ACS nano*, 2017, **11**, 11135-11144.
- 129. W. Feng, X. Han, H. Hu, M. Chang, L. Ding, H. Xiang, Y. Chen and Y. Li, *Nature Communications*, 2021, **12**, 2203.
- 130. R. Thakur, A. VahidMohammadi, J. Smith, M. Hoffman, J. Moncada, M. Beidaghi and C. A. Carrero, *ACS Catalysis*, 2020, **10**, 5124-5134.
- 131. R. Venkatkarthick, N. Rodthongkum, X. Zhang, S. Wang, P. Pattananuwat, Y. Zhao, R. Liu and J. Qin, *ACS Applied Energy Materials*, 2020, **3**, 4677-4689.
- 132. Y. Guan, S. Jiang, Y. Cong, J. Wang, Z. Dong, Q. Zhang, G. Yuan, Y. Li and X. Li, *2D Materials*, 2020, **7**, 025010.
- 133. K. Matthews, T. Zhang, C. E. Shuck, A. VahidMohammadi and Y. Gogotsi, *Chemistry of Materials*, 2021, **34**, 499-509.
- 134. S. Park, Y.-L. Lee, Y. Yoon, S. Y. Park, S. Yim, W. Song, S. Myung, K.-S. Lee, H. Chang and S. S. Lee, *Applied Catalysis B: Environmental*, 2022, **304**, 120989.
- 135. C. Wang, S. Chen, H. Xie, S. Wei, C. Wu and L. Song, *Advanced Energy Materials*, 2019, **9**, 1802977.
- 136. S. Zada, W. Dai, Z. Kai, H. Lu, X. Meng, Y. Zhang, Y. Cheng, F. Yan, P. Fu and X. Zhang, *Angewandte Chemie International Edition*, 2020, **59**, 6601-6606.
- 137. M. Naguib, J. Halim, J. Lu, K. M. Cook, L. Hultman, Y. Gogotsi and M. W. Barsoum, *Journal of the American Chemical Society*, 2013, **135**, 15966-15969.
- 138. L. Gao, C. Ma, S. Wei, A. V. Kuklin, H. Zhang and H. Ågren, *ACS nano*, 2021, **15**, 954-965.
- 139. H. Lin, S. Gao, C. Dai, Y. Chen and J. Shi, *Journal of the American Chemical Society*, 2017, **139**, 16235-16247.
- 140. Y. Wang, Y. Wang, K. Chen, K. Qi, T. Xue, H. Zhang, J. He and S. Xiao, *ACS Nano*, 2020, **14**, 10492-10502.
- 141. M. Song, S.-Y. Pang, F. Guo, M.-C. Wong and J. Hao, *Advanced Science*, 2020, **7**, 2001546.
- 142. K.-Y. Sun, Y. Wu, J. Xu, W. Xiong, W. Xu, J. Li, Z. Sun, Z. Lv, X. S. Wu, Q. Jiang, H.-L. Cai and D. Shi, *Bioactive Materials*, 2022, **8**, 435-448.
- 143. B. Shen, X. Liao, X. Zhang, H.-T. Ren, J.-H. Lin, C.-W. Lou and T.-T. Li, *Electrochimica Acta*, 2022, **413**, 140144.
- 144. A. Byeon, A. M. Glushenkov, B. Anasori, P. Urbankowski, J. Li, B. W. Byles, B. Blake, K. L. Van Aken, S. Kota, E. Pomerantseva, J. W. Lee, Y. Chen and Y. Gogotsi, *Journal of Power Sources*, 2016, **326**, 686-694.
- 145. X. Ren, M. Huo, M. Wang, H. Lin, X. Zhang, J. Yin, Y. Chen and H. Chen, *ACS nano*, 2019, **13**, 6438-6454.
- 146. W. L. Zhang, J. Tian, H. Zeng, J. Liu and Y. Tian, *Chemical Engineering Journal*, 2019, **366**, 321-329.
- 147. Z. Lan, H. Fu, R. Zhao, H. Liu, W. Zhou, H. Ning and J. Guo, *Chemical Engineering Journal*, 2022, 431, 133985.
- 148. S.-Y. Pang, W.-F. Io, L.-W. Wong, J. Zhao and J. Hao, *Advanced Science*, 2020, **7**, 1903680.
- 149. S. Tu, F. Ming, J. Zhang, X. Zhang and H. N. Alshareef, *Advanced Materials*, 2019, **31**, 1806860.
- 150. P. A. Rasheed, R. P. Pandey, F. Banat and S. W. Hasan, *Matter*, 2022, **5**, 546-572.
- 151. X. Li, X. Ma, Y. Hou, Z. Zhang, Y. Lu, Z. Huang, G. Liang, M. Li, Q. Yang and J. Ma, *Joule*, 2021, **5**, 2993-3005.
- 152. G. Liang, X. Li, Y. Wang, S. Yang, Z. Huang, Q. Yang, D. Wang, B. Dong, M. Zhu and C. Zhi, *Nano Research Energy*, 2022, **1**, e9120002.
- 153. S. Sardar and A. Jana, *Matter*, 2020, **3**, 1397-1399.
- 154. C. Huang, S. Shi and H. Yu, ACS Energy Letters, 2021, **6**, 3464-3472.
- 155. M. Naguib, Y. Gogotsi and M. W. Barsoum, 2015.
- 156. M. Je, Y. Lee and Y.-C. Chung, *Thin Solid Films*, 2016, **619**, 131-136.
- 157. C. Si, J. Zhou and Z. Sun, ACS applied materials interfaces, 2015, 7, 17510-17515.

- 158. A. Yadav, A. Dashora, N. Patel, A. Miotello, M. Press and D. Kothari, *Applied Surface Science*, 2016, **389**, 88-95.
- 159. Q. T. H. Ta, N. M. Tran and J.-S. Noh, Materials Manufacturing Processes, 2021, 36, 200-208.
- 160. J. M. Schneider, Z. Sun, R. Mertens, F. Uestel and R. Ahuja, *Solid State Communications*, 2004, **130**, 445-449.
- 161. A. M. Abdelkader, *Journal of the European Ceramic Society*, 2016, **36**, 33-42.
- 162. B. S. Reghunath, D. Davis and K. S. J. C. Devi, *Chemosphere*, 2021, **283**, 131281.
- 163. J. P. Siebert, L. Bischoff, M. Lepple, A. Zintler, L. Molina-Luna, U. Wiedwald and C. S. J. J. o. M. C. C. Birkel, *Journal of Materials Chemistry C*, 2019, **7**, 6034-6040.
- 164. M. H. Tran, A. M. Malik, M. Dürrschnabel, A. Regoutz, P. Thakur, T.-L. Lee, D. Perera, L. Molina-Luna, K. Albe and J. Rohrer, *Dalton Transactions*, 2020, **49**, 12215-12221.
- 165. N. C. Frey, J. Wang, G. I. n. Vega Bellido, B. Anasori, Y. Gogotsi and V. B. Shenoy, *ACS Nano*, 2019, **13**, 3031-3041.
- 166. B. Soundiraraju, R. Raghavan and B. K. George, *ACS Applied Nano Materials*, 2020, **3**, 11007-11016.
- 167. S.-Y. Pang, Y.-T. Wong, S. Yuan, Y. Liu, M.-K. Tsang, Z. Yang, H. Huang, W.-T. Wong and J. Hao, *Journal of the American Chemical Society*, 2019, **141**, 9610-9616.
- 168. Y.-W. Cheng, J.-H. Dai, Y.-M. Zhang and Y. Song, *Journal of Materials Chemistry A*, 2018, **6**, 20956-20965.
- 169. M. F. Cover, O. Warschkow, M. M. M. Bilek and D. R. McKenzie, *Journal of Physics: Condensed Matter*, 2009, **21**, 305403.
- 170. B. Ahmed, A. E. Ghazaly and J. Rosen, Advanced Functional Materials, 2020, 30, 2000894.
- 171. R. Meshkian, M. Dahlqvist, J. Lu, B. Wickman, J. Halim, J. Thörnberg, Q. Tao, S. Li, S. Intikhab and J. Snyder, *Advanced materials*, 2018, **30**, 1706409.
- 172. J. Yang, R. Liu, N. Jia, K. Wu, X. Fu, Q. Wang and W. Cui, *Carbon*, 2021, **183**, 76-83.
- 173. R. K. Choudhury, B. R. Bhagat, K. H. Mali, R. Pokar and A. Dashora, *Applied Surface Science*, 2022, **603**, 154426.
- 174. Y.-C. Zhou, L.-F. He, Z.-J. Lin and J.-Y. Wang, *Journal of the European Ceramic Society*, 2013, **33**, 2831-2865.
- 175. J. Zhou, X. Zha, F. Y. Chen, Q. Ye, P. Eklund, S. Du and Q. Huang, *Angewandte Chemie International Edition*, 2016, **55**, 5008-5013.
- 176. Q. Meng, J. Ma, Y. Zhang, Z. Li, A. Hu, J.-J. Kai and J. Fan, *Journal of Materials Chemistry A*, 2018, **6**, 13652-13660.
- 177. J. Zhu, A. Chroneos, J. Eppinger and U. Schwingenschlögl, *Applied Materials Today*, 2016, **5**, 19-24.
- 178. C.-F. Fu, X. Li, Q. Luo and J. Yang, *Journal of Materials Chemistry A*, 2017, **5**, 24972-24980.
- 179. B. Cai, J. Zhou, D. Li and Z. Ao, *Applied Surface Science*, 2022, **575**, 151777.
- 180. T. Lapauw, B. Tunca, T. Cabioc'h, J. Lu, P. O. Å. Persson, K. Lambrinou and J. Vleugels, *Inorganic Chemistry*, 2016, **55**, 10922-10927.
- 181. J. Zhou, X. Zha, X. Zhou, F. Chen, G. Gao, S. Wang, C. Shen, T. Chen, C. Zhi, P. Eklund, S. Du, J. Xue, W. Shi, Z. Chai and Q. Huang, *ACS nano*, 2017, **11**, 3841-3850.
- 182. R. Syamsai and A. N. Grace, Journal of Alloys and Compounds, 2019, 792, 1230-1238.
- 183. J. Zhou, X.-H. Zha, M. Yildizhan, P. Eklund, J. Xue, M. Liao, P. O. Persson, S. Du and Q. Huang, *ACS nano*, 2019, **13**, 1195-1203.
- 184. G. Zhao, J. Chen, Y. Li, L. Zheng, J. Li, X. Wang and M. Li, *Journal of the European Ceramic Society*, 2017, **37**, 83-89.
- 185. L. F. He, Y. W. Bao, J. Y. Wang, M. S. Li and Y. C. Zhou, *Acta Materialia*, 2009, **57**, 2765-2774.
- 186. L. F. He, H. Q. Nian, X. P. Lu, Y. W. Bao and Y. C. Zhou, *Scripta Materialia*, 2010, **62**, 427-430.
- 187. D. D. Jayaseelan, S. Pramana, S. Grasso, Y. Bai, S. Skinner, M. J. Reece and W. E. Lee, *Journal of the European Ceramic Society*, 2022, **42**, 1292-1301.

- 188. C. Ougherb, T. Ouahrani, M. Badawi and Á. Morales-García, *Physical Chemistry Chemical Physics*, 2022, **24**, 7243-7252.
- 189. A. Gencer, S. Aydin, O. Surucu, X. Wang, E. Deligoz and G. Surucu, *Applied Surface Science*, 2021, **551**, 149484.
- 190. Y. Liu, X. Ji, J. Liu, W. W. L. Tong, D. Askhatova and J. Shi, *Advanced Functional Materials*, 2017, **27**, 1703261.
- 191. A. Rafieerad, W. Yan, K. N. Alagarsamy, A. Srivastava, N. Sareen, R. C. Arora and S. Dhingra, *Advanced Functional Materials*, 2021, **31**, 2106786.
- 192. J. W. Lambert, Y. Sun, C. Stillson, Z. Li, R. Kumar, S. Wang, P. F. FitzGerald, P. J. Bonitatibus, R. E. Colborn, J. C. Roberts, P. M. Edic, M. Marino and B. M. Yeh, *Radiology*, 2018, **289**, 103-110.
- 193. T. Fan, L. Yan, S. He, Q. Hong, F. Ai, S. He, T. Ji, X. Hu, E. Ha, B. Zhang, Z. Li, H. Zhang, X. Chen and J. Hu, *Chemical Society Reviews*, 2022, **51**, 7732-7751.
- 194. H. Lin, Y. Wang, S. Gao, Y. Chen and J. Shi, Advanced materials, 2018, 30, 1703284.
- 195. Z. Liu, H. Lin, M. Zhao, C. Dai, S. Zhang, W. Peng and Y. Chen, *Theranostics*, 2018, **8**, 1648-1664.
- 196. A. Rafieerad, A. Amiri, G. L. Sequiera, W. Yan, Y. Chen, A. A. Polycarpou and S. Dhingra, *Advanced Functional Materials*, 2021, **31**, 2100015.
- 197. L. Dong, H. Chu, Y. Li, X. Ma, H. Pan, S. Zhao and D. Li, *Applied materials today*, 2022, **26**, 101341.
- 198. T. Wu, X. Pang, S. Zhao, S. Xu, Z. Liu, Y. Li and F. Huang, Small Structure, 2022, 3, 2100206.
- 199. J. Mei, G. A. Ayoko, C. Hu, J. M. Bell and Z. Sun, *Sustainable Materials Technologies*, 2020, **25**, e00156.
- 200. D. B. Velusamy, J. K. El-Demellawi, A. M. El-Zohry, A. Giugni, S. Lopatin, M. N. Hedhili, A. E. Mansour, E. D. Fabrizio, O. F. Mohammed and H. N. Alshareef, *Advanced Materials*, 2019, **31**, 1807658.
- 201. P. Urbankowski, B. Anasori, K. Hantanasirisakul, L. Yang, L. Zhang, B. Haines, S. J. May, S. J. Billinge and Y. Gogotsi, *Nanoscale*, 2017, **9**, 17722-17730.
- 202. E. B. Deeva, A. Kurlov, P. M. Abdala, D. Lebedev, S. M. Kim, C. P. Gordon, A. Tsoukalou, A. Fedorov and C. R. Müller, *Chemistry of Materials*, 2019, **31**, 4505-4513.
- 203. Y. Liu, Y. Jiang, Z. Hu, J. Peng, W. Lai, D. Wu, S. Zuo, J. Zhang, B. Chen and Z. Dai, *Advanced Functional Materials*, 2021, **31**, 2008033.
- 204. Y. Dall'Agnese, P.-L. Taberna, Y. Gogotsi and P. Simon, *The journal of physical chemistry letters*, 2015, **6**, 2305-2309.
- 205. X. Sun, X. He, Y. Zhu, E. Obeng, B. Zeng, H. Deng, J. Shen and R. Hu, *Chemical Engineering Journal*, 2023, **451**, 138985.
- 206. E. Lee, A. VahidMohammadi, Y. S. Yoon, M. Beidaghi and D.-J. Kim, *ACS sensors*, 2019, **4**, 1603-1611.
- 207. W. Zhang, J. Peng, W. Hua, Y. Liu, J. Wang, Y. Liang, W. Lai, Y. Jiang, Y. Huang and W. Zhang, *Advanced Energy Materials*, 2021, **11**, 2100757.
- 208. J. Zhang, C. Huang, Y. Sun and H. Yu, Advanced Functional Materials, 2022, 32, 2113367.
- 209. L. Gao, H. Chen, F. Zhang, S. Mei, Y. Zhang, W. Bao, C. Ma, P. Yin, J. Guo and X. Jiang, *Small Methods*, 2020, **4**, 2000250.
- 210. K. J. Griffith, M. A. Hope, P. J. Reeves, M. Anayee, Y. Gogotsi and C. P. Grey, *Journal of the American Chemical Society*, 2020, **142**, 18924-18935.
- 211. A. Lipatov, M. J. Loes, N. S. Vorobeva, S. Bagheri, J. Abourahma, H. Chen, X. Hong, Y. Gogotsi and A. Sinitskii, *ACS Materials Letters*, 2021, **3**, 1088-1094.
- 212. O. Akinola, I. Chakraborty, H. Celio, D. Akinwande and J. A. C. Incorvia, *Journal of Materials Research*, 2021, **36**, 1980-1989.
- 213. R. Meshkian, H. Lind, J. Halim, A. El Ghazaly, J. Thornberg, Q. Tao, M. Dahlqvist, J. Palisaitis, P. O. Persson and J. Rosen, *ACS Applied Nano Materials*, 2019, **2**, 6209-6219.
- 214. B. Zhou, H. Yin, C. Dong, L. Sun, W. Feng, Y. Pu, X. Han, X. Li, D. Du and H. Xu, *Advanced Science*, 2021, **8**, 2101043.

- 215. S. Liu, R. Lv, J. Wang, Y. Wang, H. Wang, H. Zhang and Y. Wang, *Journal of Materials Chemistry C*, 2021, **9**, 16985-16990.
- 216. J. Zhou, X. Zha, F. Y. Chen, Q. Ye, P. Eklund, S. Du and Q. Huang, *Angewandte Chemie International Edition*, 2016, **55**, 5008-5013.
- 217. Y.-C. Zhou, L.-F. He, Z.-J. Lin and J.-Y. Wang, *Journal of the European Ceramic Society*, 2013, **33**, 2831-2865.
- 218. Q. Chen, D. Zhang, J. Pan and W. Fan, *Optik*, 2020, **219**, 165046.
- 219. D. L. Druffel, M. G. Lanetti, J. D. Sundberg, J. T. Pawlik, M. S. Stark, C. L. Donley, L. M. McRae, K. M. Scott and S. C. Warren, *Chemistry of Materials*, 2019, **31**, 9788-9796.
- 220. K. Maeda, H. Wakayama, Y. Washio, A. Ishikawa, M. Okazaki, H. Nakata and S. Matsuishi, *The Journal of Physical Chemistry C*, 2020, **124**, 14640-14645.
- 221. S. Sun, J. Yang, X. Chen, W. Cui, J. Huang, T. Yang, Z. Zhang and Q. Wang, *Scripta Materialia*, 2020, **181**, 10-14.
- 222. S. Riva, K. V. Yusenko, N. P. Lavery, D. J. Jarvis and S. G. R. Brown, *International Materials Reviews*, 2016, **61**, 203-228.
- 223. X.-H. Zha, J.-C. Ren, L. Feng, X. Bai, K. Luo, Y. Zhang, J. He, Q. Huang, J. S. Francisco and S. Du, *Nanoscale*, 2018, **10**, 8763-8771.
- 224. K. Xiong, P. Wang, G. Yang, Z. Liu, H. Zhang, S. Jin and X. Xu, Scientific Reports, 2017, 7, 15095.
- 225. L. Zhou, Y. Zhang, Z. Zhuo, A. J. Neukirch and S. Tretiak, *The Journal of Physical Chemistry Letters*, 2018, **9**, 6915-6920.
- 226. J.-H. Liu, X. Kan, B. Amin, L.-Y. Gan and Y. Zhao, *Physical Chemistry Chemical Physics*, 2017, **19**, 32253-32261.
- 227. X.-H. Zha, J. Zhou, Y. Zhou, Q. Huang, J. He, J. S. Francisco, K. Luo and S. Du, *Nanoscale*, 2016, **8**, 6110-6117.
- 228. S. Bae, W. Espinosa-García, Y.-G. Kang, N. Egawa, J. Lee, K. Kuwahata, M. Khazaei, K. Ohno, Y.-H. Kim, M. J. Han, H. Hosono, G. M. Dalpian and H. Raebiger, *Advanced Functional Materials*, 2021, **31**, 2100009.
- 229. K. Fukuda and M. Hisamura, *Journal of the American Ceramic Society*, 2007, **90**, 3299-3302.
- 230. A. Mostafaei and M. Abbasnejad, Journal of Alloys and Compounds, 2021, 857, 157982.
- 231. A. Aliakbari, P. Amiri and H. Salehi, FlatChem, 2022, **31**, 100328.
- 232. E. Omugbe, O. E. Osafile, O. N. Nenuwe and E. A. Enaibe, *Physica B: Condensed Matter*, 2022, **639**, 413922.
- 233. J. Hou, K. Tu and Z. Chen, The Journal of Physical Chemistry C, 2016, 120, 18473-18478.
- 234. L. Gao, W. Bao, A. V. Kuklin, S. Mei, H. Zhang and H. Ågren, *Advanced Materials*, 2021, **33**, 2004129
- 235. R. Wang, M. Li, K. Sun, Y. Zhang, J. Li and W. Bao, Small, 2022, 18, 2201740.
- 236. H. Kim, B. Anasori, Y. Gogotsi and H. N. Alshareef, *Chemistry of Materials*, 2017, **29**, 6472-6479.
- 237. C. Zhan, W. Sun, Y. Xie, D.-e. Jiang and P. R. Kent, *ACS Applied Materials*, 2019, **11**, 24885-24905.
- 238. M. Khazaei, M. Arai, T. Sasaki, C. Y. Chung, N. S. Venkataramanan, M. Estili, Y. Sakka and Y. Kawazoe, *Advanced Functional Materials*, 2013, **23**, 2185-2192.
- 239. C. Si, K.-H. Jin, J. Zhou, Z. Sun and F. Liu, *Nano letters*, 2016, **16**, 6584-6591.
- 240. J. Yang, X. Zhou, X. Luo, S. Zhang and L. Chen, Applied Physics Letters, 2016, 109.
- 241. D. Jin, L. R. Johnson, A. S. Raman, X. Ming, Y. Gao, F. Du, Y. Wei, G. Chen, A. Vojvodic and Y. Gogotsi, *The Journal of Physical Chemistry C*, 2020, **124**, 10584-10592.
- 242. V. Mehta, K. Tankeshwar and H. S. Saini, 2018.
- 243. C. Ling, L. Shi, Y. Ouyang, Q. Chen and J. Wang, *Advanced Science*, 2016, **3**, 1600180.
- 244. Y. Cheng, J. Dai, Y. Song and Y. Zhang, ACS Applied Energy Materials, 2019, 2, 6851-6859.
- 245. D. Yang, X. Fan, D. Zhao, Y. An, Y. Hu and Z. Luo, *Physica E: Low-dimensional Systems Nanostructures*, 2019, **111**, 84-90.

- 246. C. Cheng, X. Zhang, M. Wang, S. Wang and Z. Yang, *Physical Chemistry Chemical Physics*, 2018, **20**, 3504-3513.
- 247. D. Kan, D. Wang, X. Zhang, R. Lian, J. Xu, G. Chen and Y. Wei, *Journal of Materials Chemistry A*, 2020, **8**, 3097-3108.
- 248. T. L. Tan, H. M. Jin, M. B. Sullivan, B. Anasori and Y. Gogotsi, *ACS nano*, 2017, **11**, 4407-4418.
- 249. E. Balcı, Ü. Ö. Akkuş and S. Berber, *Journal of Physics: Condensed Matter*, 2018, **30**, 155501.
- 250. E. Balcı, Ü. Ö. Akkuş and S. Berber, Journal of Materials Chemistry C, 2017, 5, 5956-5961.
- 251. B. Huang, N. Zhou, X. Chen, W. J. Ong and N. Li, *Chemistry—A European Journal*, 2018, **24**, 18479-18486.
- 252. B. Ding, W.-J. Ong, J. Jiang, X. Chen and N. Li, *Applied Surface Science*, 2020, **500**, 143987.
- 253. C. Ling, L. Shi, Y. Ouyang and J. Wang, *Chemistry of Materials*, 2016, **28**, 9026-9032.
- 254. Z. Chen, S. Huang, B. Huang, M. Wan and N. Zhou, Applied Surface Science, 2020, 509, 145319.
- 255. J. Yang, X. Luo, S. Zhang and L. Chen, *Physical Chemistry Chemical Physics*, 2016, **18**, 12914-12919.
- 256. M. Khazaei, A. Ranjbar, M. Arai and S. Yunoki, *Physical Review B*, 2016, **94**, 125152.
- 257. C. Cheng, X. Zhang, Z. Yang and Z. Zhou, *ACS Applied Materials Interfaces*, 2018, **10**, 32903-32912.
- 258. V. Shukla, N. K. Jena, S. R. Naqvi, W. Luo and R. Ahuja, *Nano Energy*, 2019, **58**, 877-885.
- 259. J. Yang, A. Wang, S. Zhang, H. Wu and L. Chen, *Computational Materials Science*, 2018, **153**, 303-308.
- 260. S. Zheng, S. Li, Z. Mei, Z. Hu, M. Chu, J. Liu, X. Chen and F. Pan, *The Journal of Physical Chemistry Letters*, 2019, **10**, 6984-6989.
- 261. Y. Xin and Y.-X. Yu, *Materials Design*, 2017, **130**, 512-520.
- 262. J. He, P. Lyu, L. Z. Sun, Á. Morales García and P. Nachtigall, *Journal of Materials Chemistry C*, 2016, **4**, 6500-6509.
- 263. H. Li, X. Wang, H. Li, S. Lin, B. Zhao, J. Dai, W. Song, X. Zhu and Y. Sun, *Journal of Alloys Compounds*, 2019, **784**, 923-930.
- 264. R. Liu, W. Cao, D. Han, Y. Mo, H. Zeng, H. Yang and W. Li, *Journal of Alloys Compounds*, 2019, **793**, 505-511.
- 265. C. Xu, F. Wu, C. Hu, L. Yang and S. Yin, Journal of Alloys Compounds, 2024, 175837.
- 266. H. Ang, H. T. Tan, Z. M. Luo, Y. Zhang, Y. Y. Guo, G. Guo, H. Zhang and Q. Yan, *Small*, 2015, **11**, 6278-6284.
- 267. J. Jia, T. Xiong, L. Zhao, F. Wang, H. Liu, R. Hu, J. Zhou, W. Zhou and S. Chen, *ACS nano*, 2017, **11**, 12509-12518.
- 268. J.-Q. Chi, W.-K. Gao, J.-H. Lin, B. Dong, J.-F. Qin, Z.-Z. Liu, B. Liu, Y.-M. Chai and C.-G. Liu, *Journal of Catalysis*, 2018, **360**, 9-19.
- 269. C. Chen, X. Xie, B. Anasori, A. Sarycheva, T. Makaryan, M. Zhao, P. Urbankowski, L. Miao, J. Jiang and Y. Gogotsi, *Angewandte Chemie International Edition*, 2018, **57**, 1846-1850.
- 270. F. Wu, C. Xu, X. Yang, L. Yang and S. Yin, *International Journal of Hydrogen Energy*, 2022, **47**, 17233-17240.
- 271. B. Unnikrishnan, C.-W. Wu, A. Sangili, Y.-J. Hsu, Y.-T. Tseng, J. S. Pandey, H.-T. Chang and C.-C. Huang, *Journal of Colloid Interface Science*, 2022, **628**, 849-857.
- 272. Z. Shi, K. Nie, Z.-J. Shao, B. Gao, H. Lin, H. Zhang, B. Liu, Y. Wang, Y. Zhang and X. Sun, *Energy Environmental Science*, 2017, **10**, 1262-1271.
- 273. G. Qu, Y. Zhou, T. Wu, G. Zhao, F. Li, Y. Kang and C. Xu, *ACS Applied Energy Materials*, 2018, **1**, 7206-7212.
- 274. X. Guo, L. Li, S. Wang, J. Shen, Y. Xu and B. Cao, *Materials Advances*, 2023, **4**, 1523-1533.
- 275. J.-Q. Chi, W.-K. Gao, J.-H. Lin, B. Dong, K.-L. Yan, J.-F. Qin, Z.-Z. Liu, Y.-M. Chai and C.-G. Liu, *Journal of colloid interface science*, 2018, **513**, 151-160.
- 276. Y.-Y. Chen, Y. Zhang, W.-J. Jiang, X. Zhang, Z. Dai, L.-J. Wan and J.-S. Hu, *ACS Nano*, 2016, **10**, 8851-8860.

- 277. D. Wang, T. Liu, J. Wang and Z. Wu, *Carbon*, 2018, **139**, 845-852.
- 278. A. Dey, S. Varagnolo, N. P. Power, N. Vangapally, Y. Elias, L. Damptey, B. N. Jaato, S. Gopalan, Z. Golrokhi and P. Sonar, *Progress in materials science*, 2023, 101166.
- 279. S. Zhang, J. Zheng, J. Lin, Y. Li, Z. Bao, X. Peng, W. Ji, L. Ding, Z. Xu and G. Wang, *Nano Research*, 2023, **16**, 6120-6127.
- 280. M. Hu, B. Liu, H. Chen, X. Xu, P. Jing, X. Guo, R. Yang, X. Wang, R. Gao and J. Zhang, *Applied Catalysis B: Environmental*, 2023, **322**, 122131.
- 281. Y. Zhang, J. Li, Z. Gong, J. Xie, T. Lu and L. Pan, *Journal of Colloid Interface Science*, 2021, **587**, 489-498.
- 282. M. Lian, Y. Shi, W. Zhang, J. Zhao and D. Chen, *Journal of Electroanalytical Chemistry*, 2022, **904**, 115849.
- 283. H. Lu, J. Li, X. Zhou, Y. Lu, Q. Li and F. Pan, *Journal of Materials Science Technology*, 2024, **190**, 135-144.
- 284. J. Zhou, S. Gao, Z. Guo and Z. Sun, Ceramics International, 2017, 43, 11450-11454.
- 285. Y. Wang, W. Zheng, P. Zhang, W. Tian, J. Chen and Z. Sun, *Journal of Materials Science*, 2019, **54**, 11991-11999.
- 286. W. Peng, M. Luo, X. Xu, K. Jiang, M. Peng, D. Chen, T. S. Chan and Y. Tan, *Advanced Energy Materials*, 2020, **10**, 2001364.
- 287. K. D. Sabnis, Y. Cui, M. C. Akatay, M. Shekhar, W.-S. Lee, J. T. Miller, W. N. Delgass and F. H. Ribeiro, *Journal of Catalysis*, 2015, **331**, 162-171.
- 288. Z. Li, Y. Cui, Z. Wu, C. Milligan, L. Zhou, G. Mitchell, B. Xu, E. Shi, J. T. Miller and F. H. Ribeiro, *Nature Catalysis*, 2018, **1**, 349-355.
- 289. Q. Tao, J. Lu, M. Dahlqvist, A. Mockute, S. Calder, A. Petruhins, R. Meshkian, O. Rivin, D. Potashnikov and E. a. N. Caspi, *Chemistry of Materials*, 2019, **31**, 2476-2485.
- 290. Z. Shen, Z. Wang, M. Zhang, M. Gao, J. Hu, F. Du, Y. Liu and H. Pan, *Materialia*, 2018, **1**, 114-120.
- 291. J. Zhang, Y. Zhao, X. Guo, C. Chen, C.-L. Dong, R.-S. Liu, C.-P. Han, Y. Li, Y. Gogotsi and G. Wang, *Nature Catalysis*, 2018, **1**, 985-992.
- 292. Z. Jin, Y. Fang, X. Wang, G. Xu, S. Wei, C. Zhou, Y. Zhang and Y. Xu, *Journal of colloid interface science*, 2019, **537**, 306-315.
- 293. D. Sabaghi, J. Polčák, H. Yang, X. Li, A. Morag, D. Li, A. S. Nia, S. Khosravi H, T. Šikola and X. Feng, *Advanced Energy Materials*, 2024, **14**, 2302961.
- 294. L. Qin, Q. Tao, A. El Ghazaly, J. Fernandez-Rodriguez, P. O. Persson, J. Rosen and F. Zhang, *Advanced Functional Materials*, 2018, **28**, 1703808.
- 295. Y. Cheng, Y. Li, L. Yang and S. Yin, ACS Applied Nano Materials, 2023, 6, 9186-9196.
- 296. Y. Wang, J. Shen, L.-C. Xu, Z. Yang, R. Li, R. Liu and X. Li, *Physical Chemistry Chemical Physics*, 2019, **21**, 18559-18568.
- 297. V. Mehta, H. S. Saini, S. Srivastava, M. K. Kashyap and K. Tankeshwar, *The Journal of Physical Chemistry C*, 2019, **123**, 25052-25060.
- 298. C. Sevik, J. Bekaert and M. V. Milošević, *Nanoscale*, 2023, **15**, 8792-8799.
- 299. J. Chen, K. Chen, D. Tong, Y. Huang, J. Zhang, J. Xue, Q. Huang and T. Chen, *Chemical Communications*, 2015, **51**, 314-317.
- 300. Y. Zhou, L. Yin, S. Xiang, S. Yu, H. M. Johnson, S. Wang, J. Yin, J. Zhao, Y. Luo and P. K. Chu, *Advanced Science*, 2024, **11**, 2304874.
- 301. I. Hussain, O. J. Kewate, S. Sahoo, S. Aftab, P. Rosaiah, M. Ahmad, M. B. Hanif, W. Al Zoubi, Z. Ajmal and W. U. Arifeen, *Chemical Engineering Journal*, 2024, 154978.
- 302. E. Cevik, S. T. Gunday, A. Iqbal, S. Akhtar and A. Bozkurt, *Journal of Energy Storage*, 2022, **46**, 103824.
- 303. L. Qin, J. Jiang, L. Hou, F. Zhang and J. Rosen, *Journal of Materials Chemistry A*, 2022, **10**, 12544-12550.
- 304. X. Bin, M. Sheng, Y. Luo and W. J. A. M. I. Que, 2022, **9**, 2200231.

- 305. B. Shen, X. Liao, X. Hu, H.-T. Ren, J.-H. Lin, C.-W. Lou and T.-T. Li, *Journal of Materials Chemistry A*, 2023, **11**, 16823-16837.
- 306. Y. Zhu, X. Ji, L. Yang, J. Jia, S. Cheng, H. Chen, Z.-S. Wu, D. Passarello and M. Liu, *Journal of materials chemistry A*, 2020, **8**, 7819-7827.
- 307. D. Wu, S. Zhao, T. Huang, W. He, X. Zhou, G. Wang, M. Guo, X. Luo, M. Cao and Y. Yue, *Chemical Engineering Journal*, 2024, **490**, 151589.
- 308. S. Hussain, I. Rabani, D. Vikraman, A. Feroze, K. Karuppasamy, Z. u. Haq, Y.-S. Seo, S.-H. Chun, H.-S. Kim and J. Jung, *ACS Sustainable Chemistry Engineering*, 2020, **8**, 12248-12259.
- 309. X. Pang, Z. Lv, S. Xu, J. Rong, M. Cai, C. Zhao and F. Huang, *Energy Storage Materials*, 2023, **61**, 102860.
- 310. T. Li, S. Gao, K. Li, G. Liu, X. Sheng, D. Shang, L. Wu, S. Chen, Y. Wang and S. Wu, *Journal of Alloys Compounds*, 2023, **934**, 168042.
- 311. Z. Wang, Z. Huang, H. Wang, W. Li, B. Wang, J. Xu, T. Xu, J. Zang, D. Kong and X. Li, *ACS nano*, 2022, **16**, 9105-9116.
- 312. S. Yang, S. Wang, D. Chen, W. He and L. Li, Chemical Engineering Journal, 2021, 413, 127471.
- 313. M. Xu, T. Wu, J. Qi, D. Zhou and Z. Xiao, *Journal of Materials Chemistry A*, 2021, **9**, 21429-21439.
- 314. Y. Mao, W. Sun, X. Yue, W. Hou, T. Deng, L. He, L. Fang, R. Sun, Z. Wang and K. Sun, *Journal of Power Sources*, 2021, **506**, 230254.
- 315. L. Malyala, S. Karingula, T. Bhookya and G. K Vengatajalabathy, *Energy Storage*, 2024, **6**, e70012.
- 316. H. Li, P. Tang, H. Shen, T. Hu, J. Chen, K. Chen, F. Qi, H. Yang, L. Wen and F. Li, *Carbon*, 2021, **183**, 840-849.
- 317. S. Zhao, C. Chen, X. Zhao, X. Chu, F. Du, G. Chen, Y. Gogotsi, Y. Gao and Y. Dall'Agnese, *Advanced Functional Materials*, 2020, **30**, 2000815.
- 318. A. S. Etman, J. Halim and J. Rosen, *Materials Advances*, 2021, **2**, 743-753.
- 319. D. Gandla, F. Zhang and D. Q. Tan, *ACS omega*, 2022, **7**, 7190-7198.
- 320. X. Pang, H. Lee, J. Rong, Q. Zhu and S. Xu, *Small*, 2024, 2309580.
- 321. R. Venkatkarthick, N. Rodthongkum, X. Zhang, S. Wang, P. Pattananuwat, Y. Zhao, R. Liu and J. Qin, *ACS Applied Energy Materials*, 2020, **3**, 4677-4689.
- 322. K. Subramanyan, S. Chen, N. Li, T. Ma, Y. Liu, S. Chandrasekaran and V. Aravindan, *Electrochimica Acta*, 2023, **437**, 141505.
- 323. X. Wang, L. Gong, Z. Li, Y. Yin and D. Zhang, *Journal of Materials Chemistry A*, 2023, **11**, 7690-7701.
- 324. M. S. Deepak, N. K. Das and S. Badhulika, Journal of Alloys Compounds, 2024, 176426.
- 325. A. Ahmed, S. Sharma, B. Adak, M. M. Hossain, A. M. LaChance, S. Mukhopadhyay and L. Sun, *InfoMat*, 2022, **4**, e12295.
- 326. X. Wang, D. Zhang, H. Zhang, L. Gong, Y. Yang, W. Zhao, S. Yu, Y. Yin and D. Sun, *Nano Energy*, 2021, **88**, 106242.
- 327. O. Faruk, M. R. Islam, S. S. Rana, G. B. Pradhan, H. Kim, M. Asaduzzaman, T. Bhatta and J. Y. Park, *Nano Energy*, 2024, 109787.
- 328. J. Fan, C. Wang, B. Wang, B. Wang and F. Liu, *Nanomaterials*, 2024, **14**, 428.
- 329. X. Yang, F. Wu, C. Xu, L. Yang and S. Yin, Journal of Alloys Compounds, 2022, 928, 167137.
- 330. B. Richard, K. Niyas, M. Ankitha and P. A. Rasheed, *ACS Applied Nano Materials*, 2024, **7**, 9585-9597
- 331. D. Mohapatra, H. J. Kang, S. Lee, Y. Son, M. Z. Ansari, Y. Kang, J. W. Lee and S. H. Kim, *Small*, 2024, 2402003.
- 332. D. Mohapatra, Y. Shin, M. Z. Ansari, Y. H. Kim, Y. J. Park, T. Cheon, H. Kim, J. W. Lee and S. H. Kim, *Advanced Science*, 2023, **10**, 2206355.

No primary research results, software or code have been included and no new data were generated or analysed as part of this review.